LED-Based Light Scattering Measurements of Papers for Printing Applications

Vom Fachbereich Maschinenbau
an der Technischen Universität Darmstadt
zur
Erlangung des akademischen Grades eines Doktor-Ingenieurs (Dr.-Ing.)
genehmigte

D i s s e r t a t i o n

vorgelegt von
Dipl.-Ing. Kathrin Happel
aus Frankfurt a.M.

Berichterstatter: Prof. Dr.-Ing. Edgar Dörsam
Mitberichterstatter: Prof. Dr.-Ing. habil. Tran Quoc Khanh

Datum der Einreichung: 04.07.2011
Datum der mündlichen Prüfung: 22.09.2011

Darmstadt 2011
D17

Kurzfassung

Für die Druckproduktion ist eine Steuerung und daher eine akkurate Vorhersage des Reflexionsspektrums des Druckprodukts erforderlich, insbesondere, wenn hohe Anforderungen an die Qualität gestellt werden. Dieses Reflexionsspektrum hängt von verschiedenen Faktoren ab, darunter auch die Lichtstreueigenschaft des Bedruckstoffs, in den meisten Fällen Papier.

Der Aufwand, ein typisches Druckermodell anzupassen, ist erheblich, denn Testfelder müssen gedruckt und gemessen werden. Mit einer steigenden Zahl von Druckfarben wird dies umso entscheidender, da die Anzahl der möglichen Kombinationen von übereinander gedruckten Farben exponentiell zunimmt. Sogenannte "First Principle Models" reduzieren den Aufwand, indem die verschiedenen physikalischen Effekte separat modelliert werden. Ein typischer Ansatz ist hierbei die Trennung von optischer und mechanischer Tonwertzunahme.

Für die Modellierung der optischen Tonwertzunahme ist die Messung der Lichtstreuung im Bedruckstoff eines der zentralen Elemente.

Diese Arbeit stellt die nötigen Mittel bereit, um einen Messaufbau zu entwerfen, mit dem diese Lichtstreuung in Papier oder in anderen Bedruckstoffen erfasst werden kann. Ein solcher Messaufbau wurde realisiert und analysiert. Des Weiteren werden repräsentative Messergebnisse vorgestellt.

Die wichtigsten Vorteile des ermittelten Messaufbaus sind die verbesserten Fokus-Werkzeuge, die Untersuchung über mögliche Ursachen von Messfehlern, und die winkelaufgelöste Messung um Anisotropie der Lichtstreuung feststellen zu können.

In einer theoretischen Studie auf Basis von amplitudenmodulierten Druckrastern wird gezeigt, dass die optische Tonwertzunahme vorhergesagt werden kann, ohne dass Testfelder gedruckt werden müssen. Wenn die Lichtstreuung durch eine Punktstreufunktion beschrieben wird, ist dafür lediglich die Messung eines einzelnen Parameters nötig, wenn Transmission der Farbe und Rasterfrequenz bekannt sind.

Eine Voraussetzung für diese Vorhersage der optischen Tonwertzunahme ist die akkurate und verlässliche Messung dieses Parameters. Der Messaufbau dieser Arbeit bietet die Möglichkeit hierzu.

Daher ist diese Arbeit ein Beitrag für die Verbesserung von "First Principle Models" durch die Entkopplung von optischer und mechanischer Tonwertzunahme.

Abstract

High-quality printing requires the control and therefore an accurate prediction of the reflectance spectrum of the printed product. This reflectance is a result of various factors, one of them is the light scattering property of the substrate, which is paper in most cases.

Fitting a typical printer model is cost-intensive since it requires to print and measure test patches. This gets even more important for an increasing number of inks because the possible combinations of overprints rise exponentially. So-called first principle models reduce these costs by modeling different effects separately. A typical approach is decoupling optical and physical dot gain.

A key element of modeling optical dot gain is the measurement of sub-surface light scattering in the substrate.

This work presents the necessary means to design a setup for the measurement of light scattering in paper or other substrates. One measurement setup is introduced and analyzed, and representative results are shown.

The main enhancements of the derived measurement setup are the advanced focusing tools, the investigation of the sources of possible measurement errors, and the angular resolved measurement for detecting anisotropy in light scattering.

A theoretical study on conventional screens showed that optical dot gain can be predicted without printing any patches. Describing light scattering using a point spread function, only the measurement of one parameter is necessary, if ink transmittance and screen frequency are known. A prerequisite for this optical dot gain prediction is an accurate and reliable measurement of that parameter. The measurement setup presented in this work offers the possibility of such a measurement.

Thus, this work is a contribution to improve first principle printer models by decoupling optical dot gain and other physical dot gain sources like ink spread.

Danksagung

Die vorliegende Arbeit entstand während meiner Tätigkeit als wissenschaftliche Mitarbeiterin am Institut für Druckmaschinen und Druckverfahren der Technischen Universität Darmstadt. Mein Dank gilt daher insbesondere Herrn Prof. Dr.-Ing. E. Dörsam für das mir entgegengebrachte Vertrauen, den gewährten Freiraum sowie für die fürsorgliche Unterstützung meiner Arbeit.

Herrn Prof. Dr.-Ing. T. Q. Kahn danke ich vielmals für sein Interesse an der Arbeit und für die Übernahme des Koreferates.

Zudem möchte ich mich bei allen Mitarbeitern des Institutes für Druckmaschinen und Druckverfahren bedanken, für viele hilfreiche Diskussionen und eine sehr angenehme Arbeitsatmosphäre, die maßgeblich zum Gelingen dieser Arbeit beigetragen hat. Besonders danke ich Herrn Dr. Philipp Urban für die wertvollen Diskussionen und Impulse. Weiterer Dank geht an Michael Desch, Dieter Spiehl, Kai Pawlowski, Karsten Rettig und Manfred Jakobi, für die konstruktive Unterstützung bei der Realisierung des Messaufbaus, sowie Marius Walter und Xaver Ludewig für die wertvolle Hilfe in der Entwicklungsphase und die Geduld zur Umsetzung der zahlreichen Messreihen. Für die unermüdliche Ausdauer bei der Korrektur meiner Arbeit danke ich Dieter Spiehl und Selin Manukyan.

Ganz herzlich möchte ich mich bei meinen Eltern und meinem Bruder bedanken, die mich stets in jeder Hinsicht unterstützen und mir durch ihr Vertrauen und ihre Zuversicht den nötigen Rückhalt bieten. Großer Dank geht auch an Maria Fedutina, Simone Schmitt und Sandra Botzet, die für Ablenkung zur richtigen Zeit sorgen und deren Geduld und Verständnis mir insbesondere die letzten Monate erleichtert hat.

Darmstadt, November 2011

Contents

Notations

Acronyms

AM	conventional screen, amplitude modulation
BRDF	bidirectional reflectance distribution function
BTDF	bidirectional transmittance distribution function
CAD	computer-aided design
CCD	charge-coupled device
CDF	color-difference formula
CERAN	glass-ceramic
CIE	Commission Internationale de l'Éclairage
CIELAB	CIE L^*, a^*, b^* color space
CIEXYZ	CIE tristimulus values
CMYK	cyan, magenta, yellow, black
DMD	digital micromirror device
dpi	dots per inch
ESF	edge spread function
FM	frequency modulation
FS mirror	first / front surface mirror
LCOS	liquid crystal on silicone
LED	light-emitting diode
lpi	lines per inch
LSC	light scattering class
LSF	line spread function
MATLAB	matrix laboratory; computing environment by MathWorks
MP	megapixel
MTF	modulation transfer function
NA	numerical aperture of an imaging system
ND	not defined
ODG	optical dot gain

OTF	optical transfer function
PSF	point spread function
PTF	phase transfer function
px	pixel
RGB	red, green, blue
RIP	raster image processor
RMSD	root-mean-square deviation
SDK	software development kit

Symbols

A	fractional area coverage of Halftone in %; nominal A_n, geometrical A_g, effective A_e
a^*	green-red component of CIELAB color space, dimensionless
b^*	blue-yellow component of CIELAB color space, dimensionless
C^*	chroma component of CIELCh color space
D	ink density, dimensionless
$d_{0.1}$	0.1-distance in px
$\mathcal{E}$	edge spread function (ESF), dimensionless
E	irradiance I incident on a surface in $\mathrm{W/m^2}$
$\mathfrak{F}$	quality measure for focus, dimensionless
$\mathcal{F}$	Fourier transform operator
$\mathcal{F}^{-1}$	inverse Fourier transform operator
f_c	conversion factor: definition of the reproduction scale of the imaging system (observation unit) in $\mu\mathrm{m\,px^{-1}}$
f_s	screen frequency in l/cm or lpi
fs	auxiliary variable, dimensionless; product of screen frequency f_s, form parameter for light scattering s, and conversion factor f_c
h^*	hue component of CIELCh color space
h	height of a volume element in m
$\boldsymbol{I}$	relative gray value; normalized to irradiance and averaged over pixel rows
I	irradiance in $\mathrm{W/m^2}$: incident on a surface (E), emitted by a surface (M)
L^*	lightness correlate of CIELAB color space, dimensionless
$\mathcal{L}$	line spread function (LSF), dimensionless

l	pathlength of light through a volume element in m
L	radiance in $\mathrm{W}/(\mathrm{sr}\,\mathrm{m}^2)$
$\mathcal{M}$	mask, dimensionless
M	luminous exitance: irradiance I emitted by a surface in W/m^2
$\tilde{n}$	index of refraction, dimensionless
n	Yule-Nielsen factor, dimensionless
$\mathcal{P}$	point spread function (PSF), dimensionless
Q	electric charge in C (coulomb) or e (elementary charge)
R	reflectance, dimensionless
r	radius in m
S	spectrum of radiant exitance of light source or illuminant, arbitrary unit
s	form parameter of light scattering in px
T	transmittance, dimensionless
t_E	exposure time of camera in s, reciprocal of shutter speed
$\boldsymbol{V}$	gray value of camera, dimensionless
w	weighting function for ink density calculation, dimensionless
X, Y, Z	tristiumulus values for CIE 1931 standard observer, dimensionless
$\overline{x}$, $\overline{y}$, $\overline{z}$	color matching functions for CIE 1931 standard observer, dimensionless
$*$	convolution operator
α	coefficient of absorption, dimensionless
β	radiance factor, dimensionless
ΔA	optical dot gain in %
η	quantum efficiency of a sensor, dimensionless
γ	angle of incidence in ° (degree)
Ω	solid angle in sr (steradian)
ϕ	azimuth angle in ° (degree) or rad (radians)
φ	fluorescent coefficient, dimensionless
ρ	coefficient of surface reflection, dimensionless
$\varsigma_{u,v}$	scattering coefficient, part of incident light from direction u that is scattered in direction v, dimensionless
θ	polar angle relative to the surface normal in degrees or radians

Indices

EMG	modified exponential PSF according to Gustavson
EXP	exponential PSF
GAU	Gaussian PSF
PBX	pillbox PSF
QUA	quadratic rational PSF
RAM	ramp PSF

ACMO	absolute central moment focus measure
CONT	image contrast focus measure
CURV	image curvature focus measure
GDER	Gaussian derivative focus measure
GLVA	gray-level variance focus measure
GLVN	normalized gray-level variance focus measure
GRAS	squared gradient focus measure
HISR	histogram range focus measure
LAPV	variance of Laplacian focus measure
SFIL	steerable filters-based focus measure
SFRQ	spatial frequency focus measure
TENG	Tenengrad focus measure
VOLA	Vollat's correlation-based focus measure
WAVR	wavelet ratio focus measure
WAVS	wavelet sum focus measure
WAVV	wavelet variance focus measure

1

Introduction

1.1 Framework of the Research

Printing is maybe one of the most important production techniques. Although, the word *printing* first reminds everyone of printers at home and at the office, these digital printers are only one aspect of the technology, where the quality of the print is usually of secondary interest.

Nevertheless, high-quality prints blend into our environment so that we do not even notice them. Packaging might be the best example followed by printed cloths. But also the reproduction of images captured by digital cameras leads to new challenges for digital printers. Other examples are reproductions of art paintings, billboard advertisings, as well as high-quality journals and magazines.

The majority of the mentioned examples exceed the boundaries of standard CMYK inks. Especially in packaging, prints with 12 and more inks are not unusual. In recent years, also digital printers with seven (CMYK + RGB) and more inks became increasingly important and new printers with up to 12 inks were introduced to the market.

The precise control of the printing process requires a printer model that accurately predicts the spectral reflectance of the print. The reflectance spectrum of a print reproduction is a result of various factors. These include the spectral reflectance properties of inks and papers, the scattering behavior of incident light within the paper as well as the considered printing process and halftone method.

During the printing process, the printer control values are transformed into a digital layout, which can be printed (see figure 1.1). The resulting reflectances are additionally exposed to *optical dot gain* (ODG).

Typically, multi-ink printer models are *regression based models* [2]. These models treat the printing system as a black box and are not necessarily based on physical principles. In general, test patches are printed and the m model parameters $(c_1, \ldots, c_m)$ are fitted to the reflectances measured.

If one of the influencing factors, such as ink, paper or the printing process is changed, new test patches have to be printed and the model parameters have to be fitted again. It is very difficult to

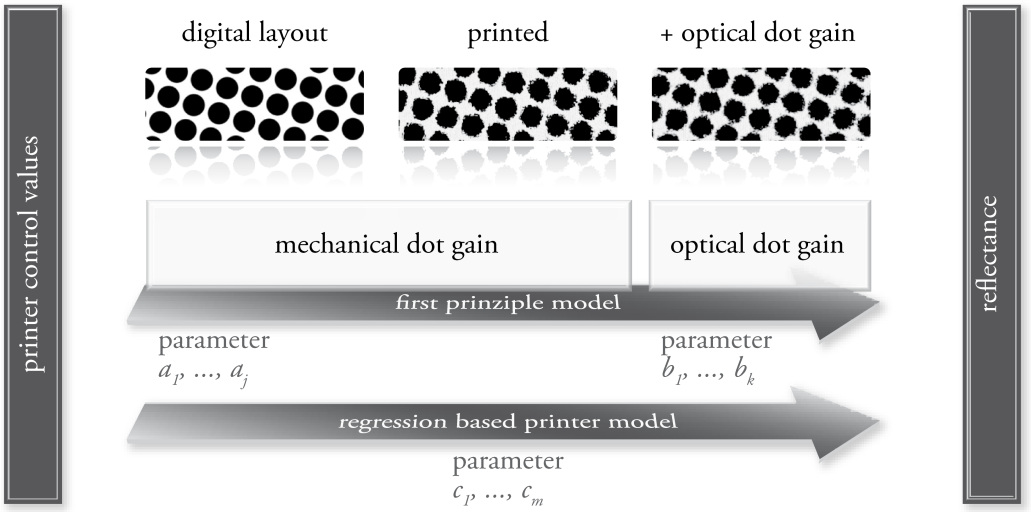

Figure 1.1: Printing process and two different types of printer models ([1] edited).

calculate correction factors to transfer the printer model to a different setup.

Fitting a printer model is cost-intensive since it requires time and material resources. This becomes even more important for an increasing number of inks because the possible combinations of overprints, that have to be represented by a test patch, rise exponentially. Modeling a four-ink system with the widespread *cellular Yule-Nielsen spectral Neugebauer model* utilizing five grid points results in 625 test patches. For a seven-ink system the number of test patches increases to $78,125$ [1].

In contrast, the reflectance prediction of *first principle models* [2] is based on the physical processes of the printing system. Even a printing system with more than four inks is assumed to require only a few test patches for fitting. In this case, the overall number of model parameters of the first principle model (j+k) should be significantly smaller than the number of parameters of the regression based model ($j + k \ll m$ see figure 1.1).

Additionally, some of the results might be transferable to other printing setups. If for example only the paper differs, all parameters that are paper-independent have not to be changed. This way, the effort for fitting a model to a setup can be reduced drastically.

A common approach for first principle models is to model the so-called optical dot gain (ODG) separately. This effect is caused by light scattering in the substrate and makes the halftone appear darker than the fractional area coverage would suggest.

A key element to model ODG is the measurement of sub-surface light scattering in the substrate.

The measurement of reflectances of prints is conducted with spectrophotometers. In recent years, the usage of *light emitting diodes* (LED) as light sources for these instruments became more and more popular. The advantage of an LED compared to a halogen lamp is its better efficiency. Therefore, the

aim of this work is to design a setup to measure light scattering in paper using an LED light source and to analyze the performance of these measurements. Additionally, these measurements open up new possibilities for halftone prediction, which are to be evaluated.

1.2 Objectives

The objective of this research is to build up a reliable measurement setup for detecting light scattering in paper. In order to do so, the various influences on the measurement performance have to be investigated and guidelines for the correct design of the setup have to be analyzed.

Exemplary measurements, taken with the derived setup, will be presented and applied to model optical dot gain in printing.

Deriving a simple representation of the light scattering properties of substrates as a function of only one variable is another objective. The advantage of such a single value is that it could be added to the datasheets by paper producers. Complex data would require a more sophisticated information transfer. Therefore, a single value as scattering characteristics would be the most feasible.

1.3 Methodology

After introducing into light scattering as optical phenomenon in section 2.1 and some essential basics about optical measures (section 2.2) and printing (section 2.3), the measurement setup and measurement procedure will be derived in chapter 3. First a morphological analysis of measurement setups from literature will be presented in section 3.1. From this analysis, the principle measurement setup will be derived.

For the measurement procedure, several images have to be acquired using a camera. In section 3.2, the relevant model and the constraints for the measurement will be derived. Section 3.3 introduces the detailed setup and influences on the measurement performance. In section 3.4, the measurement results are investigated with respect to anisotropy, light scattering classes, different methods to acquire the LSF and PSF, and spectral properties of light scattering.

Validating the measurement results, two alternative methods for optical dot gain measurement are compared to simulated optical dot gain based on the light scattering measurements in section 4.1 and section 4.2. A new simple prediction function for optical dot gain will be derived from a theoretical parameter study in section 4.3.

2

Basics

Light scattering in the printing substrate essentially effects the appearance of the printed product. In most cases, the printing substrate is paper. In terms of the light scattering properties, the term paper will stand as a representative for all other substrates even if they are not mentioned explicitly.

Paper is a flat material, produced from plant fibers [3]. The optical properties of paper influence the quality of a print. Here, the sub-surface light scattering is essential for the optical dot gain and thus for the reproduction of halftones.

In section 2.1, optical models will be presented that can be applied to paper. Here, the focus is set especially on models that take account for light scattering.

Some general basics on optical measures as well as ink density and color calculation can be found in section 2.2. The focus is set to measurement geometries and their influence on the reflectance measure.

Printing as a reproduction process is described in section 2.3. The composition, production and dimensions of paper being the primary printing substrate are outlined. Furthermore, the concepts of the Yule-Nielsen optical dot gain model and the Murray-Davies equation are presented.

2.1 Optics

The following sections involve the related optics for visible light. In most cases geometric optics are sufficient to describe the effects that are of importance for the work at hand. The basics are presented along the system theory for optical components.

2.1.1 Thin Medium as Optical System

A system generally consists of one or several inputs, outputs and transformations. The boundary separates the system from its surrounding. An input passes the boundary inwards, an output in the opposite direction. The choice of the boundary is existential for the behavior of the system. In the following, every

medium that interacts optically, will be treated as an optical system. Light that falls onto the medium is the input, light emerging from the medium will be treated as output. Transformations describe what happens to the light within the system's boundary. Treating the system as a black box, not knowing any physical effects that affect the transformations, a rough phenomenological description can be gained. The more the system is divided into subsystems, the more physical effects can be implemented. This way, the system can be refined to a state, where all major physical effects are modeled and all minor effects are treated phenomenologically as black boxes.

In general, optical systems can be treated as time independent.

In literature, the models for optical systems can differ in terms of light handling and dimensions [4–7]. Light handling refers to, whether the model differentiates direct and diffuse light or not. The dimensions can be either 1D, 2D, or 3D respectively.

A simple 1D model in z-direction [8] can be consulted for explaining the most important physical effects, see figure 2.1. A thin optical medium, e.g. a glass pane, optical filter, or sheet of paper, is illuminated with a known radiance L_i incident on the top side of the medium. Treating the whole system as a black box (center), the two outputs at the top and the bottom of the medium are the reflected radiance L_r and the transmitted radiance L_t. In a first step of refining, the system can be divided into three subsystems: the top interface, the volume, and the bottom interface. Top and bottom interface involve the surfaces only. The intermediate subsystem is restricted to volume only. This way, surface reflections and volume effects like absorption and scattering can be handled separately. For logically connecting the subsystems, connecting radiances have to be defined, here named after the z-position of their occurrence (subscript) and their z-direction (superscript).

Considering the top interface subsystem, input (L_i and L_0^-) and output (L_r and L_0^+) are related according to the laws of surface reflection. The direction of the reflected light depends on the orientation of the incident light relative to the surface normal. In the ideal case, the angle of reflection equals the angle of incidence. With the coefficients of surface reflection for light coming from the surrounding ρ_s and light coming from the medium ρ_m, the output can be written as:

$$L_r = \rho_s \cdot L_i + (1 - \rho_m) \cdot L_0^- \tag{2.1}$$

$$L_0^+ = (1 - \rho_s) \cdot L_i + \rho_m \cdot L_0^- \tag{2.2}$$

Surface or specular reflection depends on the index of refraction of the medium $\tilde{n}_m$ and of the surrounding $\tilde{n}_s$. For the case of normal incidence of light, the coefficient of surface reflection ρ can be expressed by Fresnel's law [9]:

$$\rho = \left(\frac{\tilde{n}_m - \tilde{n}_s}{\tilde{n}_m - \tilde{n}_s} \right)^2 \tag{2.3}$$

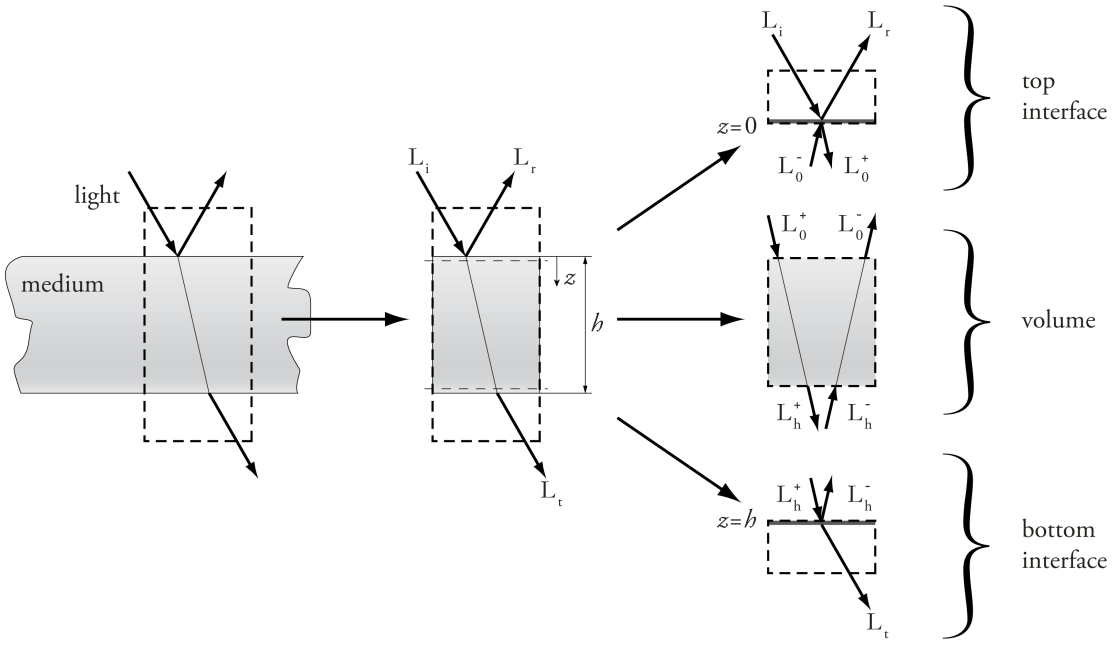

Figure 2.1: 1D system theory for thin optical components with single dimension z ([8] edited).

With varying angle of incidence γ, the surface reflection for unpolarized light increases as shown in figure 2.2 on the left. Additionally the reflection becomes different for the part of the light that is plane-polarized parallel and perpendicular to the plane of incidence respectively, as it can be seen on the right in figure 2.2. The related equations are:

$$\rho_{\parallel} = \left(\frac{\cos\gamma - \left[(\tilde{n}_m/\tilde{n}_s)^2 - \sin^2\gamma \right]^{\frac{1}{2}}}{\cos\gamma + \left[(\tilde{n}_m/\tilde{n}_s)^2 - \sin^2\gamma \right]^{\frac{1}{2}}} \right)^2 \tag{2.4}$$

$$\rho_{\perp} = \left(\frac{(\tilde{n}_m/\tilde{n}_s)^2 \cos\gamma - \left[(\tilde{n}_m/\tilde{n}_s)^2 - \sin^2\gamma \right]^{\frac{1}{2}}}{(\tilde{n}_m/\tilde{n}_s)^2 \cos\gamma + \left[(\tilde{n}_m/\tilde{n}_s)^2 - \sin^2\gamma \right]^{\frac{1}{2}}} \right)^2 \tag{2.5}$$

This theory is restricted to perfectly plane surfaces. For such media, the surface reflection can be reduced to the specular reflection. In reality, materials with perfect specular reflection are rare. In most cases, the reflection forms a lobe in approximate specular direction. A model for such a surface is to divide it into subsurfaces, which are oriented statistically. For each of these subsurfaces, the law of mirror reflection can be applied locally. From a global view, the reflection is diffuse. For a perfectly diffuse reflector, also called Lambertian reflector, the reflected radiance is constant for all directions and does not depend on the angle of incidence, see figure 2.3.

For the volume element of figure 2.1, input and output are connected by absorption and scattering

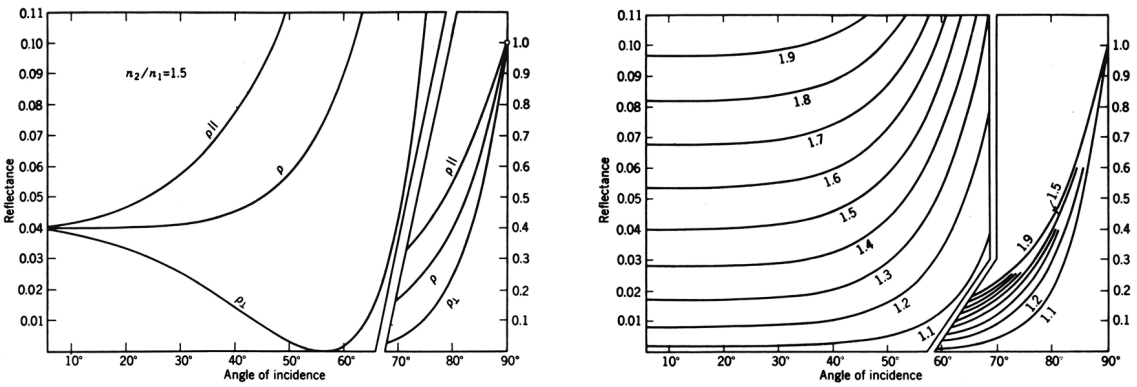

Figure 2.2: Surface reflection depends on the refractive indices of the media and the angle of incidence [9].

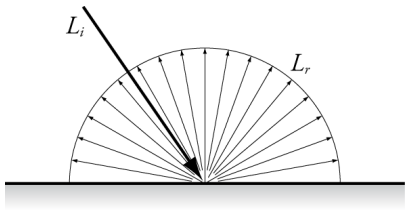

Figure 2.3: Distribution of radiance for a Lambertian reflector.

in the medium. Here, no surface effects take place. The absorption coefficient α indicates how light is decimated by absorption in the observed volume element. The longer the path length for the light, the more light is absorbed. This can be described by Lambert's law [10]:

$$L = L_i e^{-\alpha l}, \tag{2.6}$$

where L is the part of the incident light L_i that is transmitted through the volume while the absorbed part increases with the path length l through the volume element. Absorption transforms the lights energy into other forms, in most cases thermal energy [11]. A special case is the effect of fluorescence, where the energy that is absorbed is transformed into kinetic energy of the electrons of fluorescent pigments. When these relax to their ground states, they emit light, usually of different wavelengths than the absorbed light. The emitted light (by fluorescence only) depends on the incoming light L_i, the fluorescent coefficient φ, and the path length for the light that depends on the height of the volume element h:

$$L = f\left(L_i, \varphi, h\right). \tag{2.7}$$

In case of fluorescent material, fluorescence can be incorporated into the system's model. In the following, fluorescence will not be considered.

While the effect of absorption reduces the intensity, scattering causes the light to change direction. Assuming, that light comes from an arbitrary direction u, and the part that is scattered in direction v

can be described by the scattering coefficient $\varsigma_{u,v}$, the outgoing radiance depends on the input $L_{in,u}$, the scattering coefficient $\varsigma_{u,v}$, and the height of the volume element h:

$$L_{out,v} = f\left(L_{in,u}, \varsigma_{u,v}, h\right). \tag{2.8}$$

The explicit formulation depends on the definition of the volume element. Different models for scattering will be presented in section 2.1.2. A general condition for the scattering coefficients for light coming from one single direction u is that there shall be no loss of energy due to scattering:

$$\int_v \varsigma_{u,v}\,\mathrm{d}v = 1. \tag{2.9}$$

This leads to a general formulation of the output radiances L_0^- and L_h^+ of the volume element of figure 2.1 as a function of the input radiances L_0^+ and L_h^-, the absorption coefficient α, the scattering coefficients $\varsigma_{u,v}$, and the height h.

$$L_0^- = f\left(L_0^+, L_h^-, \alpha, \varsigma_{u,v}, h\right) \tag{2.10}$$

$$L_h^+ = f\left(L_0^+, L_h^-, \alpha, \varsigma_{u,v}, h\right) \tag{2.11}$$

Equations 2.1, 2.2, 2.10, and 2.11 can be combined to a system of differential equations. In this context, a multi-layer system can be derived by combining different subsystems. For example, a two layer system could be represented with the following combination: top interface – volume 1 – interface – volume 2 – bottom interface.

2.1.2 Light Scattering Models

Models that describe the optical effects in a volume element are usually integrated models including absorption, scattering, and possibly fluorescence. With the assumption of zero absorption and zero fluorescence, they can be reduced to light scattering models.

In the following paragraphs, different physical models will be presented. Due to their restricted validity for the light scattering in paper, another type of models will be concluded. These phenomenological models do not refer to the physical causes for light scattering but take the light scattering process as a whole phenomenon.

A lateral two dimensional description of the reflectance answer due to light scattering can be derived by using *point spread functions* or their Fourier transforms, the *optical transform functions*.

Physical Scattering Models

Physical scattering models are usually restricted to optically thin media. This means, that each scattering center can be regarded separately because the other centers are far away. This scattering can be described by several models. In the following, only elastic scattering will be mentioned. Inelastic scattering includes that energy is transformed and light changes its wavelength. This is contradictory to previous assumptions and to equation 2.9.

There are three types of elastic scattering for light, see figure 2.4. They are valid for different rates of circumference of the scattering center πd and wavelength λ:

- Rayleigh scattering (for $\pi d/\lambda \ll 1$)
- Mie scattering (for $\pi d/\lambda \approx 1$)
- Geometric (or optical) scattering (for $\pi d/\lambda \gg 1$)

For Rayleigh and Mie scattering the scattering centers must be perfect spheres [12, 13]. Figure 2.5 illustrates the scattering according to Rayleigh (left) and two cases of Mie scattering (center, right) for $\lambda = 550\,\text{nm}$. The curves and vectors indicate the radiation intensity of the scattering in that direction. For Rayleigh scattering, the backscattering has the same shape as the forwardly directed radiation. The bigger the ratio $\pi d/\lambda$, the more light is scattered forwards.

Although the models have very restricted applicability, there are two facts that can be derived:

1. Scattering depends on the ratio of $\pi d/\lambda$, it is a spectral quantity depending on wavelength λ.
2. Scattering changes the direction of the light's propagation. Also, back scattering in negative propagation direction can occur.

Figure 2.4: Limits of the scattering models of Rayleigh and Mie as a function of the ratio of diameter to wavelength ([14] edited).

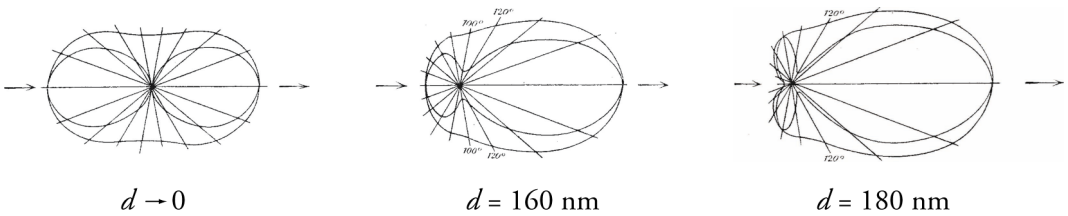

Figure 2.5: Rayleigh scattering by an infinitesimal small gold particle (left); Mie scattering by small gold particles with diameter $d = 160\,\text{nm}$ (center) and $d = 180\,\text{nm}$ (right) [12, 13].

Phenomenological Light Scattering Models

Phenomenological light scattering models describe the phenomenon light scattering without referring exactly to the causing physical principles. Therefore, these models are often not applicable to all cases but restricted to a limited field which is usually smaller than the field of application for the physical models. Phenomenological models can be adapted to a given problem by adjusting their parameters. The value of the parameters are usually not directly related to the underlying physics and cannot be derived from material characteristics. Thus, they must be adapted empirically.

The two-flux model considers the incident radiance as a diffuse irradiance I in two direction: in positive (I^+) and negative (I^-) z-direction. The change of irradiance in the medium is only influenced by absorption, which reduces the irradiance by a certain factor, and scattering, which reverses the direction of a certain part of the irradiance. The related coefficients for the model are the absorption coefficient K and the scattering coefficient S. This model is also referred to as Kubelka-Munk model [4, 5, 15, 16].

The balance of irradiances – indicated by dashed arrows on the right of figure 2.6 – yields two differential equations [6, 15]

$$\frac{\mathrm{d}I^+}{\mathrm{d}z} = -(K+S)I^+ + SI^- \tag{2.12}$$

$$\frac{\mathrm{d}I^-}{\mathrm{d}z} = (K+S)I^- - SI^+ \tag{2.13}$$

Adding collimated irradiance to the model, the number of fluxes is doubled. The four-flux model considers diffuse (I^+, I^-) and collimated irradiance (I^{c+}, I^{c-}) in positive and negative z-direction respectively, illustrated in figure 2.7. These four fluxes are coupled with scattering and absorption coefficients. The coefficients for diffuse irradiance K and S correspond to those of the two-flux model. For the collimated part of the light, three new coefficients are introduced: the absorption coefficient k and the

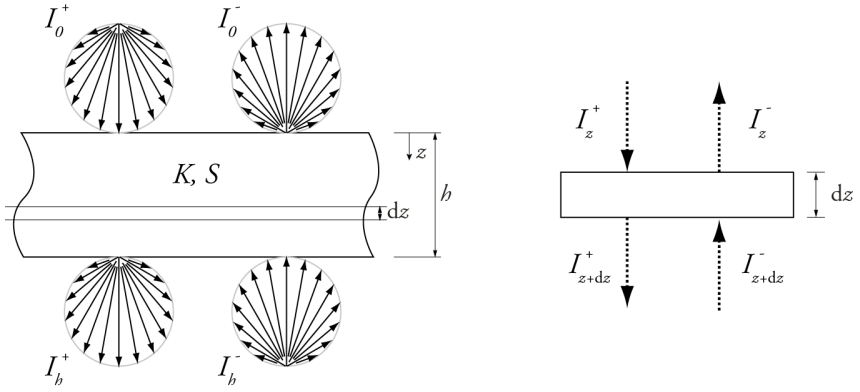

Figure 2.6: Two-flux or Kubelka-Munk model ([5, 16] edited).

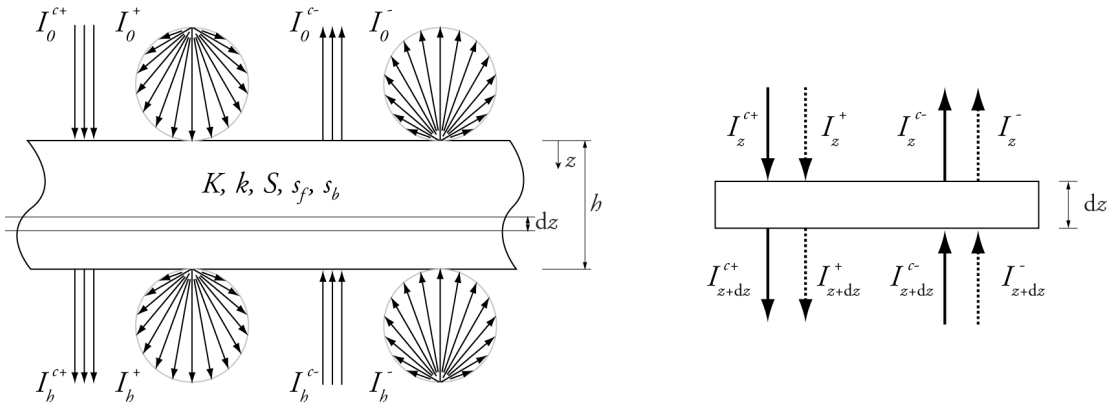

Figure 2.7: Four-flux model ([5, 16] edited).

two scattering coefficients s_f and s_b, referring to forward (f) and backward scattering (b) respectively. With scattering, the amount of diffuse light is increased, while the amount of collimated light decreases. The balance of irradiances is illustrated on the right hand side of figure 2.7, where the solid arrows now refer to collimated light. The differential equations for this model are [15]

$$\frac{\mathrm{d}I^{c+}}{\mathrm{d}z} = -(k + s_f + s_b)I^{c+}, \tag{2.14}$$

$$\frac{\mathrm{d}I^{c-}}{\mathrm{d}z} = (k + s_f + s_b)I^{c-}, \tag{2.15}$$

$$\frac{\mathrm{d}I^{+}}{\mathrm{d}z} = -(K + S)I^{+} + SI^{-} + s_f I^{c+} + s_b I^{c-}, \tag{2.16}$$

$$\frac{\mathrm{d}I^{-}}{\mathrm{d}z} = (K + S)I^{-} - SI^{+} - s_f I^{c-} - s_b I^{c+}. \tag{2.17}$$

Berg's extended Kubelka-Munk model [6] is an extension of the two-flux model with a second dimension, see figure 2.8. As in the two-flux model, only two fluxes are considered for the z-direction (irradiance M and exitance E) but the dimensional extension requires two additional fluxes S_+ and S_- in positive and negative x-direction respectively, see figure 2.8. S_+ and S_- are caused by scattering and must be added or subtracted from the cells next to the observed element. Since the z-direction is perpendicular to the surface, Berg's model allows only for a one-dimensional lateral description of scattering. The differential equations for this model can be found at Berg [6].

Adding another dimension with another two fluxes, Mourad's extension [7] serves as a full 3D description for light scattering, absorption, and fluorescence, as illustrated in figure 2.9 on the left. The model can also be formulated in polar coordinates, as shown in figure 2.9 on the right. Here, isotropic scattering is assumed. In this case, the light transferred from one cell to its angular neighbor compensates the light exchange with the neighbor on the other side.

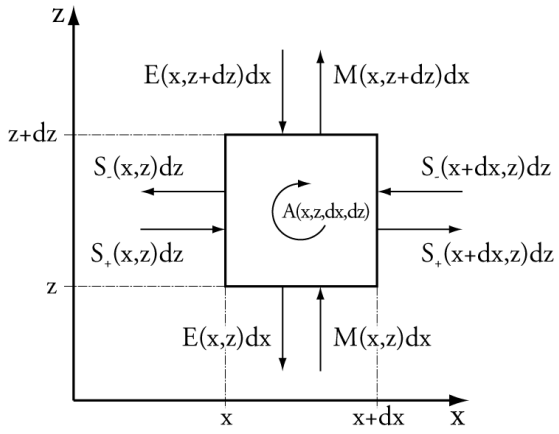

Figure 2.8: Berg's extended 2D Kubelka-Munk model ([6] edited).

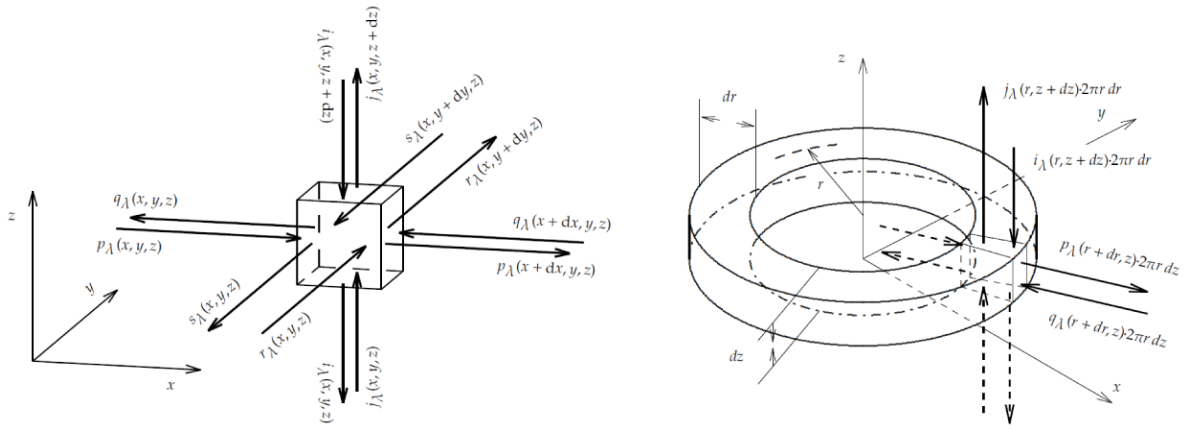

Figure 2.9: Mourad's extended 3D Kubelka-Munk model [7].

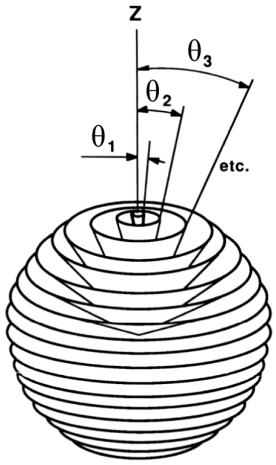

Figure 2.10: Many-flux model [5].

The models presented could be refined, adding even more directions. This leads to the many-flux model [15], an illustration of 22 channels [5] is shown in figure 2.10. For calculations, the many-flux model is usually too complex, since for each transition between the channels a coefficient has to be defined and the number of differential equations increases, so that the adaption to a given problem becomes difficult.

PSF as Reduced Lateral Light Scattering Model

A common description of light scattering is the use of *point spread functions* (PSF). In this case the PSF can be considered as a "probability density function that describes the probability of a photon returning to the surface of the [medium] at a location (x,y) away from the point of entry into the [medium]" [17].

This approach differs to the phenomenological approaches presented previously. The simplest models only distinguish direct and diffuse light, as in the two- and the four-flux model. Cellular models like Berg or Mourad consider scattering as a transport phenomenon of light to the direct neighbor cell. The PSF according to Arney et al. [17]. allows light to be transported also into cells some distance away from the source cell without solving the whole model. This is achieved by convoluting the original light pattern that just entered the medium $L_0^+(x,y)$ with the PSF $\mathcal{P}(x,y)$:

$$L_0^-(x,y) = \left(L_0^+ * \mathcal{P}\right)(x,y), \tag{2.18}$$

where $*$ is the convolution operator and $L_0^-(x,y)$ the lateral distribution of the light about to return through the surface again.

For a point source, the PSF directly describes the reflectance answer of a scattering medium as it is shown in figure 2.11 on the left. In case of a line source, the direct answer is called the *line spread function* (LSF), see the illustration in the center of figure 2.11. Mathematically, the LSF $\mathcal{L}(x)$ can be obtained in two ways: first by convoluting the PSF with a line source, or second, by integrating the PSF in one direction:

$$\mathcal{L}(x) = \int_{-\infty}^{\infty} \mathcal{P}(x,y)\ \mathrm{d}y \tag{2.19}$$

In many cases, the PSF in characterized using polar coordinates. Then the transformation equation can be written using the Abelian integral, presuming isotropic scatter:

$$\mathcal{L}(x) = 2 \cdot \int_{x}^{\infty} \mathcal{P}(r) \frac{r}{\sqrt{r^2 - x^2}}\ \mathrm{d}r. \tag{2.20}$$

For the general derivation of this equation see Marchand [18, 19]. For the special case used here, see appendix A.2. The inverse equation of 2.20 is:

$$\mathcal{P}(r) = -\frac{1}{\pi} \int_{r}^{\infty} \frac{\mathcal{L}'(x)}{\sqrt{x^2 - r^2}}\ \mathrm{d}x. \tag{2.21}$$

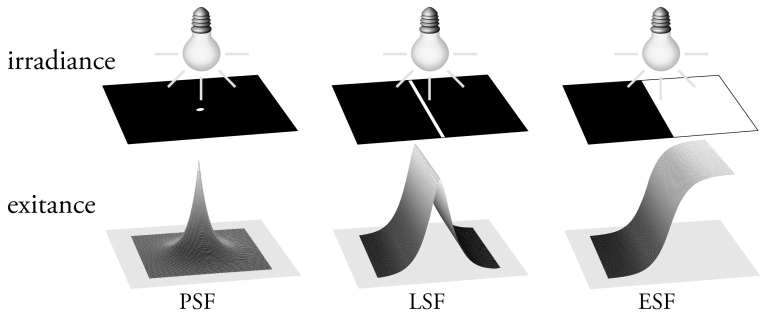

Figure 2.11: PSF, LSF and ESF [1].

Another important case for the PSF is a halfplane, edge-shaped illumination, as it can be seen in figure 2.11 on the right. In this case, the reflectance answer is the *edge spread function* (ESF) $\mathcal{E}$. The relation between LSF and ESF is defined by differentiation and integration respectively:

$$\mathcal{E}(x) = \int_{-\infty}^{x} \mathcal{L}(u)\ \mathrm{d}u \tag{2.22}$$

$$\mathcal{L}(x) = \frac{\mathrm{d}}{\mathrm{d}x}\mathcal{E}(x) \tag{2.23}$$

Optical Transfer Function

Transferring equation 2.18 into the frequency domain by taking the Fourier transform $\mathcal{F}$ leads to:

$$\mathcal{F}[L_0^-(x,y)] = \mathcal{F}\left[\left(L_0^+ * \mathcal{P}\right)(x,y)\right], \tag{2.24}$$

$$\mathcal{F}[L_0^-] = \mathcal{F}[L_0^+] \cdot \mathcal{F}[\mathcal{P}], \tag{2.25}$$

where the Fourier transform of the PSF is called the *optical transfer function* (OTF) [20] of the system

$$\mathrm{OTF} = \mathcal{F}[\mathcal{P}] \tag{2.26}$$

and is normalized to unit value at zero spatial frequency. Generally, the OTF is a complex function. Its magnitude is referred to as *modulation transfer function* (MTF) and its phase is called the *phase transfer function* (PTF) [20].

$$\mathrm{MTF} = |\mathrm{OTF}| \tag{2.27}$$

$$\mathrm{PTF} = \arg\left(\mathrm{OTF}\right), \tag{2.28}$$

The MTF is an important metric for describing resolution characteristics of an imaging system, where the components of the system can be incorporated as a mathematical product. Components can be for example lenses, windows, but also paper and other optical media [21].

2.2 Optical Measurements

Optical measures do not directly correspond to the physical effects described above. They strongly depend on the measurement setup. Therefore, the general definitions and conditions are mandatory information for reproducible measurements.

2.2.1 Optical Measures

The most common optical measures are reflectance R and transmittance T. In contrast to the coefficients for absorption, fluorescence, scattering, and surface reflection, these measures are no material constants since they are a combination of physical effects and not one effect only. Additionally, the values for reflectance and transmittance can vary for the same material depending on the measurement setup or method used for their determination. According to Judd, reflectance can be defined as the "ratio of some specified portion of the reflected flux to incident flux" [22]. Applying this definition to the optical system in figure 2.1, reflectance (and accordingly transmittance) can be defined as

$$R = \frac{L_r}{L_i} \tag{2.29}$$

$$T = \frac{L_t}{L_i} \tag{2.30}$$

Both measures depend on a combination of surface reflection, absorption, and scattering, in some special cases, effect pigments can cause interference [23, 24]. The isolated physical effects are hardly measurable. Therefore, reflectance and transmittance can be used to determine these material constants indirectly.

Since diffuse surface reflection and scattering can alter the directional distribution of reflected or transmitted radiance, both measures depend on the measurement geometry, i.e. the directions of incidence (index i) and detection, where reflectance is denoted by index r and transmittance by index t. Figure 2.12 shows the general definition of the measurement geometry for reflectance measurements. Each direction is defined by its polar angle θ relative to surface normal, its azimuth ϕ, and its solid angle element $\mathrm{d}\Omega$ [25].

Covering the full hemisphere of incident and detection angles, a *bidirectional reflectance distribution function* (BRDF) can be obtained. It contains the reflectance (per steradian) for each pair of directions [25]. For transmittance, the function is named BTDF (*bidirectional transmittance distribution function*).

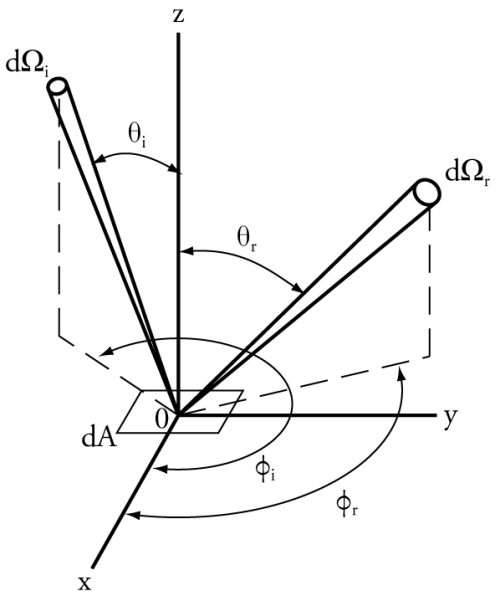

Figure 2.12: Geometry for reflectance measurements ([25] edited).

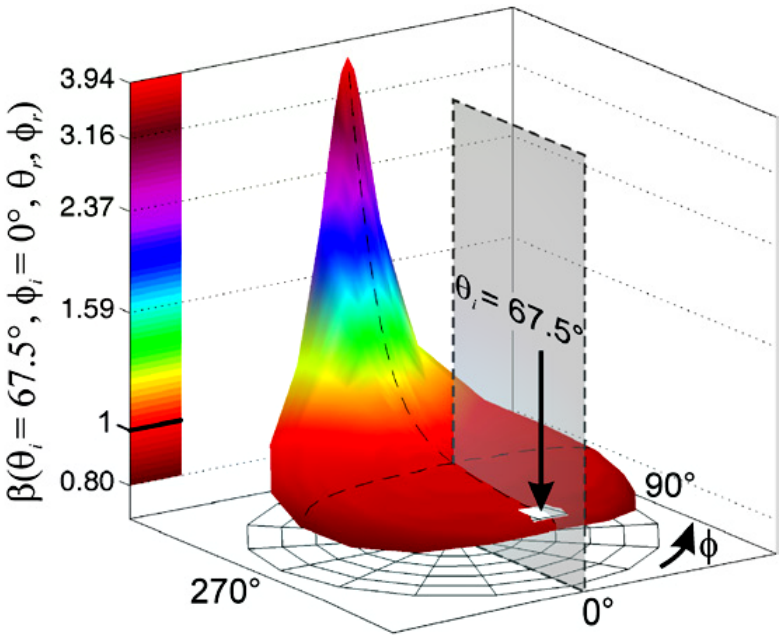

Figure 2.13: Three-dimensional reflection indicatrix of the radiance factor β; matt-sided opal glass, incident geometry $\theta_i = 67.5°$, wavelength $\lambda = 550\,\text{nm}$ [26].

Illustrating a BRDF means always a reduction in some terms. As example, figure 2.13 shows the reflectance of a matt-sided opal glass for one direction on incidence $\theta_i = 67.5°$, $\phi_i = 0°$ and one wavelength $\lambda = 550\,\mathrm{nm}$ (solid angles of incidence $\mathrm{d}\Omega_i = 2.16 \times 10^{-2}\,\mathrm{sr}$ and detection $\mathrm{d}\Omega_r = 96.45 \times 10^{-6}\,\mathrm{sr}$) [26]. The radius of this illustration is the polar angle θ (relative to the surface normal). The z-axis is the radiance factor β, measured for $\theta_r = 0°$ to 80° and $\phi_r = 0°$ to 360°.

A perfect Lambert reflector would show a constant radiance factor $\beta = 1$ for all measurement geometries. The radiance factor for a perfect mirror reflector would be equal to zero for all but the specular direction. This illustration makes clear, why differences in the solid angle can affect the measurement. Therefore, three types of solid angles can be distinguished [5, 27]:

- Hemispherical or diffuse: the solid angle covers the full hemisphere.
- Conical: the solid angle is small, it forms a cone.
- Directional: incidence or detection are parallel or quasi-parallel.

In contrast to conical or directional measurements that are specified using the polar angle, a hemispherical or diffuse measurement geometry is specified with "d". Combining all possible types of solid angles for incidence and detection, nine types of measurement conditions can be distinguished. For reflectance these are given in table 2.1.

These cases will not be distinguished in the following and all measurements will be referred to as reflectance measurements. For reasons of comprehensibility all necessary information will be provided.

Illumination	**Detection**	**Quantity**	**Symbol**
hemispherical			ρ_{dif}
conical	hemispherical	reflectance	ρ_c
directional			ρ_g
hemispherical			R_{dif}
conical	conical	reflectance factor	R_c
directional			R_g
hemispherical			β_{dif}
conical	directional	radiance factor	β_c
directional			β_g

Table 2.1: Nine types of reflectance measurements according to DIN 5036-3 [5, 22, 27].

2.2.2 Color Measurement and Calculation

Although, handling color as an optical property of an object is not truly accurate, color will be reduced to the optical aspect in the following. For the aspect of human vision and psychophysics, the reader is

referred to Valberg [28].

The aim of a color measurement is to process the optical measure in order to derive a correlate to the visual appearance of the object. Thus, color measurement can refer to reflectance and transmittance. The following section will be limited to reflectance measurements only.

Typical measurement geometries for color measurements in graphic industries are conical-conical setups at $0^\circ/45^\circ$ or $45^\circ/0^\circ$ and hemispherical-conical setups at $d/0^\circ$ or $d/8^\circ$. The conical angles of aperture are restricted to a maximum of 5°, which equals a solid angle of $0.006\,\mathrm{sr}$ [27, 29].

Generally, color measurements consist of a spectral reflectance measurement and a subsequent calculation of color values. This process is illustrated in figure 2.14. The first step of color calculation is to derive the *CIE tristimulus values* X, Y, Z (CIEXYZ) according to the following equations [9]:

$$X = k \int_\lambda R(\lambda)\, S(\lambda)\, \overline{x}(\lambda)\ \mathrm{d}\lambda \tag{2.31}$$

$$Y = k \int_\lambda R(\lambda)\, S(\lambda)\, \overline{y}(\lambda)\ \mathrm{d}\lambda \tag{2.32}$$

$$Z = k \int_\lambda R(\lambda)\, S(\lambda)\, \overline{z}(\lambda)\ \mathrm{d}\lambda \tag{2.33}$$

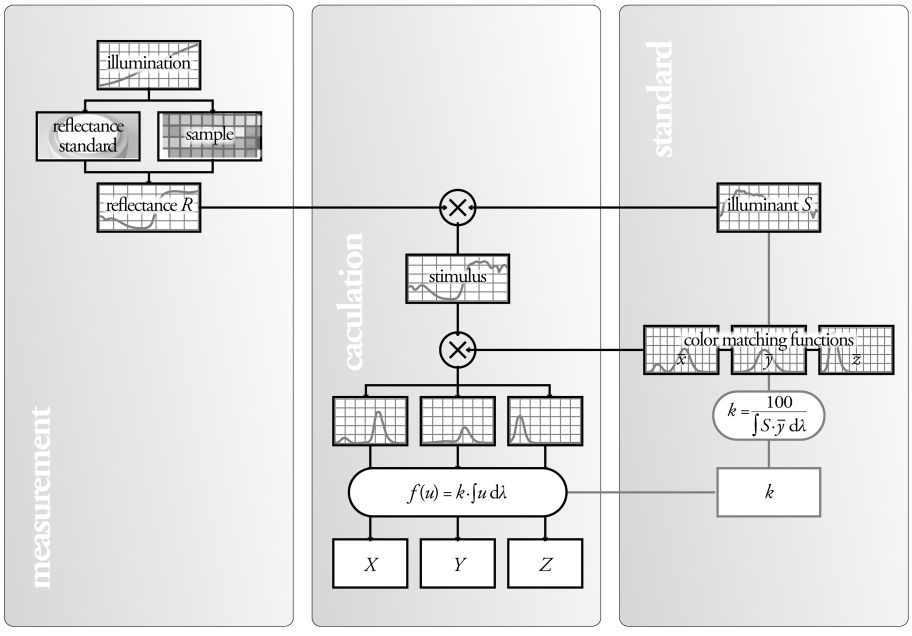

Figure 2.14: Process of color measurement and calculation ([30] translated).

where k is a normalizing factor defined as

$$k = \frac{100}{\displaystyle\int_\lambda S(\lambda)\, \overline{y}(\lambda)\ \mathrm{d}\lambda} \tag{2.34}$$

The tristimulus values X, Y, and Z are functions of the measured reflectance R, the light spectrum S, and the color matching functions $\overline{x}$, $\overline{y}$, and $\overline{z}$ defined by CIE in 1931 for the 2° standard observer [31].

In a second step, the tristimulus values X, Y, Z are, in the general case, converted into an approximately uniform color space, where the correlation between the Euclidean distance of color values and the perceived color difference is better. The widest spread is the CIE L^*, a^*, b^* color space (CIELAB) color space, defined by CIE in 1976. The CIELAB color values are a lightness correlate L^*, a red-green component a^*, and a blue-yellow component b^*. These quantities are calculated relative to the CIEXYZ color values of the light X_n, Y_n, Z_n [9]:

$$
\begin{aligned}
L^* &= \begin{cases} 903.3 \cdot \dfrac{Y}{Y_n} & \text{if } \dfrac{Y}{Y_n} \leq 0.008856 \\ 116 \cdot \left(\dfrac{Y}{Y_n}\right)^{1/3} - 16 & \text{else} \end{cases} \\
a^* &= 500 \cdot (Q_X - Q_Y) \\
b^* &= 200 \cdot (Q_Y - Q_Z) \\
\text{with } Q_A &= \begin{cases} 7.787 \cdot \dfrac{A}{A_n} + \dfrac{16}{116} & \text{if } \dfrac{A}{A_n} \leq 0.008856 \\ \left(\dfrac{A}{A_n}\right)^{1/3} & \text{else} \end{cases} \\
&\text{where } A = X, Y, Z.
\end{aligned}
\tag{2.35}
$$

There are various attempts to enhance the uniformity of color spaces. One approach is the formulation of better *color-difference formulas* (CDF), like CIE94, CIEDE2000, or CMC. CDFs are usually applied to CIELAB or its polar equivalent CIE L^*, C^*, h^* color space (CIEXYZ). Then the colors are not transferred into a different color space but the color difference is an adapted formula that varies over the whole color space in contrast to the Euclidean distance that is location-independent. The corresponding equations can be found in literature [32].

A different approach is the formulation of color-appearance models like CIECAM02. Here, visual effects like chromatic adaption can be implemented and enhance color matching [32].

2.2.3 Densitometry

Optical density originally refers to the darkness of a light sensitive medium, i.e. a photographic film. It is a measure of the absorption characteristics of the sample – the higher the absorption, the higher the optical density. The optical density can be calculated from reflectance or transmittance measurements as the reciprocal of the measure. In the following, the term densitometry will be restricted to the reflectance measurement as it is common in printing industry as a correlate for the ink film thickness [33].

The density measurement on printed products is standardized [34]: illumination, measurement geometry, weighting functions, and the calculation of the density are fixed. This standardized measure will be called the ink density in the following.

Ink density is a relative measure of weighted reflectances. Two measurements are taken: one on the sample patch $R_s(\lambda)$, the other on the unprinted substrate $R_p(\lambda)$ where index p refers to paper being the most common printing substate. The measurement geometry is set to be $0^\circ/45^\circ$ or $45^\circ/0^\circ$ respectively. Also, the use of polarizing filters is regulated. Both, measurement geometry and polarizing filters aim at reducing the detected surface reflections that would distort the measurement [34, 35]. Standard illumination is an incandescent light with spectral distribution $S(\lambda)$ according to standardized illuminant A [36].

Since printing inks differ in their spectral absorption characteristics, weighting functions $w_i(\lambda)$ restrict the evaluated wavelengths to the range where the ink i has highest absorption. These weighting functions are standardized for the four process inks cyan, magenta, yellow, and black. For example, they can be implemented by using different color filters. With these conditions, the ink density D can be calculated from the reflectance [34]:

$$D = -\log_{10}\left(\int_\lambda w_i(\lambda)S(\lambda)R_i(\lambda)\ \mathrm{d}\lambda\right). \tag{2.36}$$

In printing, it is common to use the relative density D', such that paper density D_p is set to zero:

$$D' = D - D_p. \tag{2.37}$$

The relative ink density can be expressed in basic densities or reflectances respectively:

$$D'_i = D_i - D_p. \tag{2.38}$$

$$D = -\log_{10}\left(\frac{\int_\lambda w_i(\lambda)S(\lambda)R_i(\lambda)\ \mathrm{d}\lambda}{\int_\lambda w_i(\lambda)S(\lambda)R_p(\lambda)\ \mathrm{d}\lambda}\right). \tag{2.39}$$

2.3 Printing

Printing is the process of transferring a material (liquid ink or solid toner) onto a printing substrate (e.g. paper or foil). In general, the result is a laterally structured print where printed and unprinted elements alternate. There are four input elements [37] that participate in the process (figure 2.15): the two materials printing ink or toner and printing substrate, the layout defining the lateral distribution of printed and unprinted elements, and the energy that is responsible for the material's transfer onto the printing substrate.

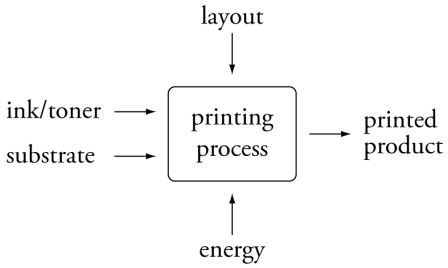

Figure 2.15: Printing process ([37] edited).

Examples for conventional printing processes are offset, flexography, gravure, and screen printing. Most important digital processes are inkjet and electrophotography printing. Each process demands different properties from the materials and the layout, so that there are special inks for each of the processes and even some special papers, e.g. for injekt printing.

When liquid ink is transferred onto the printing substrate, some part of the ink permeates the substrate. With this, the optical properties of the remaining ink on top of the substrate change, as do the optical properties of the penetrated substrate. For different printing processes, this is a desired or an unwanted effect. Therefore, the printing substrates can be designed to fit the needs of the different processes.

2.3.1 Printing Substrates (Paper)

The major printing substrate is paper. Papers are sheets of cellulose fibers that are mostly gained from wood, from fiber crops or can be recycled from waste paper. The dimensions of the fibers differ noticeably, see table 2.2.

Fiber type	**Fiber length** / mm	**Fiber diameter** / µm
softwood	1.1 – 9.3	14 – 65
hardwood	0.3 – 2.7	10 – 44
cotton	25	20
other	1.1 – 2.7	9 – 20

Table 2.2: Dimensions of fibers used for paper production [38–41].

Fillers increase the opacity of paper, having a diffraction index different from the one of the paper fibers [38]. These components are e.g. pigments like kaolin, clay, calcium carbonate, or titanium dioxide [40]. The dimensions of these pigments are small compared to the dimensions of the fibers. Figure 2.16 compares the dimensions of wood fibers and fillers.

Other components of paper are additives that control the mechanical and chemical characteristics of paper.

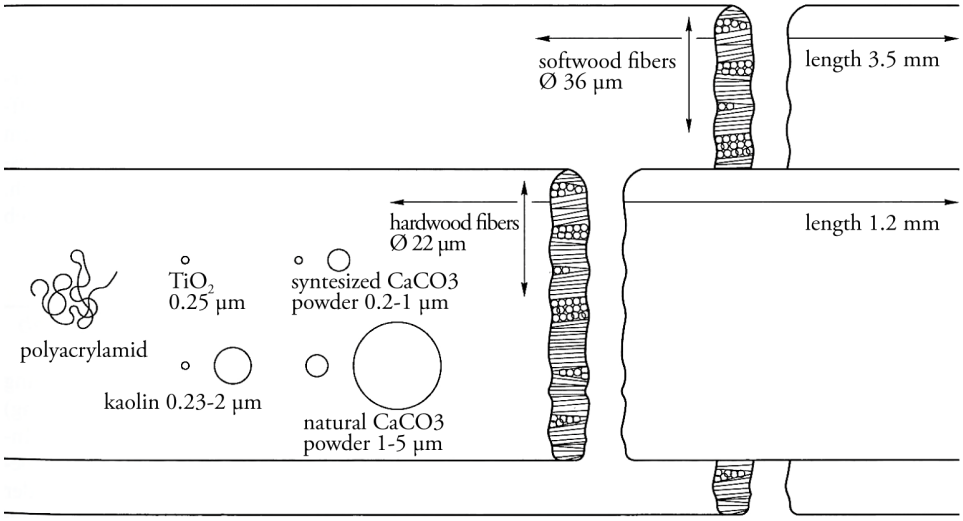

Figure 2.16: Dimensions of fibers and some fillers ([40] translated and corrected).

During paper production, the fibers are mostly aligned in process direction. A slight jogging motion of the carrier wire reduces this grain direction to some extend [3]. Paper production also includes pressing and calendering, where the surface is evened. After that, papers can be coated. A layer of material including pigments is applied to the surface of the paper. The pigment types are the same as for the fillers, but the sizes are slightly smaller [38, 40, 41]. The coated paper can be calendered again achieving satin finish or special structures using an embossing calender [3]. For highly glossy surface finish, the paper is cast-coated. Then the calender is replaced by contact drying using a chrome cylinder that transfers its smooth surface to the coating [3].

This way, the surface geometry of paper can be designed. Its roughness can vary from some hundred nanometers for coated papers up to several microns for uncoated papers [42] e.g. for newspapers. A comparison of different papers and their roughness can be found in figure 2.17.

Coatings increase the opacity of paper so that the optical influence of the fibers is reduced. Figure 2.18 shows micrographs in transmission mode of a standard uncoated office paper and a matte coated fine art paper. Both images were postprocessed in order to enhance the contrast. For the uncoated paper on the left, the fibers can be seen clearly. The fibers of the coated paper on the right are only visible as blurred shapes due to the high opacity of the coating.

Special coatings can be found for inkjet papers. Their aim is to absorb the ink and keep it in the upper regions of the coating. In optical sense, these coatings can hardly be compared to coatings of fine art papers.

Another important type of printing substrates is foil. Foils usually do not absorb ink. Their structure is not as inhomogeneous as paper. During their production, foils are stretched. This is the reason for

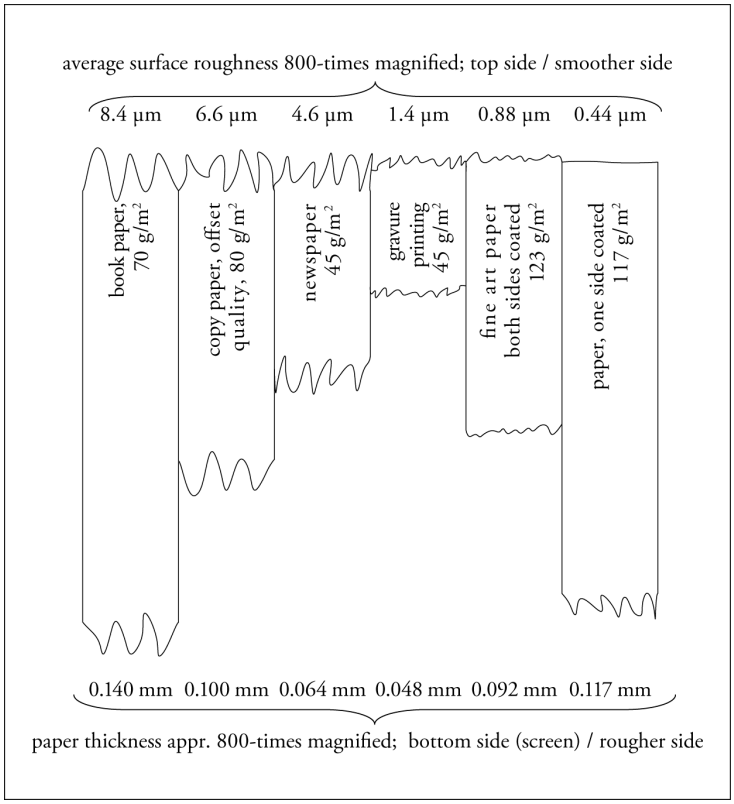

Figure 2.17: Comparison of the surface roughness of six papers with varying smoothness; approximately 800-times magnification ([42] translated).

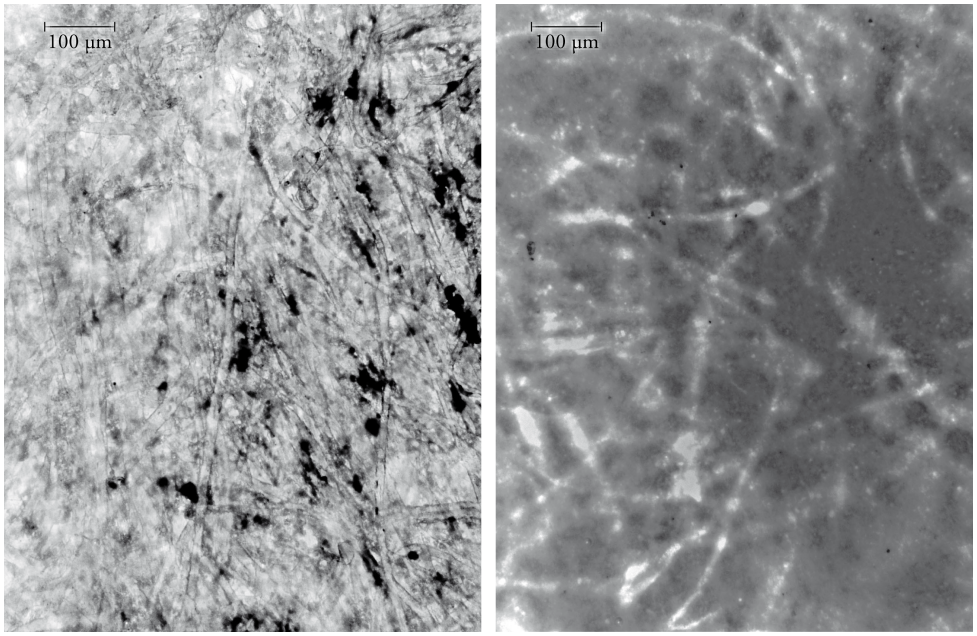

Figure 2.18: Micrographs of an uncoated (left) and a matte coated paper (right) in transmission mode.

foils having a slight polarizing effect. Foils as printing substrates will not be investigated in this research. Nevertheless, they should be considered in future examinations.

2.3.2 Reproduction of Halftones

Most printing processes do not allow to vary the ink thickness purposefully to produce different halftones. Thus, screening technologies are used to print halftones.

The number of inks is usually restricted to the four process colors cyan, magenta, yellow, and black (CMYK). These can be printed next to or on top of each other (overprint). This results in four primary colors, six secondary colors of the overprint of two inks, four tertiary colors and one color resulting from the overprint of all inks.

The number of solid colors increases exponentially with the number of inks. Figure 2.19 shows a model for this fact, using Pascal's triangle. The apex shows the number of zero inks. In this case, the only color possible is the color of the printing substrate, i.e. the white color of the paper. One ink allows for two possible colors: the substrate color and the color of the solid ink. In case of two inks, the additional overprint of the two inks adds a secondary color to the two primary colors of the solid inks and the paper's color, and so on. For the number of n inks, 2^n combinations are possible.

In conventional printing processes, additional inks are usually used for corporate colors and not for color separation. Nevertheless, the number of digital printers using more than four colors is increasing. Examples are the addition of light inks for a better reproduction of pastel colors or expanding the color gamut using additional red, green, and blue ink.

The correct image reproduction requires the reproduction of halftones. These are achieved by printing a high frequency of small dots. The screening technologies for building the dots can be divided into

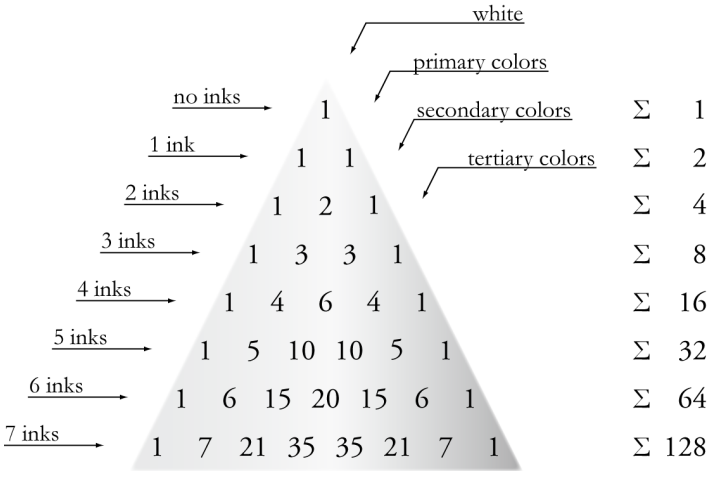

Figure 2.19: Pascal's triangle representing the number of possible colors as combination of inks.

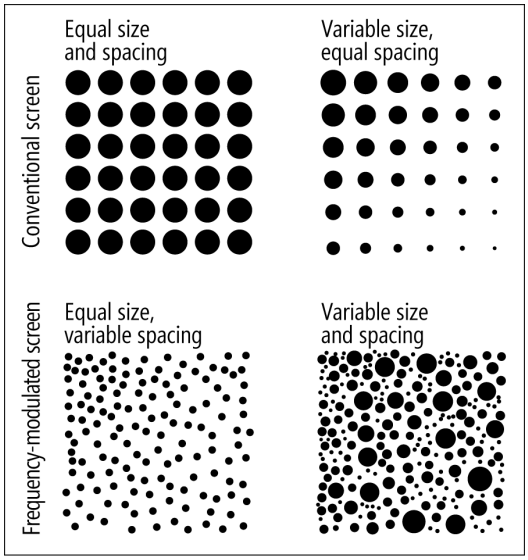

Figure 2.20: Screen types for the reproduction of halftones [3].

conventional screens with variable dot size and fixed dot spacing (AM: *amplitude modulation*), *frequency modulated* screens (FM) with fixed dot size and variable spacing, and hybrid technologies using variable dot size and variable spacing (see figure 2.20).

The screen frequency f_s is a measure for the coarseness of the grid. It is usually specified in lines per centimeter l/cm or lines per inch lpi. In contrast to this, the addressability of digital printers is specified in dots per inch (dpi). The dot pitch (in µm) is a measure for the distance between two printed dots and therefore the reciprocal of the screen frequency for conventional screens, or the addressability for FM screens.

The reproduction of true halftones using varying thickness of the ink can only be found in gravure and, restricted, in inkjet printing. Apart from this, conventional screens are generally used for conventional printing processes, frequency modulated or hybrid screens can be found in digital printers.

The differentiation of screening techniques is important when investigating *optical dot gain* (ODG). Halftones seem to have higher coverage than the dimensions of the dots would imply, caused by subsurface light scattering. This effect is also called the *Yule-Nielsen effect* [43]. Here, the mean distance between or the mean diameter of the dots is an important factor. The smaller these values, the higher the ODG. Since FM screens use smaller dots than AM screens, the effect is more visible, here. Only true halftones by varying ink film thickness can be free from ODG, if the printed structures are large compared to light scattering.

2.3.3 Monochrome Halftone Models

In printing, the prediction of the final print from the original layout is a key element for high quality prints. By means of halftone models, the reflectances of a printed halftone R_A can be calculated from the fractional area coverages A of the layout, a reflectance measurement of the printing substrate R_p, and a reflectance measurement of the solid ink R_i. In the following, the models will be restricted to monochrome models, since in multicolor printing, other effects like ink spreading arising from overprints have to be considered [44].

With the assumptions of negligible light scattering – both, in the substrate and in the ink – and constant ink thickness for the dots, the Murray-Davies [45] equation gives the simplest formulation of a halftone model:

$$R_A = A \cdot R_i + (1 - A) \cdot R_p. \tag{2.40}$$

The inverse Murray-Davies equation can be used to calculate the fractional area coverage from a measured reflectance or relative ink density respectively:

$$A = \frac{R_A - R_p}{R_i - R_p}, \tag{2.41}$$

$$A = \frac{1 - 10^{-D'_A}}{1 - 10^{-D'_i}}. \tag{2.42}$$

where D'_A and D'_i are the relative ink densities of the halftone (index A) and the solid ink (index i) respectively, according to equations 2.36-2.39. The Murray-Davies model does not account for ODG and is therefore often afflicted with significant errors. Yule and Nielsen [43] corrected the inverse Murray-Davies equation introducing a factor n that can vary for different papers. The correction was applied to the densities in equation 2.42:

$$A = \frac{1 - 10^{-D'_A/n}}{1 - 10^{-D'_i/n}}. \tag{2.43}$$

which yields to the following equations using reflectances:

$$A = \frac{\sqrt[n]{R_A} - \sqrt[n]{R_p}}{\sqrt[n]{R_i} - \sqrt[n]{R_p}}, \tag{2.44}$$

$$R_A = \left(A \cdot \sqrt[n]{R_i} + (1 - A) \cdot \sqrt[n]{R_p}\right)^n. \tag{2.45}$$

Let us assume that the fractional area coverage of the printed halftone really equals the nominal coverage A_n of the original layout. Then, the perceived or measured coverage according to the Murray-Davies equation can be called *effective coverage* A_e. The optical dot gain ΔA is defined as their difference:

$$\Delta A = A_e - A_n. \tag{2.46}$$

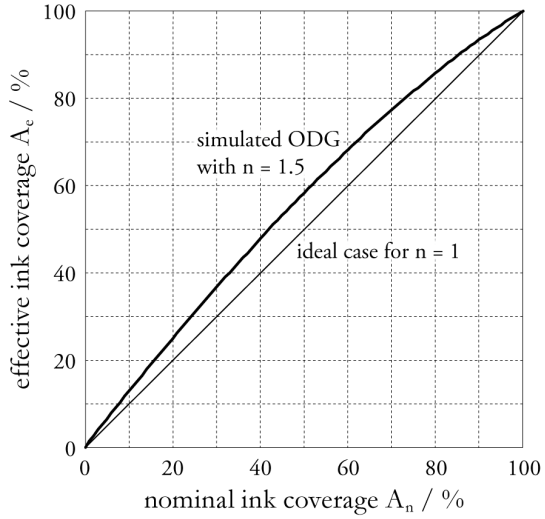

Figure 2.21: Tone response curve for printing with simulated dot gain with $n = 1.5$.

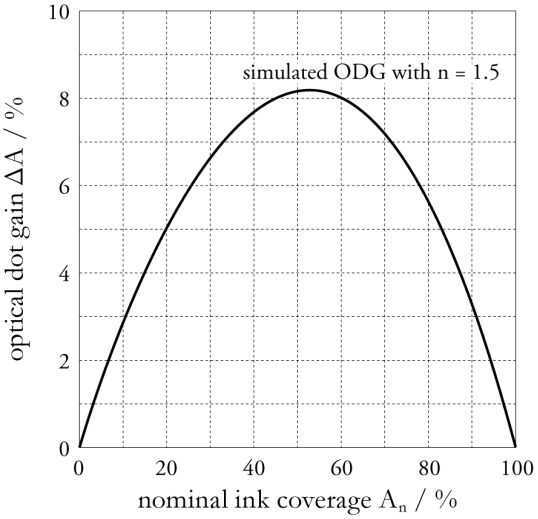

Figure 2.22: Dot gain curve for simulated optical dot gain with $n = 1.5$.

Since ODG depends on the frequency and the diameter of the dots, ΔA depends on the nominal area coverage A_n. The tone response curve shows the effective over the nominal area coverage, as shown in figure 2.21. For the dot gain curve (figure 2.22), the dot gain is plotted over the nominal area coverage. For calculating the reflectance of the halftones, the Yule-Nielsen model was used assuming $n = 1.5$.

In terms of optical dot gain, the use of nominal area coverages can be the source of errors. During the printing process, the size and shape of the dots can change. Therefore, an additional term will be introduced, called the *geometrical area coverage* A_g in the following. This term refers to the real fractional coverage of the ink on the substrate. In contrast to this, the nominal area coverage is the intended coverage from the digital layout. This way, the optical dot gain, that truly refers only to light scattering and no other effects, has to be calculated from the difference between geometrical and effective coverage:

$$\Delta A = A_e - A_g. \tag{2.47}$$

Then equation 2.46 includes, – among ODG– also ink spread on the paper or other physical dot gain effects.

3

Measurement of Light Scattering Properties of Paper

In literature, some measurement setups can be found that either acquire the *point spread function* (PSF) or the *modulation transfer function* (MTF) of printing papers. In section 3.1 a morphological analysis of these literature sources is given from which the principle measurement design of this research is derived.

In section 3.2 the necessary captures, that are needed for the measurement, will be derived. In this course, some important constraints for the image capture will be deduced. In addition, approaches to calculate the *line spread function* (LSF) and the PSF from the measured *edge spread function* (ESF) will be presented.

A detailed description of the experimental setup can be found in section 3.3. Furthermore, some essential influences on the measurement performance will be analyzed.

Section 3.4 presents the measurement results that were derived with the setup introduced. These results are analyzed according to anisotropy, a possible classification of light scattering, the two major approaches of deriving LSF and PSF, and some spectral aspects of light scattering.

3.1 Principle Design of the Measurement Setup

Generally, the measurement of light scattering properties of paper and similar media follows some common rules. The sample is illuminated by a known lateral pattern of light. It is important that light regions alternate with dark regions. Usually, the capture of the "answer" of the sample is the lateral capture of its reflectance. The more the reflected light resembles the incident light, the less light is scattered in the sample. Of course, there are some challenges due to surface reflections and distortions in the measurement system. But generally, the essential elements of the measurement procedure are as described. However, there is also a special case which is called *contact method*, where no lateral capture is needed, but the

reflectance is measured area-integrated. Furthermore, measurements can be based on the Kubelka-Munk model [4] using black and white backings. Such measurements will not be considered in the following. The interested reader is referred to Ackermann et al. [46].

In the following chapter, the essential elements of procedures for light scattering measurements will be discussed. Examples from literature will be analyzed with respect to their use of these elements. The results of the analysis will be summed up in a morphological analysis from which the principle measurement design for this work will be derived.

3.1.1 Review of Literature

In literature, some publications on the measurement of light scattering in paper can be found, starting with Yule and Nielsen in 1951 [43]. The different sources were analyzed according to their method of light pattern generation, their pattern type, their method of detection, and their measurement geometry. The information from literature were collected in table 3.1. Entries marked with *not defined* (ND) are not defined in the sources. Additional investigations were performed on the spectral design and the possible use of polarizing filters. Due to little information in the sources, these aspects were not included into table 3.1.

Design of the Light Pattern

The light pattern is an essential element of the measurement. As described in chapter 2, scattering is a volume related effect. Within the volume of the material, scattering makes the light change direction. This way, it can be transferred to a different location than the one of its entry and exit there. The easiest way to observe this effect is to generate light and dark regions in a defined pattern. A perfectly reflecting, no-scattering material would show the same lateral distribution of reflectance like the pattern of incidence. Scattering makes light travel from the illuminated regions to the dark regions to some extent. This way, light regions become darker and dark regions become lighter. The comparison of the pattern of light incidence with the lateral reflectance indicates the extent of light scattering in the material. Therefore, a defined light-dark-pattern is important to detect light scattering.

In literature, there are different designs of light patterns. One of the earliest measurements of light scattering in paper was performed by Yule and Nielsen [43]. They projected the light filament of a halogen lamp onto the paper (figure 3.1a). The light filament formed the illuminated part, the rest of the detected area was dark. Later, Yule et al. [47] altered their measurement setup and used a knife edge to generate a sharp transition between a light and a dark half-plane. This can also be found in the work of Ackermann et al. [46]. Other versions of half plane light pattern were realized by Arney et al. [17] using a glass plate that was covered to its half with a chrome layer (figure 3.1b) and Engeldrum and Pridham [49], using a photographic film. A basic approach is the reduction of the light area to an infinitesimal small point,

Source	Method	Pattern	Detection	Geometry	Remarks
Yule-Nielsen 1951 [43]	projection	halogen filament	analogue photograph		microdensitometric measurements using a microscope
Yule-Nielsen 1951 [43]	contact	halftone pattern	area-integrated, densitometric	ND	different screen rulings
Yule et al. 1967 [47]	projection	knife edge on Kodak plate	modified microdensitometer	45°/0°	
Wakeshima and Kunishi 1968 [48]	projection	small point (pencil of light)	ND	ND	
Engeldrum and Pridham 1995 [49]	projection	knife edge photogr. film	microdensitometer	45°/0°	
Arney et al. 1996 [21]	contact	bar target film	CCD camera	45°/0°	
Inoue et al. 1997 [50]	projection	sinusodial	modified microdensitometer	45°/0°	halogen lamp
Rogers 1998 [51]	projection and contact	bar target	ND	d/ND	
Ackermann et al. 2002 [46]	projection	knife edge	CCD camera	0°/0°	
Arney et al. 2003 [17]	projection	half chromed glass plate	CCD camera	20°/0°	green filter, polarizing filter
Ukishima et al. 2009 [52]	projection	pencil light, iris of microscope	CCD camera	0°/0°	halogen lamp, daylight filters, bandpass filters, polarizing filters

Table 3.1: Overview of measurement setups in literature.

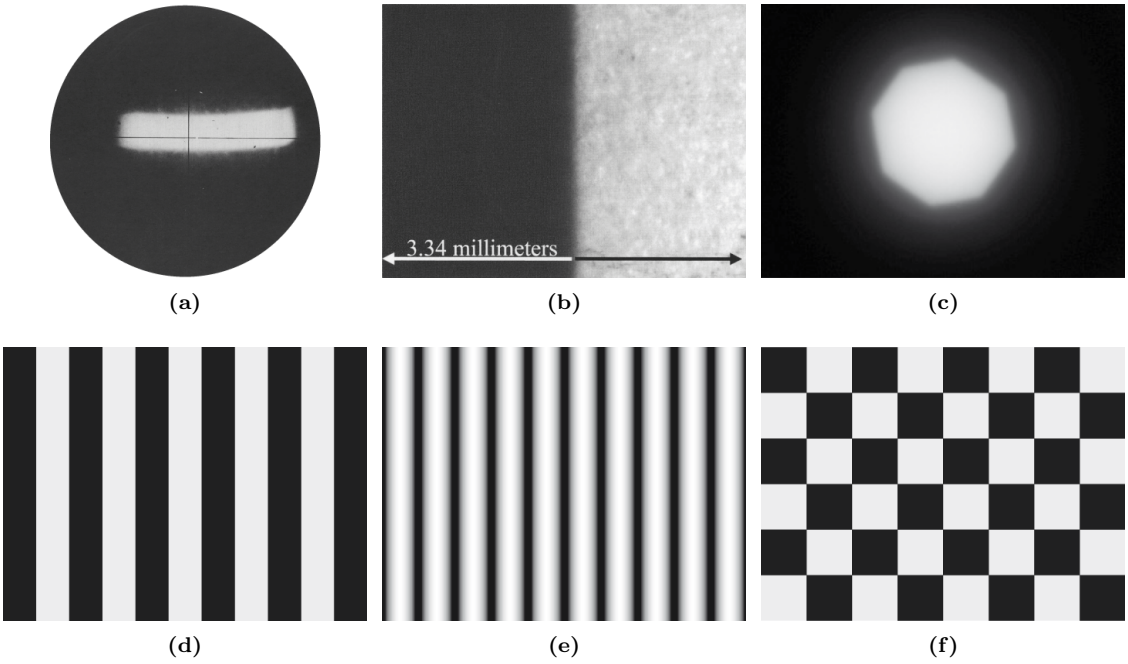

Figure 3.1: Different light patterns: a) halogen filament of Yule-Nielsen [43], b) edge of Arney et al. [17], c) pencil light of Ukishima et al. [52], d) bar pattern, e) sinusoidal pattern, and f) checkerboard pattern.

as it was done by Wakeshima and Kunishi [48]. Rogers [51] found out that for a special type of MTF calculation, a bar target performed best. This was an enhancement of the frequently used sinusoidal light pattern, as it can be found in Inoue et al. [50]. Ukishima et al. [52] used a pencil light (figure 3.1c) as it is created by closing the iris of a microscope. Also halftone pattern can be used, as shown by Yule and Nielsen [43], while they also mention a checkerboard pattern.

When using bar or sinusoidal pattern, it is common to use multiple test pattern with different frequencies, which allow for a direct determination of the MTF [53].

Projection and Contact Method

Most methods reviewed project the light pattern onto the sample, in the following this procedure will be called the *projection method* [51]. This method involves some difficulties in terms of the geometry of measurement (see "Geometry of Measurement", p. 34) and the focus calibration. However, there is an alternative method, where a film with a defined pattern is attached to the surface of the sample. The developed areas create dark regions, the transparent film allows the light to pass through almost without any change. This method will be called the *contact method* [51] in the following. Although this method seemingly allows for any geometry of measurement, there are some important differences to the projection method, as it can be seen in figure 3.2 for an exemplary edge shaped light pattern.

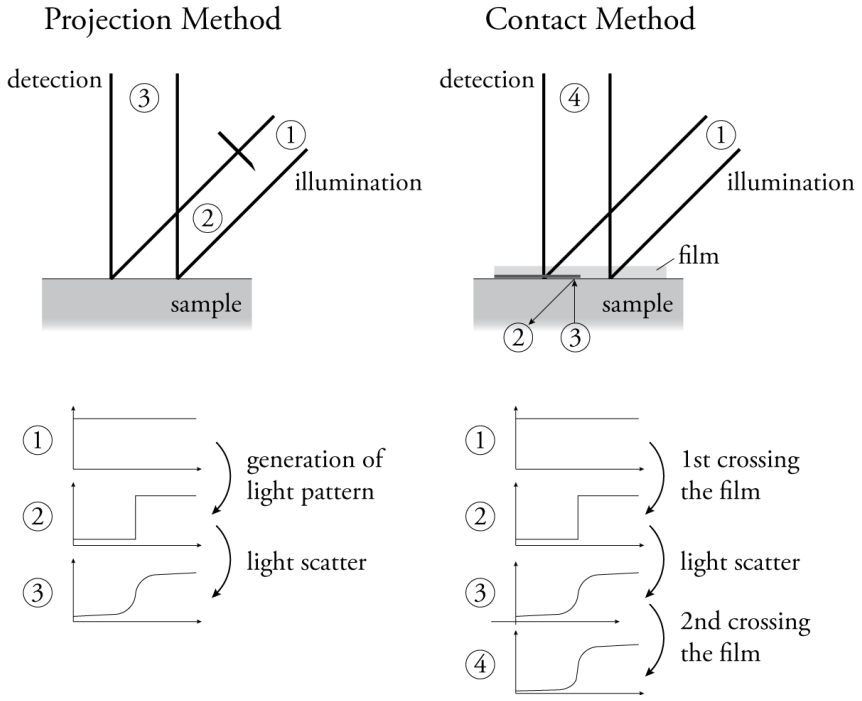

Figure 3.2: Projection method and contact method for the measurement of light scattering.

The first difference is that the light passes the pattern two times and not only one time in the illumination path. This way, the two methods result in different answers of reflectance for the same pattern. The results cannot be compared directly. This fact enables the contact method to be used for an area-integrated measurement, see "Detection of Reflectance" (p. 34). The second difference is that the design of the contact zone of film and sample is essential for the accuracy of the measurements. In some cases, optical contact can be created by using special liquids or glue. But with higher roughness of the surface of the sample this becomes increasingly difficult. Multiple reflections bias the results. The third difference arises from the fact that the height of the developed layer of the film can create shadows, depending on the illumination angle. This is even more relevant when using diffuse or divergent light as illumination. Providing collimated light is much more important for the contact method than it is for the projection method. Avoiding even more distortions in the measurement, the developed layer of the film should be oriented on the side next to the sample surface.

Generally, the transmission patterns used for the contact method can correspond to the light pattern for the projection method. For example, Arney et al. [21] and Rogers [51] both used bar targets, whereas Yule and Nielsen [43] attached strip films with halftone patterns in different screen rulings onto their samples.

Detection of Reflectance

The detection of the reflectance distribution is the detection of the answer of the sample according to the light pattern signal, with which it is illuminated. Therefore, the detection usually has to be laterally resolved e.g. by a regular grid as it is the case with most digital cameras, as they were used for most experimental setups [17, 21, 46, 52]. The first measurements of Yule and Nielsen [43] were captured by an analog camera. Traces of the images were measured with a microdensitometer. Other measurements with microdensitometers can be found at Engeldrum and Pridham [49] as well as Inoue et al. [50].

In contrast to the laterally resolved detection, the are-integrated measurement detects only one reflectance value that stands for the integrated answer of the sample. This can only work, if the total amount of light, that is detected, differs for a perfectly non-scattering and a scattering sample. This is only possible for the contact method. Assuming that the following model is valid: The number of "light beams" that enter the sample at transparent locations of the film and are scattered (transported) to a dark location is exactly the same as the number of "light beams" that enter the sample at a dark spot and are transported to transparent regions before exiting the sample. This way, every light-to-dark beam has its corresponding dark-to-light beam. For a perfectly scattering sample, these two beams each pass through a dark spot once and through a transparent spot the other time. In contrast, the sample with no scattering properties reflects the two beams exactly where they entered. The one beam passes two times through the transparent part, the other beam two times through the dark part of the film with transmittance $0 < T_d < 1$. Assuming that the transparent part of the film does not absorb any light at all ($T_t = 1$), the condition that the total amount of detected light for perfectly non-scattering and scattering sample differ can be written as:

$$2T_d \neq 1 + T_d^2. \tag{3.1}$$

This is true for all $T \neq 1$. Since, for the transmittance taking the value 1 there would be no difference between transparent and dark regions of the film, it can be stated that this condition is always satisfied.

An example for an area-integrated measurement can be found at Yule and Nielsen [43].

Geometry of Measurement

The angle of the incident light of the illumination and the angle of detection relative to the surface normal of the sample define the measurement geometry as defined in section 2.2. The measurement geometry for light scattering should correspond to the measurement geometry of the measurement instruments, where the results shall be applied. In the work at hand this is the measurement geometry of densitometers and the majority of spectrophotometers, which is $0^\circ/45^\circ$ or $45^\circ/0^\circ$ respectively.

For most setups in literature the angle of detection is 0°. However, the angle of illumination varies from 45° to 0°. For the contact method, the biggest influence can arise from the mentioned shadowing.

Using the projection method, a measuring geometry other than 0°/0° (in combination with no collimated light) always leads to regions that are out of focus. The sample and the image plane of the light pattern are tilted. Only the line of intersection of these two planes is in focus. The measurement has to be restricted to this small line. For the detection of the whole area, the height of the sample must be continuously adjusted.

Spectral Design

Emission spectrum of the light source and spectral sensitivity of the sensor are key elements for the spectral design of the measurement setup. Although there are several possible light sources, the measurement setups from literature usually use a halogen lamp [43, 50, 52]. In some cases, this broadband illumination is limited using color filters [17,52]. This way, a narrow-band or approximately monochrome measurement can be realized.

The color filters can be placed either directly behind the light source or in front of the detector. Similar effects can be achieved with both placements. Nevertheless, there might be differences due to fluorescent pigments in paper. When placing the filter in front of the sensor, these pigments can be stimulated by UV light coming from the light source. Although the relevant wavelengths might be absorbed by the color filter and are not detected this way, the emitted light from the fluorescent pigments could have a wavelength that can pass the color filter. Placing the color filter directly behind the light source, the stimulating wavelengths would be absorbed there and fluorescence would be omitted.

There are two general types of color filters. Absorption filters absorb the light while dichroic filters reflect it. This reflection could increase internal stray light. These effects due to the position of the color filters have not been investigated, yet.

Instead of using color filters, the spectral design can also be derived by choosing a matching light source, for example a narrow-band LED or a monochromator.

Polarization

For measurement geometries that detect close to the angle of mirror reflection, surface reflections can affect the measurement noticeably. Using polarizing filters suppresses the detection of these surface reflections. Only Ukishima et al. [52] mention the use of polarizing filters. The effect on the measurement with and without polarizing filters will be investigated in section 3.3.4.

3.1.2 Morphological Analysis

The review of literature lead to a morphological analysis of the different components and methods of the measurement setups. Table 3.2 presents the results of the morphological analysis, where the aspect of the measurement setup can be found in the first row, followed by possible solutions.

Apart from the presented solutions in the previous sections, a new solution for the aspect of the method for the pattern generation could be derived. It is usually solved using contact or projection method, as they are previously described. All setups in literature that are based on the projection method generate the pattern in transmittance. Either some partly transparent and partly opaque material is inserted into the light path, or the light path is partly blocked. A new solution for pattern generation is the projection method in reflectance mode [54]. This could be realized by micro-projection technology using a DMD (*digital micromirror devices*) or an LCOS (*liquid crystal on silicone*) device. A similar method is used for focusing in the profilometer Sensofar Plμ Neox [55].

3.1.3 Principle Design

For the following measurement setup, the projection method is chosen. It does not require collimated light which reduces the efforts for the measurement setup considerably. In order to avoid the focus problem with illumination apart from 0°, a 0°/0° measurement geometry is chosen, although it is not identical to the measurement geometries for color measurement or densitometry. The measurement setup will be incorporated into a standard microscope. Here, the 0°/0° measurement geometry is already available. The microscope also allows for attaching a camera for detection. A monochrome CCD camera will be used, avoiding any lateral loss of resolution due to the typical color filter patterns of RGB cameras. This way, the full sensor can be used to detect the laterally resolved image of the reflectance answer of the sample.

For the choice of the light pattern, some aspects have to be considered. The first is the fact, that the measurements are to serve for the calculation of a PSF. While periodic pattern are preferable for the detection of an OTF or an MTF, the PSF can be found easiest, if the light pattern resembles one of the spread function inputs, i.e. point-, line- or edge-shaped illumination. The second aspect is the feasibility for measurement. Here, point and line pattern have drawbacks, since the illuminated regions are so small. Therefore, the edge pattern is preferable for the measurement task [20], while LSF and PSF can be calculated from the measured ESF.

Other important parts of the measurement setup will not be fixed at this state. Furthermore, their impact on the measurement result will be examined. For the influence of illumination spectrum, polarizing filters, and out-of-focus measurements, see section 3.3.4.

Method for Pattern Generation	contact (transmittance)	projection (transmittance)	projection (reflectance)			
Pattern Type	halftone	checkerboard	edge	bars	sinusodial	others (e.g. halogen filament, pencil light, point, line)
Detection Method	laterally resolved	area-integrated				
Detection System	analog photography	digital photography	densitometer	colorimeter	spectrora-diometer	
Measurement Geometry	0°/0°	d/0°	45°/0°	0°/45°	others	
Spectral Sensitivity	broadband	narrowband	monochromatic			
Reduction of Sensitivity	none	inherent characteristics of light source	inherent characteristics of detection	filtering of light source	filtering of detector	others
Handling of Surface Reflections	none	polarizing filters	correction equations			

Table 3.2: Morphological analysis for generation of new solutions for the measurement of light scattering.

3.2 Image Acquisition and Data Processing

The measurement of light scattering with the principle design according to section 3.1.3 requires the detection of differences in the lateral reflectance distribution.

In the following sections, it will be derived what kind of images are necessary to perform such a measurement. The conditions for image capture will be deduced. Subsequently, the measured ESFs can be transformed into LSFs and PSFs. The relevant equations and transformation strategies will be presented.

3.2.1 Required Images

Let the sample be illuminated by a certain unknown distribution of irradiance E_s as a function of two variables x, y, indicating the location on the sample and the pixels of the camera respectively. All values also depend on the wavelength λ, although it will not be denoted in the following equations. Assuming that the physical effects at the bottom interface have only little influence on the reflectance, the sample can be modeled using only the top interface and the volume, as illustrated in figure 3.3. For the top interface, the following equations can be formulated:

$$M_s(x,y) = \rho \cdot E_s(x,y) + (1-\rho') \cdot I_0^-(x,y) \tag{3.2}$$

$$I_0^+(x,y) = (1-\rho) \cdot E_s(x,y) + \rho' \cdot I_0^-(x,y) \tag{3.3}$$

where ρ is the surface reflection from the surround and ρ' from the volume. The exitance from the sample is denoted by M_s. I_0^+, I_0^- are auxiliary values. The light balance equation for the volume is:

$$I_0^-(x,y) = (1-\alpha) \cdot \left(I_0^+ * \mathcal{P}_s\right)(x,y) \tag{3.4}$$

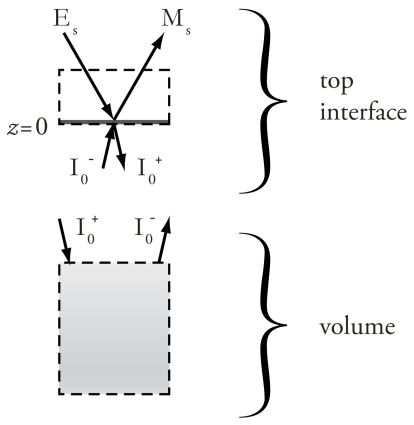

Figure 3.3: Simplified model of the sample with irradiance E_s, exitance M_s, and auxiliary values I_0^+, I_0^-.

where α is the absorption, $*$ the convolution operator (see appendix A.1), and $\mathcal{P}_s$ the point spread function representing light scattering in the medium, see section 2.1.2. Absorption can be neglected, if the spectrum of the light source covers a range, where the reflectance of the sample is high. Also, surface reflection can be reduced to a negligible amount when using polarizing filters. Then, equations 3.2 to 3.4 simplify to the single relation:

$$M_s(x, y) = (E_s * \mathcal{P}_s)(x, y). \tag{3.5}$$

In this work, this exitance is detected with a CCD camera. The output of the CCD camera is a distribution of gray values $\boldsymbol{V}(i, j)$, where i, j stand for the i'th row and the j'th column. The gray value depends on the charge Q that has been freed during exposure time t_E in one pixel. Thus, a gray values is the result of the irradiance $E_c(x, y)$ incident on the pixel with the size $w_x \cdot w_y$, integrated over exposure time t_E and pixel area:

$$\boldsymbol{V}(i, j) = k \cdot \int_0^{t_E} \int_{jw_y}^{(j+1)w_y} \int_{iw_x}^{(i+1)w_x} E_c(x, y)\, \mathrm{d}x\, \mathrm{d}y\, \mathrm{d}t. \tag{3.6}$$

where k is a characteristic value for the camera that depends on its quantum efficiency η predominantly. Linearity of the sensor provided and assuming that irradiance is constant during exposure time t_E and constant over one pixel, all pixels having the same size, the equation for the gray value simplifies to:

$$\boldsymbol{V}(i, j) \approx k \cdot t_E \cdot w_i \cdot w_j \cdot E_c(i, j) \tag{3.7}$$

Now, the irradiance on the camera E_c is a function of the exitance of the sample M_s. Between sample and camera, the light has to pass some lenses and windows, thus it encounters some transformations. Assuming that these transformations can be described by a simple convolution with a point spread function of the observation unit $\mathcal{P}_o$ leads to:

$$E_c(i, j) = (M_s * \mathcal{P}_o)(i, j). \tag{3.8}$$

Combining equations 3.5 to 3.8, the gray value can be written as:

$$\boldsymbol{V}(i, j) = k \cdot t_E \cdot w_i \cdot w_j \cdot (E_s * \mathcal{P}_s * \mathcal{P}_o)(i, j). \tag{3.9}$$

When generating the light pattern, the irradiance on the sample E_s is changed. The assumption is reasonable that the new edge-shaped irradiance $E_{s,\mathcal{M}}(i, j)$ is simply the product of the original irradiance $E_s(i, j)$ with a mask $\mathcal{M}(i, j)$, the latter generating the light pattern:

$$E_{s,\mathcal{M}}(i, j) = \mathcal{M}(i, j) \cdot E_s(i, j). \tag{3.10}$$

Generally, the mask does not need to be of a specific shape. Bar pattern, sinusoidal pattern, an edge or other shapes can be realized. With this masked illumination, the detected gray values can be gained according to equation 3.9:

$$\boldsymbol{V}_{\mathcal{M}}(i,j) = k \cdot t_E \cdot w_i \cdot w_j \cdot ((\mathcal{M} \cdot E_s) * \mathcal{P}_s * \mathcal{P}_o)\,(i,j). \tag{3.11}$$

Let the irradiance on the sample E_s be approximately constant over i, j. Then two simplifications can be made:

$$(E_s * \mathcal{P}_s)\,(i,j) \approx E_s(i,j) \tag{3.12}$$

$$((\mathcal{M} \cdot E_s) * \mathcal{P}_s)\,(i,j) \approx E_s(i,j) \cdot (\mathcal{M} * \mathcal{P}_s)\,(i,j). \tag{3.13}$$

This way, equations 3.9 and 3.11 can be written as:

$$\boldsymbol{V}(i,j) = k \cdot t_E \cdot w_i \cdot w_j \cdot E_s(i,j) \tag{3.14}$$

$$\boldsymbol{V}_{\mathcal{M}}(i,j) = k \cdot t_E \cdot w_i \cdot w_j \cdot E_s(i,j) \cdot (\mathcal{M} * \mathcal{P}_s * \mathcal{P}_o)\,(i,j). \tag{3.15}$$

The ratio of the detected gray values $\boldsymbol{V}$ of the sample that is evenly illuminated and the gray values $\boldsymbol{V}_{\mathcal{M}}$ for the masked illumination can be reduced to

$$\frac{\boldsymbol{V}_{\mathcal{M}}(i,j)}{\boldsymbol{V}(i,j)} = \left(\frac{\boldsymbol{V}_{\mathcal{M}}}{\boldsymbol{V}}\right)(i,j) = (\mathcal{M} * \mathcal{P}_s * \mathcal{P}_o)\,(i,j) \tag{3.16}$$

in case of identical exposure times t_E for both acquisitions. Still, the mask $\mathcal{M}$ and the point spread function of the observation unit $\mathcal{P}_o$ are unaccessible. Therefore, an acquisition of a reference material can be used to eliminate these unknowns. This material is assumed to have perfect surface reflection, no absorption and no light scattering in the medium. Then the discrete form of equation 3.5 becomes:

$$M_{s,\mathrm{ref}}(i,j) = E_{s,\mathrm{ref}}(i,j). \tag{3.17}$$

Thus, the reference would create the following ratio of gray values:

$$\left(\frac{\boldsymbol{V}_{\mathcal{M},\mathrm{ref}}}{\boldsymbol{V}_{\mathrm{ref}}}\right)(i,j) = (\mathcal{M} * \mathcal{P}_o)\,(i,j). \tag{3.18}$$

The same result could be derived by assuming a perfect Dirac impulse as $\mathcal{P}_{\mathrm{ref}}$ and substitute it as $\mathcal{P}_s$ in equation 3.16. Substituting equation 3.18 into equation 3.16 leads to

$$\boxed{\left(\frac{\boldsymbol{V}_{\mathcal{M}}}{\boldsymbol{V}}\right)(i,j) = \left(\mathcal{P}_s * \left(\frac{\boldsymbol{V}_{\mathcal{M},\mathrm{ref}}}{\boldsymbol{V}_{\mathrm{ref}}}\right)\right)(i,j),} \tag{3.19}$$

which will be called the *2D measurement equation* in the following. From this equation, the PSF $\mathcal{P}_s$ can be obtained by deconvolution. For the measurement of the PSF the following four images have to be acquired:

- reference, unmasked illumination ($\boldsymbol{V}_{\mathrm{ref}}$)
- reference, masked illumination ($\boldsymbol{V}_{\mathcal{M},\mathrm{ref}}$)
- sample, unmasked illumination ($\boldsymbol{V}$)
- sample, masked illumination ($\boldsymbol{V}_{\mathcal{M}}$)

Some restrictions have to be considered, when capturing the images for measurement. First, the acquisition of the images with masked and unmasked illumination should be performed using the same exposure time. This is valid for sample and reference respectively. Second, the images of the reference (masked and unmasked) must be taken without polarizing filters, since the reference is assumed to have perfect surface reflection and polarizing filters would eliminate the captured reflectance. The sample images require the use of polarizing filters. Thirdly, samples with high absorption in the wavelength range of the irradiance produce almost no signal and cannot be measured. Fluorescent components in the sample can alter the results. For good results, absorption and fluorescence should be negligible.

3.2.2 Measurement With Edge-Shaped Illumination

The direct extraction of the PSF $\mathcal{P}_s$ from equation 3.19 has an important drawback when there is noise in the measurement system. One action to reduce noise is to take the average over a series of shots for each of the four required images. This can reduce temporal noise of the camera or due to a flickering light source. An additional action is to restrict the mask $\mathcal{M}$ to be invariant in one direction, for example in being edge-shaped. Let the mask be constant in j-direction:

$$\mathcal{M} = \mathcal{M}(i). \tag{3.20}$$

Averaging all pixels in j-direction with n being the number of elements, equation 3.16 results in

$$\frac{1}{n}\sum_{j=1}^{n}\left(\frac{\boldsymbol{V}_{\mathcal{M}}}{\boldsymbol{V}}\right)(i,j) = \frac{1}{n}\sum_{j=1}^{n}\left(\mathcal{M} * \mathcal{P}_s * \mathcal{P}_o\right)(i,j), \tag{3.21}$$

which can be written as:

$$\frac{1}{n}\sum_{j=1}^{n}\left(\frac{\boldsymbol{V}_{\mathcal{M}}}{\boldsymbol{V}}\right)(i,j) = k \cdot \left(\mathcal{M} * \left(\sum_{j=1}^{n}\mathcal{P}_s\right) * \left(\sum_{j=1}^{n}\mathcal{P}_o\right)\right)(i), \tag{3.22}$$

where is k a constant factor. With the definition of a *line spread function* (LSF) $\mathcal{L}$

$$\mathcal{L}(i) = \sum_{j}\mathcal{P}(i,j), \tag{3.23}$$

equation 3.22 becomes

$$\frac{1}{n}\sum_{j=1}^{n}\left(\frac{\boldsymbol{V}_{\mathcal{M}}}{\boldsymbol{V}}\right)(i,j) = k\cdot(\mathcal{M} * \mathcal{L}_s * \mathcal{L}_{o,j})(i). \tag{3.24}$$

Introducing the abbreviations for the mean relative gray values

$$\boldsymbol{I}(i) = \frac{1}{n}\sum_{j=1}^{n}\left(\frac{\boldsymbol{V}_{\mathcal{M}}}{\boldsymbol{V}}\right)(i,j) \tag{3.25}$$

$$\boldsymbol{I}_{\mathrm{ref}}(i) = \frac{1}{n}\sum_{j=1}^{n}\left(\frac{\boldsymbol{V}_{\mathcal{M},\mathrm{ref}}}{\boldsymbol{V}_{\mathrm{ref}}}\right)(i,j), \tag{3.26}$$

the 2D measurement equation 3.19 becomes a *1D measurement equation*:

$$\boxed{\boldsymbol{I}(i) = (\mathcal{L}_s * \boldsymbol{I}_{\mathrm{ref}})(i).} \tag{3.27}$$

This leads to some additional restrictions for the measurement. The reduction of temporal noise in the measurement system requires the repetition of one capture for several times. The averaging of pixels along one direction is only valid, if the edge is aligned to this pixel direction. A good adjustment is a prerequisite.

3.2.3 LSF and PSF Acquisition

When calculating the LSF from equation 3.27, different methods can be utilized. One example is the deconvolution using predefined algorithms provided by MATLAB. Such algorithms are deconvolution using long division for 1D deconvolution and blind deconvolution, Lucy-Richardson deconvolution, deconvolution using regularized filter, and deconvolution using Wiener filter for 2D deconvolution [56].

Alternatively, the LSF can be derived by dividing the Fourier transforms of the captured images:

$$\mathcal{L}_s(x) = \mathcal{F}^{-1}\left[\frac{\mathcal{F}[\boldsymbol{I}(i)]}{\mathcal{F}[\boldsymbol{I}_{\mathrm{ref}}(i)]}\right]. \tag{3.28}$$

where $\mathcal{F}$ is the Fourier transform and $\mathcal{F}^{-1}$ its inverse. It was found that both methods, direct deconvolution and Fourier transform, perform poorly on noisy ESFs.

Aiming to find a robust method for noisy ESFs, an approach is to use simple empirical functions with only one parameter s as starting point for the LSF $\mathcal{L}(s,i)$. The best guess for one function can be achieved by solving the optimization problem

$$\underset{s>0}{\text{minimize}} \sum_{i} \left[\boldsymbol{I}(i) - (\mathcal{L}(s) * \boldsymbol{I}_{\mathrm{ref}})(i)\right]^2 \tag{3.29}$$

where $\mathcal{L} * \boldsymbol{I}_{\text{ref}}$ is the simulated edge and $\boldsymbol{I}$ is the captured edge.

This approach produces very smooth LSFs but sometimes the residuals are quite large and, according to this, the chosen function is not a good approximation for the LSF. Some empirical functions for the PSF can be found in literature [6,57,58]. From these, the corresponding LSFs can be calculated according to equation 2.20 or in a discrete way according to equation 3.23. Appendix A.3 sums up some PSFs and their LSFs.

When fitting these empirical functions, the resulting form parameter s can be substituted into the PSF equation without any further processing.

Fitting empirical functions is very stiff and unflexible. A solution for the given deconvolution problem can be found with linear programming [59]. This approach allows a maximum degree of freedom for the LSF that is not bound to any empirical functions. At the same time the solution is less affected by noise than direct deconvolution or Fourier transform. Unfortunately, the high degree of freedom is the reason why a lot of LSFs produce results that are equivalent in their residuals but differ significantly in their shape. Thus, the solution space has to be restricted with physically feasible constraints. Finding a solution for the LSF, the following minimization problem is formulated:

$$\underset{\mathcal{L}}{\text{minimize}} \sum_i \left| \boldsymbol{I}(i) - \left(\mathcal{L} * \boldsymbol{I}_{\text{ref}}\right)(i) \right| \tag{3.30}$$

where $\mathcal{L} * \boldsymbol{I}_{\text{ref}}$ is the simulated edge and $\boldsymbol{I}$ is the captured edge. For practical reasons, the LSF has an uneven dimension N. This way, there is always a center element i_0 of the LSF that stands for the location of the infinitesimal line.

For linear programming, the convolution of the LSF $\mathcal{L}$ with the reference image $\boldsymbol{I}_{\text{ref}}$ can be formulated as multiplication with a convolution matrix of the reference image $\boldsymbol{C}$. This way, the minimization problem of equation 3.30 can be substituted by:

$$|\boldsymbol{I} - \boldsymbol{C}\mathcal{L}| \leq \epsilon, \tag{3.31}$$

where ϵ is an auxiliary variable representing the difference between captured and simulated edge. which leads to the following two constraints for linear programming:

$$\begin{aligned} -\boldsymbol{C}\mathcal{L} - \epsilon &\leq -\boldsymbol{I} \\ \boldsymbol{C}\mathcal{L} - \epsilon &\leq \boldsymbol{I}. \end{aligned} \tag{3.32}$$

The LSF must be positive. This leads to the condition:

$$\mathcal{L}(i) \geq 0. \tag{3.33}$$

Two other constraints for the LSF are that its maximum is centered, i.e. the location i_0 of the imaginary infinitesimal illuminated line, and that it is reflectional symmetric with respect to i_0.

$$\mathcal{L}(i_0 - i) = \mathcal{L}(i_0 + i) \tag{3.34}$$

These center and symmetry constraints are reasonable, but they could be also defined differently. However, the symmetry of the LSF is mandatory.

It is comprehensible that the LSF decreases with increasing distance from its center. The LSF must be unimodal, i.e. it is monotonically increasing for $i < i_0$ and monotonically decreasing for $i > i_0$. The maximum value is $\mathcal{L}(i_0)$ and there are no other local maxima.

$$\mathcal{L}(i+1) - \mathcal{L}(i) \begin{cases} \geq 0 & \text{for } i \leq i_0 \\ \leq 0 & \text{for } i \geq i_0 \end{cases} \tag{3.35}$$

In addition, a reasonable consideration is that also the PSF must be monotonically decreasing for increasing radius. This leads to the constraint, that the second derivative of the LSF must be greater than or equal to zero for $i < i_0$, and less than or equal to zero for $i > i_0$. This can be written as the following smoothness constraint:

$$\mathcal{L}(i+1) - 2\mathcal{L}(i) + \mathcal{L}(i-1) \begin{cases} \geq 0 & \text{for } i \leq i_0 \\ \leq 0 & \text{for } i \geq i_0. \end{cases} \tag{3.36}$$

Since light scattering is assumed to be restricted to light transport and not to be responsible to any loss of light here, the law of energy conservation must be satisfied. This means that the overall amount of light that is distributed by the LSF must be equal to the amount of light that is incident. The sum of all LSF elements must be one.

$$\sum_i \mathcal{L}(i) = 1 \tag{3.37}$$

Since usually the resulting LSFs from linear programming cannot be described by analytical functions, the PSF must be acquired using the transformation equation 2.21.

Both approaches, linear programming and fitting empirical functions, are based on isotropic light scattering. The acquisition of anisotropic PSFs needs some further investigations and is not part of this research.

3.3 Experimental Setup

The general measurement design, as derived in chapter 3.1, was realized by enhancing an existing microscope. The performed changes, new constructions and a detailed characterization of the parts of the measurement setup can be found in the following section 3.3.1. For a reliable measurement, a set of adjustments and calibrations is necessary. These will be described in section 3.3.2. Special attention is payed to the focus adjustment and the focussing of the sample, which can be found in section 3.3.3. Important influences on the reliability and the performance of the measurements will be analyzed in section 3.3.4.

3.3.1 The Setup in Detail

The experimental setup is an enhancement of the setups presented in the work of Walter [60] and in [1]. It is incorporated into a standard microscope (Leitz Orthoplan [61] with objective turret Ploemopak [62]) using the lens PL Apo 6.3 and consists of an illumination unit, a sample holding unit and an observation unit, as shown in figure 3.4.

Illumination Unit

Essential component of the illumination unit is the light source. The spectrum of the light illuminating the sample has a big influence on the measurement performance. The broader the illuminating spectrum, the more exact focusing of the system becomes difficult due to increasing chromatic aberration. Thus,

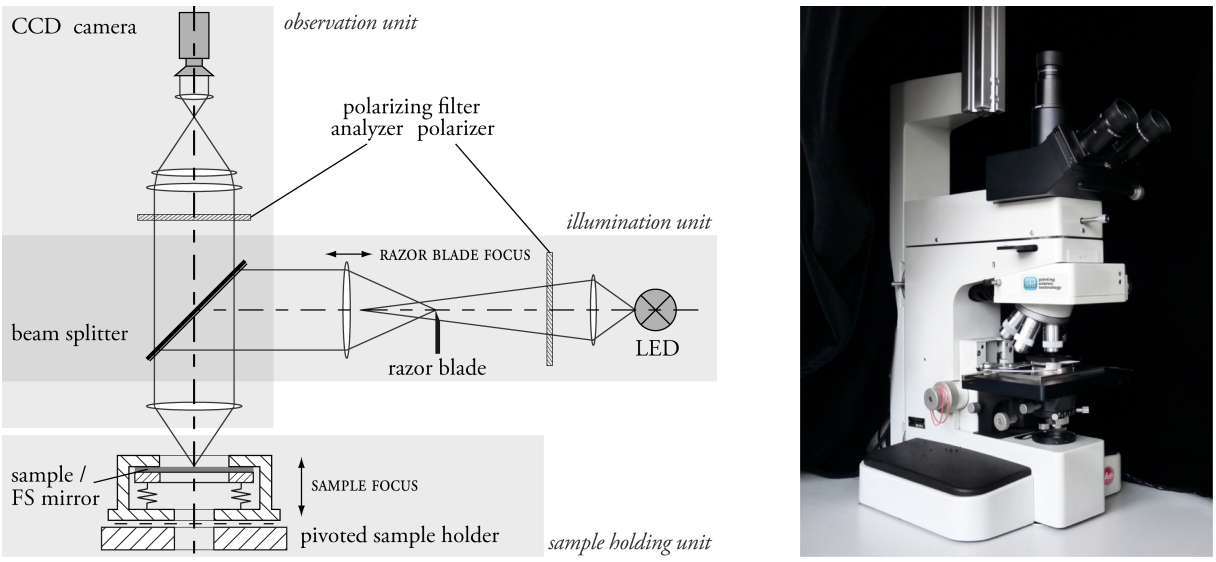

Figure 3.4: Schematic and picture of the experimental setup for the measurement of light scattering in paper.

the limitation of the spectrum should be considered. Either, a small-band or even monochromatic light source could be chosen or the spectrum should be limited using small-band filters. For this work, a green *light-emitting diode* (LED) was installed. It allows for a small-band measurement, where the maximum wavelength is close to the maximum of the luminous efficiency function. Small-band filters are not needed in this case. A monochromator would be even more advantageous in terms of spectral resolution and focus but due to the higher costs and the less luminous exitance, the LED seems to be preferable.

The LED is attached to a passive heat sink (figure 3.5). Its spectral power distribution is sufficiently constant over time. In figure 3.6 the spectrum of the LED was measured over 30 minutes with a spectro-radiometer (Konica Minolta CS-1000A), not revealing a significant change. The position of the LED can be adjusted in three directions. An additional lens allows for adjusting the magnitude of the illumination relative to the image size. For performance analysis, the green LED can be replaced by a blue or red LED or the original halogen lamp respectively.

Another important part of the illumination unit is the creation of the light pattern. In the experimental setup the half-plane pattern is realized using the edge of a razor blade. For good quality measurements, three conditions have to be satisfied. First, the geometry of the edge of the razor blade has to be free of defects and as straight as possible, and second, the focus calibration has to be as good as possible, see section 3.3.2. Thirdly, the edge should be in the center of the field of detection. A new mechanism allows to swivel the razor blade into the light path, while the edge direction stays constant, as it can be seen in figure 3.7. This allows for an advanced and reproducible edge positioning and easy edge removal for detecting the lateral distribution of the illumination level. The focus of the blade can be adjusted by moving a lens.

The image of the edge will always be influenced by Fresnel diffraction at the razor blade and distortions inside the microscopes windows and lenses. An important aim is to remove as much distortions as possible and to be aware of the distortions that cannot be avoided.

Observation Unit

The observation unit holds a 2 megapixel (MP) monochrome *charge-coupled device* (CCD) camera (Basler scA1600-14gm) with 12 bit signal depth. The pixel pitch is 4.4 µm. The advantage of a monochrome camera is the missing pattern with red, green, blue (RGB) filters. Thus, each pixel can be used for image evaluation. The pixel pitch of 4.4 µm is a good compromise of small pixels for high resolution and big pixels for a small signal-to-noise ratio.

Some materials produce high dynamic range measurements, where the difference between the reflectance of light and dark pattern elements is high. Nevertheless, it is necessary to detect even small differences in reflectance also for these images. Therefore, a good signal depth, 12 bit in this case, is necessary. Additionally, it is important to adjust the exposure time, so that the range of gray values

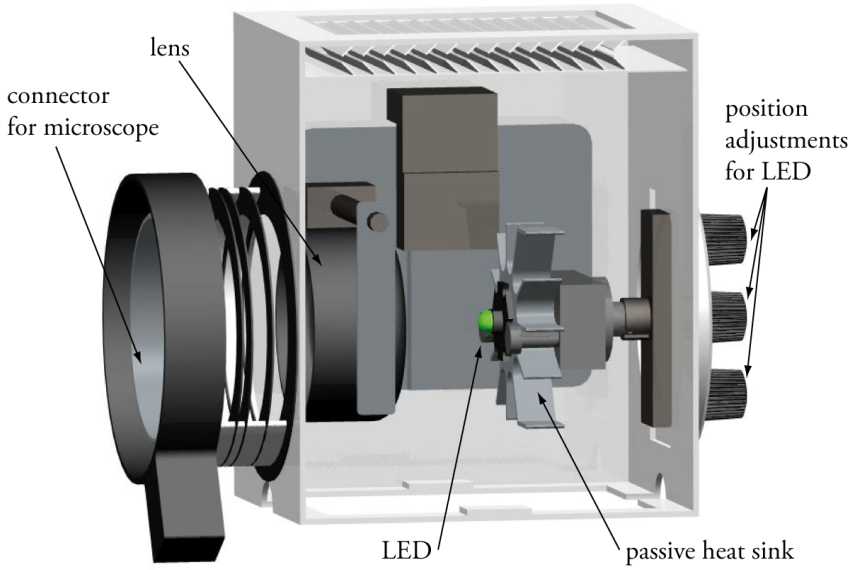

Figure 3.5: CAD image of the lamphouse with LED attached to passive heat sink and its position adjustments.

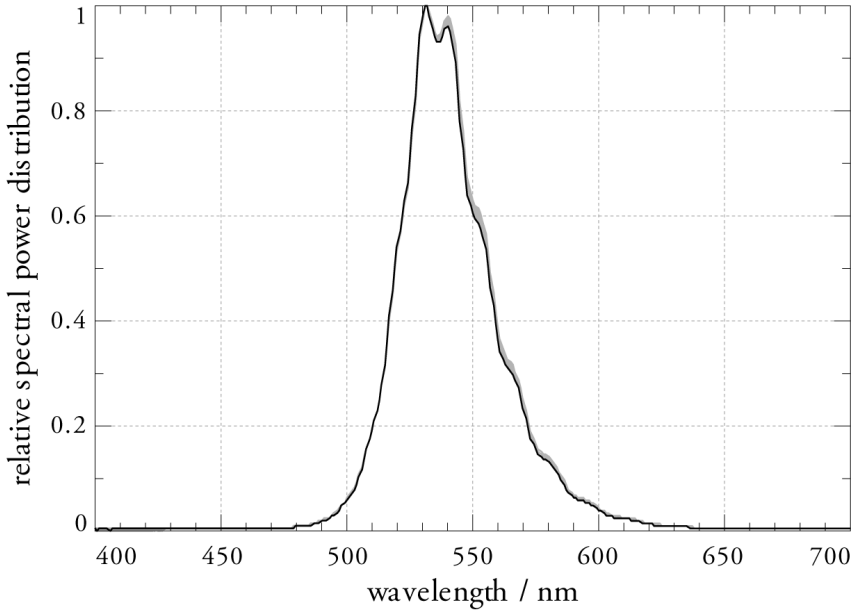

Figure 3.6: Relative spectral power distribution of green LED: measurements over 30 minutes (gray) in comparison to first measurement (black).

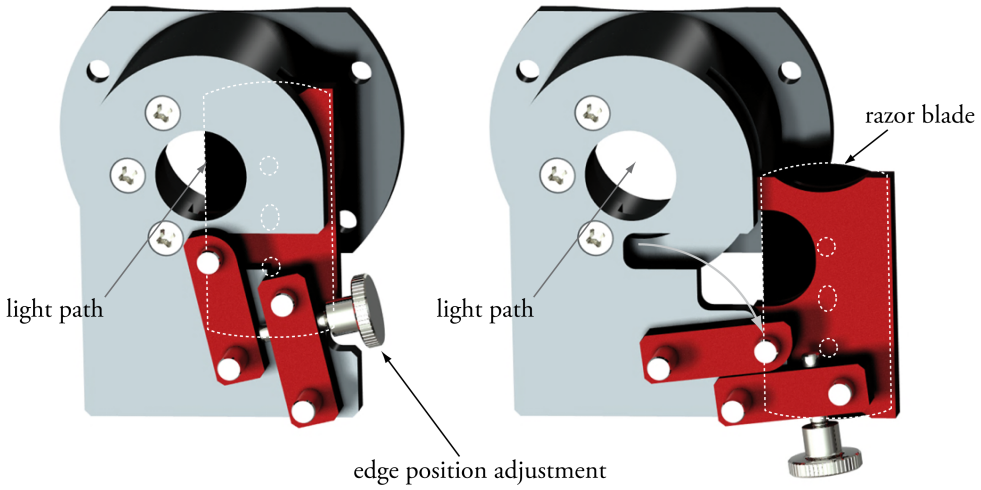

Figure 3.7: CAD image of the mechanism to swivel the razor blade in the light path (left) and out (right); The position of the razor blade in the light path can be adjusted while edge direction stays constant.

covers the whole signal range. For identifying the correct exposure time, the gray values are scaled so that the median of the lightest 40 % of the image is at about 94 % ± 2 % gray value. This algorithm is efficient and suitable for our measurements. It allows to capture differences in reflectance in the very light regions and at the same time offers the biggest quantization for the darkest regions of the image. This way, increasing the dynamic range of the camera by taking shots with different exposure times is not necessary. Working in the linear domain of the sensor, the gray values can directly be related to reflectances.

For image acquisition, the manufacturers *software development kit* (SDK) was connected to MATLAB, so that images could be directly accessed and processed there.

The combination of all optical parts in the observation unit will be called the imaging system in the following. It will be treated as one unit. The following elements belong to the imaging system:

- CCD camera,
- beam splitter,
- objective lens, and
- other windows of objective turret and microscope that lie in the observation path.

Sample Holding Unit

The sample holding unit consists of a special sample holder that is attached to the microscope stage. This allows for a simple adjustment of the sample focus by moving the microscope stage in vertical direction.

The sample holder used here was developed in a supporting work of Walter [60]. It takes over an important task that has been the source of imprecisions in the past: the adjustment of the sample focus.

Figure 3.8: Image of the sample holder with paper sample. Scales on sample holder and microscope stage allow for reproducible angle adjustment [60].

Usually the samples (i.e. paper) have quite rough surfaces. That means that the highest image sharpness does not considerably vary over a certain range. This effect is even magnified when using broadband illumination. The result is that the adjustment of the sample focus is not reproducible. In order to enhance the sample focus, an aluminized *first* or *front surface mirror* (FS mirror) was introduced. The surface of the FS mirror has to be leveled with the surface of the sample. For this reason, FS mirror and sample are pressed against a superfinished steel plate which is positioned parallel to the microscope stage. This way, it is possible to switch between FS mirror and sample by simply sliding the microscope stage in horizontal direction – without leaving the focus.

The sample holder can be rotated about the optical axis of the microscope, again, without leaving focus. This way, inhomogeneous scattering properties can be detected. Scales on the microscope stage and on the sample focus allow for a reproducible angular positioning, see figure 3.8.

Other Components

Two other components of the measurement setup have big influence on the precision of the measurements. First, polarizing filters are used. The chosen measuring geometry $0°/0°$ involves that a lot of reflections from the surface of the sample are detected in the camera. This is not desirable for the measurement of light scattering. Especially rough surfaces distort the measurement, since their reflection at the surface is diffuse and in most cases not predictable. The use of polarizing filters can reduce this effect to a minimum. For this, a polarizer, positioned in the illumination unit, generates linearly polarized light. The light that is reflected directly at the sample surface does not change its polarization, other than the light that enters the material and is scattered. The analyzer, a second polarizing filter with orthogonal orientation to the polarizer, is located in the observation unit. The light that was reflected at the surface

cannot pass whereas the part of the light that changed polarization in the material can be detected. This way, disturbing surface reflections can be almost eliminated.

In contrast to samples with scattering properties, the part of the light that enters the FS mirror and changes its polarization is almost negligibly small. This way, the use of polarizing filters almost obliterates the image. Therefore, taking images of the reference, polarizing filters cannot be used.

A second important improvement to similar measurement setups is the prevention of stray-light distort the image detection. For this, a black curtain surrounds the whole microscope. It would also be possible, to locate the measurement setup in a dark room but working conditions in such a surround are not very agreeable. In addition, any light coming from the necessary computer monitor could influence the measurement. The curtain can be lifted to change samples or rotate the sample holder for the next angular measurement.

3.3.2 Adjustments and Calibration

Before being able to perform reliable measurements with the setup presented above, the setup has to be adjusted and calibrated. The actions include light adjustment, edge position adjustment, and calibration of pixel scale. For reliable adjustments, a reference material is required that reflects all light as correctly as possible. The FS mirror is an appropriate tool for these adjustments. Its surface is very even and its reflection is more than 95 % over the wavelength range of 450 nm to 650 nm, which is the most powerful part of the LED spectrum, see figure 3.9.

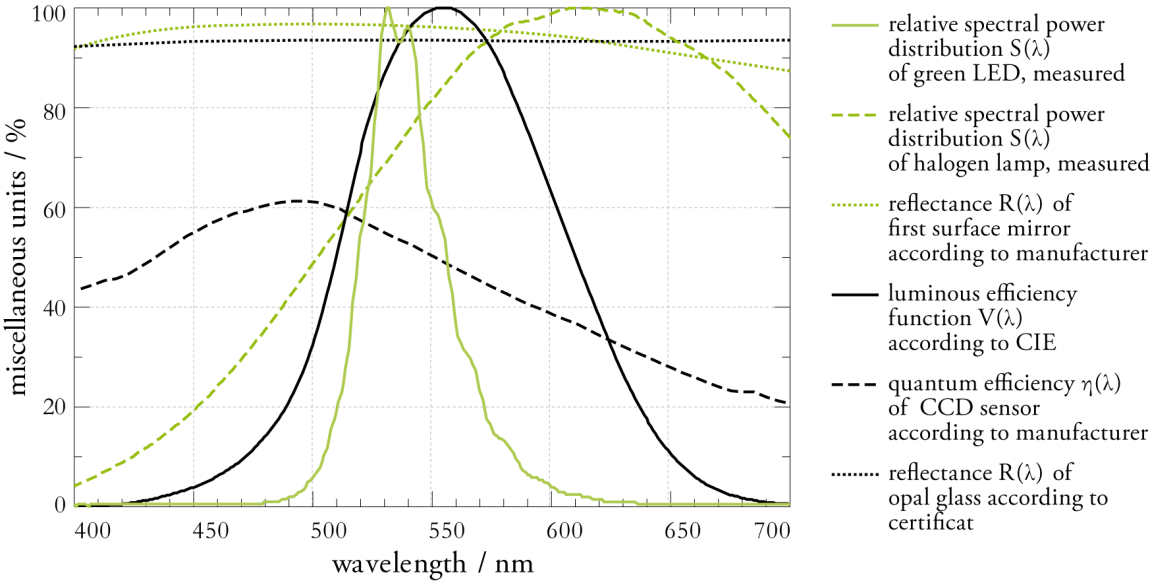

Figure 3.9: Different important spectra of the measurement setup.

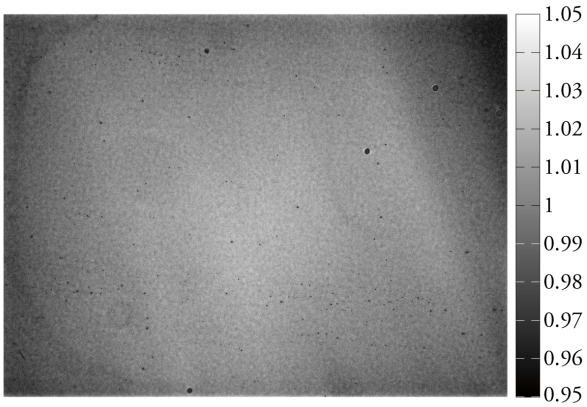

Figure 3.10: Spatial power distribution of LED light source relative to its average; reflectance from FS mirror captured with CCD camera.

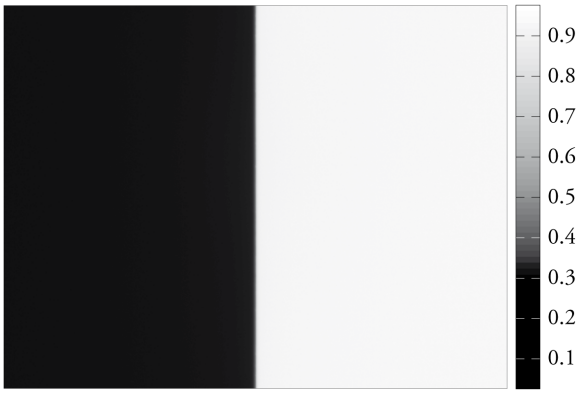

Figure 3.11: Position of the edge relative to the pixel rows of the CCD camera; green LED, relative reflectance from FS mirror.

All adjustments will be performed using the CCD camera as detection and MATLAB for evaluation. A collection of important spectra is shown in figure 3.9. The measurements of the light sources were performed with installed light sources and a spectroradiometer at the place of the CCD camera. The spectra were detected using the spectroradiometer KonicaMinolta CS-1000A with spectral range 360 nm to 780 nm and 1 nm resolution. All other data in figure 3.9 was derived from data sheets of the manufacturers [63–65], a certificate for the opal glass specimen [66] and CIE standard [36].

Light Source Adjustment

The light source of the measurement setup does not evenly illuminate the whole field of detection. This means, that some parts are darker than others just because of the non-uniform illumination and not because of light scattering or because of the edge in the light path. It is hard to eliminate this nonuniformity and a lot of efforts have to be done in order to reduce the deviations from uniformity to a negligible amount, see [67]. Nevertheless, light source adjustment can highly improve measurement performance, although uniformity cannot be achieved. For this, several position adjustments of the LED (see figure 3.5) and the lens permit to find the best setting.

For the adjustment of the light source, the edge is removed from the light path and the camera detects an image of the illumination over the total field of detection, reflected by the FS mirror. An exemplary image of the light's relative spatial power distribution is shown in figure 3.10. Dirt in the optical system makes it difficult to find an absolute value for the uniformity of the light's lateral power distribution, especially since the resolution of the image is quite high. Therefore, the 95 %-limit of the relative gray values is a good measure. For the lateral distribution in figure 3.10 the 95 %-limit was calculated approximately $\pm 2.6\,\%$.

Edge Position Adjustment

The adjustment of the edge to the pixel rows of the camera affects the complexity and the accuracy of the measurements. A good adjustment in row direction can eliminate the need for additional image processing, which always means data manipulation and possible distortion. For this, the edge holder can be rotated around the axis of the light path of the illumination unit. This allows for simple angular position adjustment of the razor blade edge relative to pixel orientation. With this tool, the deviation from being parallel in figure 3.11 is less than 2 px over 1236 pixel rows. This is an angular displacement of $0.093^\circ = 5.60'$.

A second edge position parameter is centering the edge relative to the field of detection. This way, the field of detection is proportionally divided into light and dark. With a screw, the centering of the edge can be adjusted without changing the angular orientation of the edge. The screw moves the razor blade in such a way that the edge stays parallel to the original orientation. In figure 3.11, the orthogonal displacement of the edge relative to the center of the field of detection is about 16 px out of 1626 pixel rows that is approximately 1 %.

Calibration of Pixel Scale

The physical pixel pitch of the CCD sensor is 4.4 µm according to the manufacturer [63]. For making the measurement results comparable to results gained with different measurement setups, the pixel pitch of the sensor has to be calibrated.

A typical microscope calibration relates the ocular scale to the metric scale of a stage micrometer. The result is a conversion factor f_c for the calculation of the real distances on the stage out of the distances read from the ocular scale [68]. In terms of camera measurements, the smallest unit is one pixel (px). Therefore, the conversion factor relates the distance of 1 px to the real distance on the microscope stage.

Determining the conversion factor, an image of a stage micrometer made of CERAN was captured, shown in figure 3.12. The scale was oriented parallel to the pixel rows of the CCD camera for an easy calculation of the conversion factor. In this case, the x-value of the first line and the x-value of the last line define the pixel difference ΔP, here this was 1605 px. The metric distance on the stage can be derived from the manufacturer's data [69]. In this case, the smallest division is 0.01 mm that means a distance of $d = 0.87\,\text{mm}$ between first and last line of the image in figure 3.12. Thus, the conversion factor f_c can be calculated as follows:

$$f_c = \frac{d}{\Delta P} = \frac{0.87\,\text{mm}}{1605\ \text{px}} = 0.542\,\mu\text{m/px}. \tag{3.38}$$

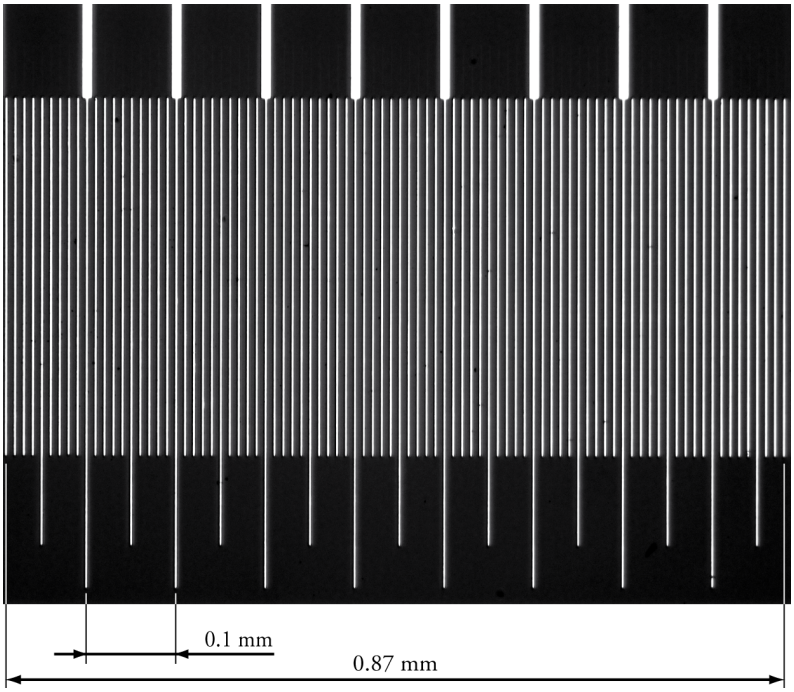

Figure 3.12: Image of CERAN stage micrometer with smallest units of 0.01 mm.

The conversion factor is only valid for the image plane of the observation unit. The distances from measurements that are out of focus are automatically not correct. Additionally, the minimal distance $d_{\min}$ of image elements that can be distinguished is limited by the wavelength λ of the illumination and the numerical aperture NA of the optics. According to Abbé's equation [10, 70], the minimal distance that can be detected is:

$$d_{min} = \frac{\lambda}{NA}. \tag{3.39}$$

According to the data sheet, the lens PL Apo 6.3 has a numerical aperture of 0.20. With a medium wavelength of the green LED of $\lambda = 535\,\text{nm}$, the minimal distance of resolvable objects is approximately 2.7 µm that equals about 5 px. This means that every image of the camera will be blurred, even if the focus adjustment is perfect. Better results can only be achieved with shorter wavelengths of the light source. An exemplary PSF of the imaging system can be seen in figure 3.13. This PSF was simulated with PSFLab [71] assuming a glass sample and monochromatic light of 535 nm.

This PSF is part of the blurring function $\mathcal{P}_o$ of the imaging system, as it is introduced in equation 3.8. With processing of the captured images as presented in section 3.2, it can be eliminated from the measured ESF.

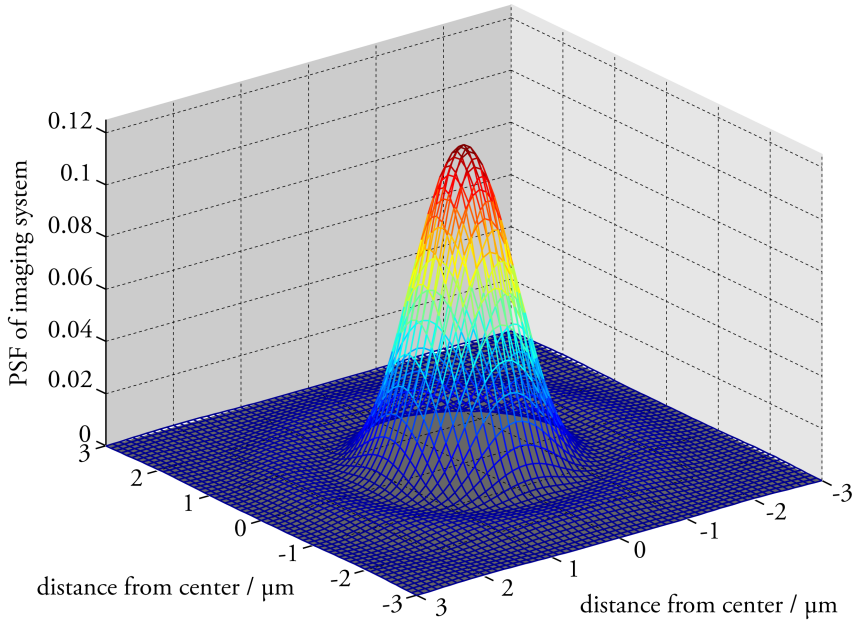

Figure 3.13: Simulation of the PSF of the imaging system for monochromatic light with $\lambda = 535\,\text{nm}$.

3.3.3 Focus Adjustment and Focusing

In terms of focus there are two actions that have to be distinguished. First, the *focusing* means to bring a sample into the image plane by moving it normally to this plane. Second, the *focus adjustment* relates to altering the position of the image plane by moving a lens along the light path.

The measurement setup has three foci:

- the focus of the edge,
- the focus of the light source, and
- the focus of the imaging system.

The focus of the edge is the only focus that can be adjusted independently. The focus of the light source is of secondary importance. It can be adjusted by a lens in the lamp house but is also influenced by the lens for the edge focus. The focus of the imaging system is static, it cannot be adjusted.

Focus adjustment and focusing of the sample are two of the most influencing factors concerning measurement accuracy. In the following, the term *focus adjustment* will be used for adjusting the edge focus so that its image plane and the image plane of the imaging system are identical. In contrast to the focus adjustment, the *focusing* of the sample refers to moving the sample into the image plane of the adjusted foci.

The first step is the focus adjustment as illustrated in figure 3.14. Since the focus of the imaging system cannot be modified, its image plane has to be identified by focusing a sample. Therefore, the FS

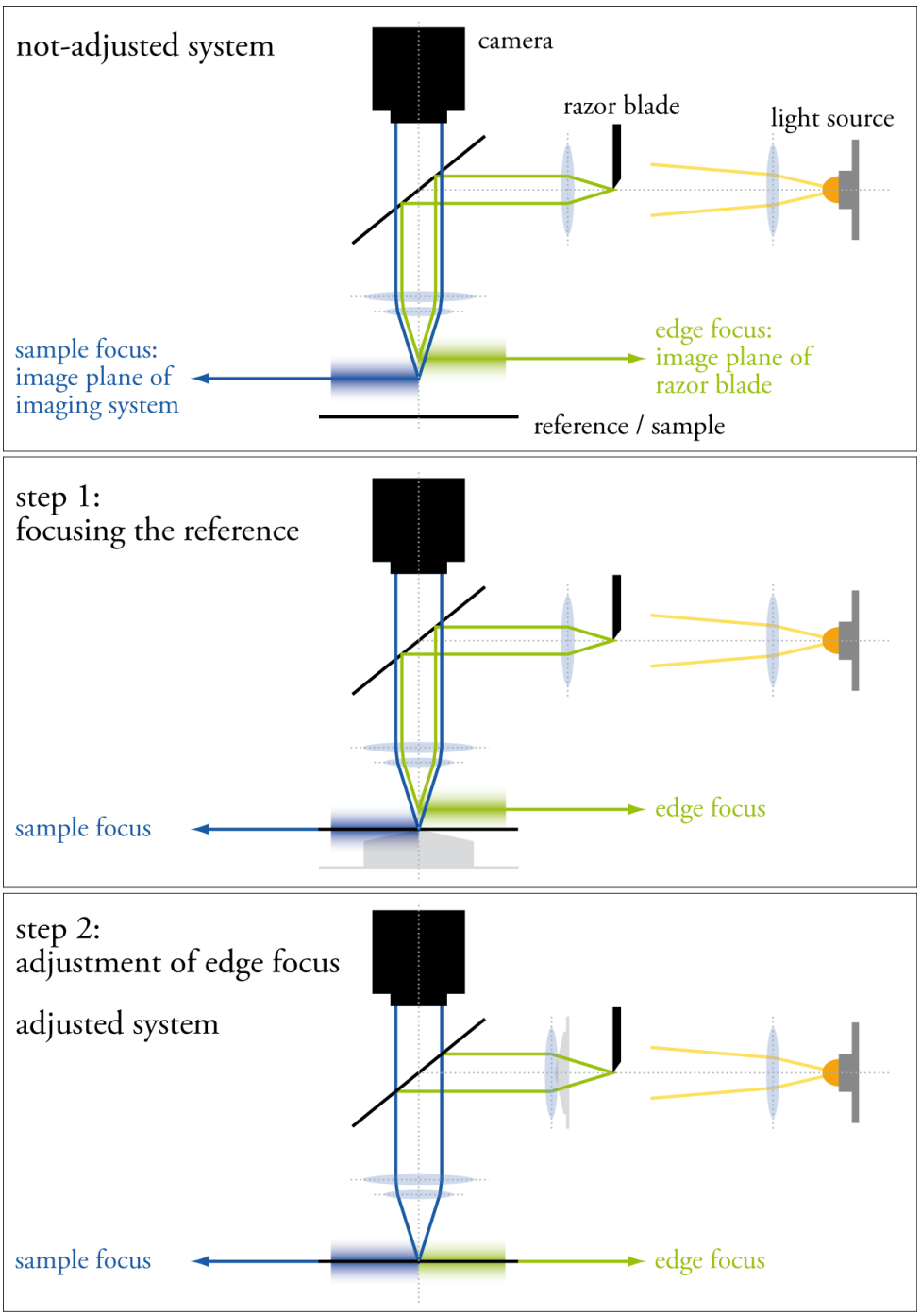

Figure 3.14: Process of focus adjustment.

mirror will be used. The edge's focus has to be modified until its image plane is identical to the image plane of the imaging system, marked by the FS mirror.

With adjusted foci, focusing the sample means to move it along the optical axis of the microscope until its surface is in plane with the image planes of imaging system and edge. An important condition is the smoothness of the sample's surface, which means that its roughness must be much smaller than the illuminating wavelengths. This is valid for the FS mirror but not for paper samples, where the roughness can be up to several microns for uncoated papers [42]. The surface does not form a single plane anymore and this way, several elements of the surface are in the image plane when moving the sample up and down – at least for some region. Therefore, the paper sample itself is not focused but the FS mirror is used as a focusing tool. The alignment of the surfaces is achieved by pressing both against a superfinished plate of the sample holder that can be moved using the microscope stage without leaving the focus plane. Even for the very smooth surface of the FS mirror, the focus is blurred to some extent due to chromatic aberration. Focusing manually therefore means that the plane of best focus can only be guessed and is often missed considerably.

Therefore, an objective measure for the quality of focus is required. Such measures and their reviews can be found in literature [72–89]. A MATLAB implementation of these methods was published by Pertuz [90]. The methods that were tested for the work at hand are listed in table 3.3.

A drawback of some methods is the required threshold definition. This can easily be a source of errors and should be handled with care. The performance of some methods depends on the motive of the captured image, especially if the measure takes into account only the distribution of gray values and not the spatial distribution. Therefore, the methods were tested with typical images of the setup and their performance was rated.

For this work, the focus measure $\mathfrak{F}$ has to be computed and displayed in a live-view window using MATLAB. Methods that require high computation time are not feasible in this case. Thus, a first criterion for choosing the focus measure is the relative computation time. In table 3.3, the computation time ti was calculated relative to the shortest. All values are the average of 32 MATLAB calculations for different images. There was no significant variance in computation time. The results depend on the algorithm used and it is likely that for different images, different implementations of the methods or other programming languages than MATLAB, the results can be different. For further calculations, the methods SFIL, WAVS, WAVV, and WAVR were excluded due to their time costly computations. The applicability of a focus measure depends on whether the maximum of the measure is identical with the point of best focus and how good this maximum can be recognized. For the accuracy criterion (i.e. the distance from focus), images of the evenly illuminated FS mirror were taken. At the beginning, the focus was adjusted manually, using no computed measure of focus but just subjective rating. Then, the microscope stage was moved 100 units in 2-unit steps around the assumed focus. One unit of the scale for

ID	Method	t_i	$\Delta z_{\max,i}$	m_i/σ_i
ACMO	Absolute central moment [86]	5		
BREN	Brenner's focus measure [84]	12	- 0.3	0.09
CONT	Image contrast [81]	17	- 0.4	0.14
CURV	Image curvature [77]	34		
DCTE	DCT Energy measure [85]	69	0.1	0.07
DCTR	DCT Energy ratio [79]	69	0	0.05
GDER	Gaussian derivative [76]	33	0	0.34
GLVA	Gray-level variance [78]	9	0.4	0.46
GLLV	Gray-level local variance [83]	52	3.9	0.33
GLVN	Gray-level variance normalized [84]	9	0.4	0.5
GRAE	Energy of gradient [73]	18	- 0.4	0.11
GRAT	Thresholded gradient [84] (threshold = 0)	12	- 0.2	0.11
GRAS	Squared gradient [74]	7	0.1	0.14
HELM	Helmli's measure [77]	29	2.9	0.12
HISE	Histogram entropy [78]	4	- 1.2	0.16
HISR	Histogram range [75]	1		
LAPE	Energy of Laplacian [73]	6	- 0.4	0.03
LAPM	Modified Laplacian [82]	7	- 0.2	0.06
LAPV	Variance of Laplacian [83]	11	- 0.1	0.15
LAPD	Diagonal Laplacian [87]	12	- 0.3	0.1
SFIL	Steerable filters-based [80]	195		
SFRQ	Spatial frequency [74]	25	- 0.2	0.13
TENG	Tenengrad [78]	19	0.1	1
TENV	Tenengrad variance [83]	25	1.8	0.6
VOLA	Vollat's correlation-based [84]	31	- 0.3	0.34
WAVS	Wavelet sum [89]	133		
WAVV	Wavelet variance [89]	156		
WAVR	Wavelet ratio [88]	272		
	manually	12		

Table 3.3: Overview of focus measures implemented in [90] and criteria for their performance: computation time t_i, accuracy $\Delta z_{\max,i}$, and recognizability m_i/σ_i.

the vertical movement (z-direction) of the microscope stage is about 1 µm [61]. For each step, 15 images were taken. The focus measures $\mathfrak{F}_i(z)$ were calculated for each of these images and then averaged. From these curves, the focus planes $z_{\max,i}$, i.e. the z-values where the measures reach their maxima, could be derived by approximating the zero-crossing of the slopes $\mathfrak{F}'(z_{\max,i}) = 0$. The median $\overline{z_{\max}}$ is assumed to be the true focus plane in the following. Thus, the distance from focus $\Delta z_{\max,i} = z_{\max,i} - \overline{z_{\max}}$ (see table 3.3) indicates, how well the focus plane is coincident with the maximum of the measure $\mathfrak{F}_i$ and thus is a criterion for the accuracy of the measure. For the methods ACMO, CURV, and HISR the focus plane

was not distinct and they were excluded from the investigation.

The last criterion rates the recognizability of the measure. Two factors are important here. The first is the slope mi of the measure around the maximum. The steeper the slope, the easier the maximum can be recognized. For approximating the slope, a line was fit to the last five values before the maximum and the maximum itself. The second factor is how insensitive the measure is against temporal image noise. This was described with the standard deviation σ_i of the focus measure for the 15 images of each step. The standard deviations of the six values used for calculating the slope were averaged. The ratio of slope and mean standard deviation $m_i = \sigma_i$ is the criterion for the recognizability of the measure $\mathfrak{F}_i$.

The following evaluation was restricted to the methods CONT, GDER, GLVA, GLVN, GRAS, LAPV, SFRQ, TENG, and VOLA. The other methods were excluded due to their poor performance. Figure 3.15 illustrates the results of the methods for the evenly illuminated FS mirror. Note the different scaling in the two sections of the figure. The focus measures $\mathfrak{F}_i$ are normalized to 1, plotted over the relative z-position of the microscope stage, where $\overline{z_{\max}}$ is set to zero. The error bars illustrate the standard deviation of the focus measures for one z-position. It becomes clear that a focus measure with a good recognizability does not simply show a steep slope, but that its slope is so steep that the variance of the measure for one z-position becomes insignificant. Although, a scaling of the "flat" focus measures would increase their slopes, it would also increase their standard deviations and this way would not enhance the recognizability. Choosing a focus measure for the measurement setup, a second evaluation followed. This time, the FS mirror was brought to the image plane of the CCD camera using the TENG method as support for focusing manually. Then, the razor blade was positioned into the light path and the edge focus was varied, the procedure similar to the one described before. Only, the scale cannot be transferred to a metric movement of the lens. The focus measures were calculated for the selected methods. The results can be seen in figure 3.16. On the abscissa the lens position is indicated by Δz relative to $z_{\max,\mathrm{TENG}}$. Obviously, some of the selected measures fail when the task is to indicate the edge focus. Only CONT, GDER, GLVN, and TENG show a clear maximum, VOLA a minimum. The z-position of the maximum is about the same for GDER, TENG, and VOLA, whereas CONT and GLVN indicate a different optimum z-position. A closer look at the edges for these two z-positions shows (figure 3.17) that at the z-position indicated by CONT and GLVN the edge is not as steep as at $z_{\max}$. of GDER, TENG, and VOLA. CONT and GLVN fail in terms of identifying the point of best focus. GDER shows better recognizability (normalized to 1) compared to 0.38 for TENG and 0.13 for VOLA. Nevertheless, $z_{\max,\mathrm{GDER}}$ differs to some extent from $z_{\max,\mathrm{TENG}}$ and $z_{\max,\mathrm{VOLA}}$. This and the better performance in the previous evaluation are the reason for TENG being selected for focusing and focus adjustment in the following.

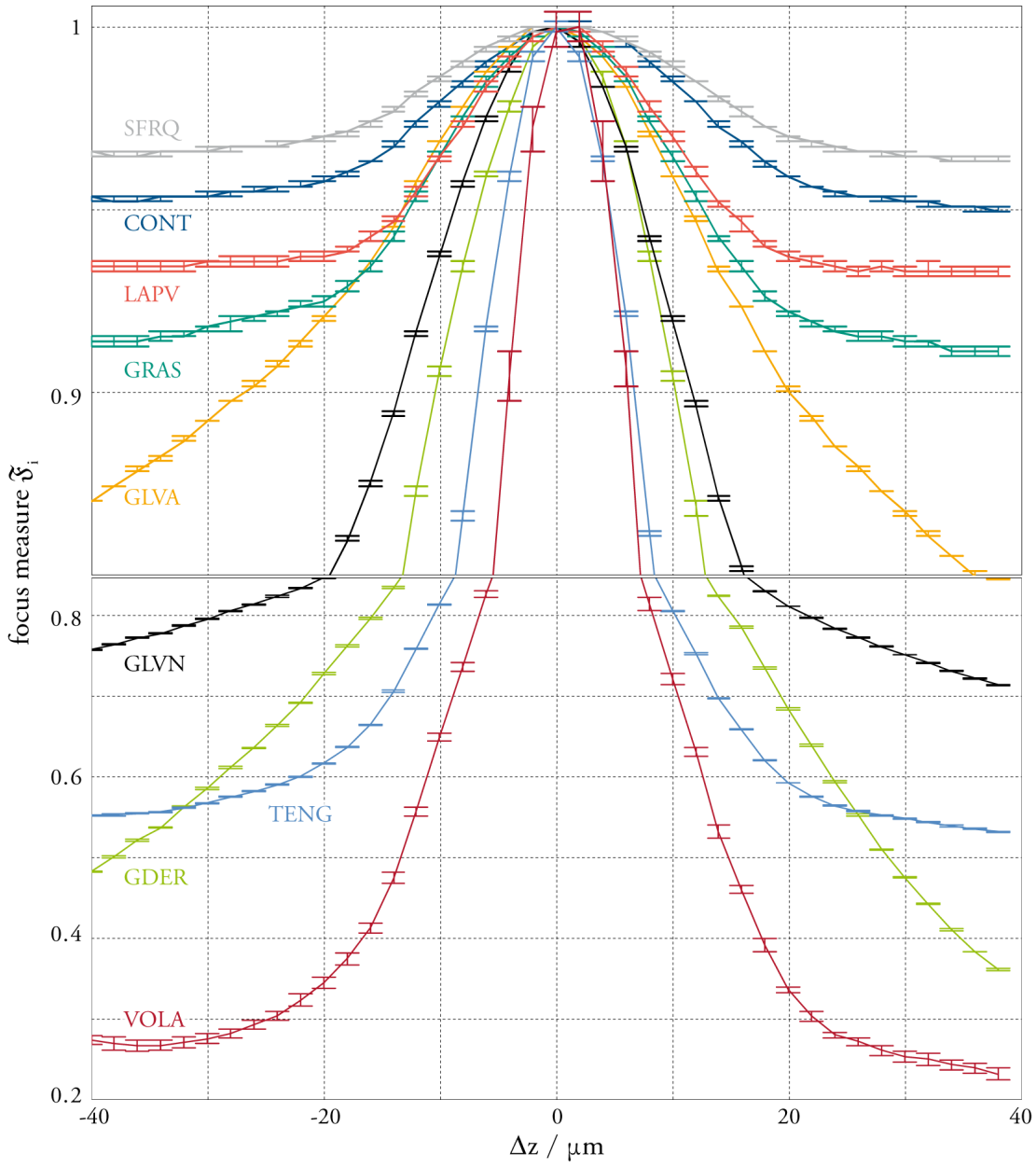

Figure 3.15: Selected focus measures for evenly illuminated FS mirror, plotted over distance from focus $\Delta z = z - z_{\max,\mathrm{TENG}}$.

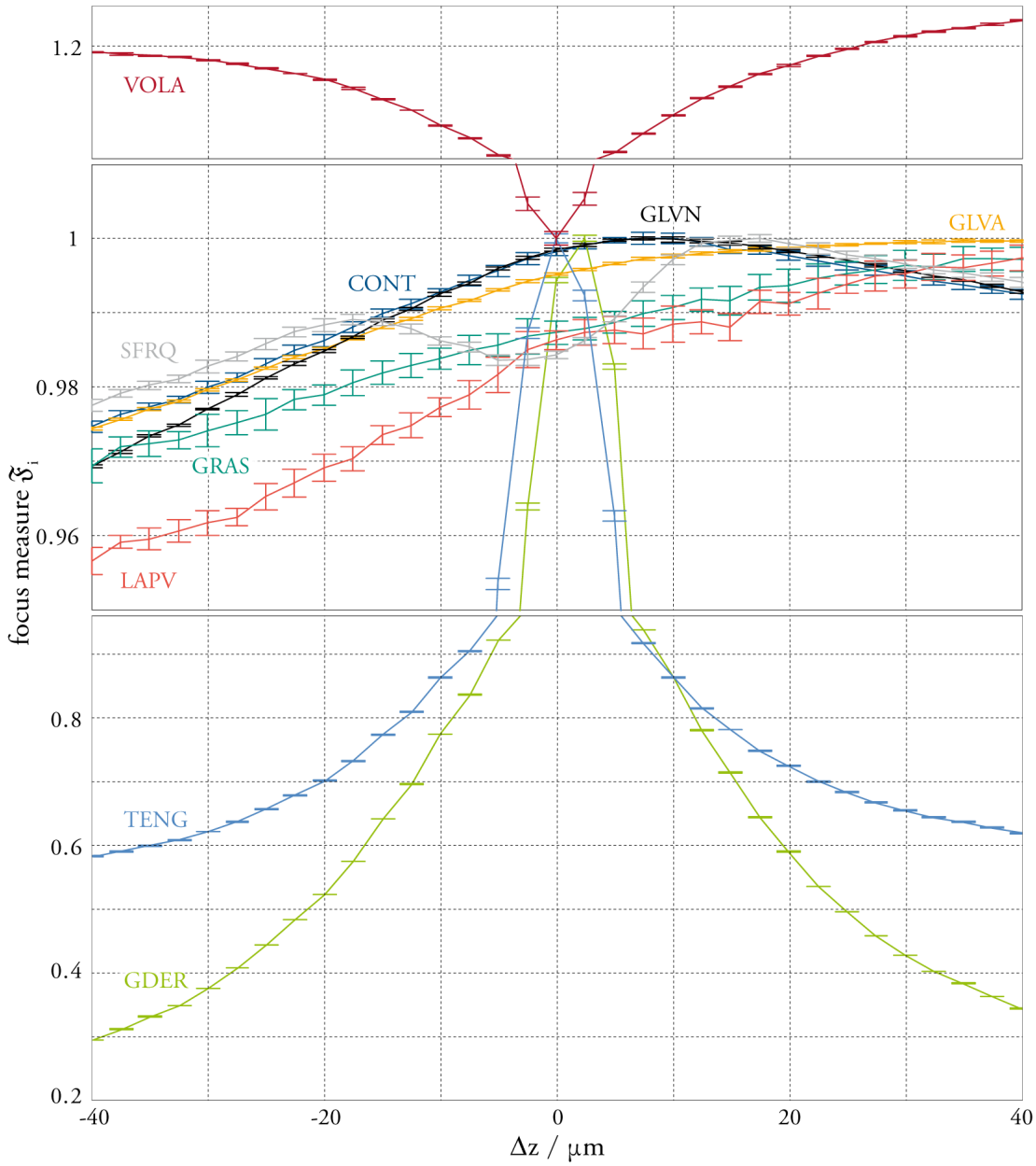

Figure 3.16: Selected focus measures for focus adjustment of the edge, plotted over distance from focus $\Delta z = z - z_{\max,TENG}$.

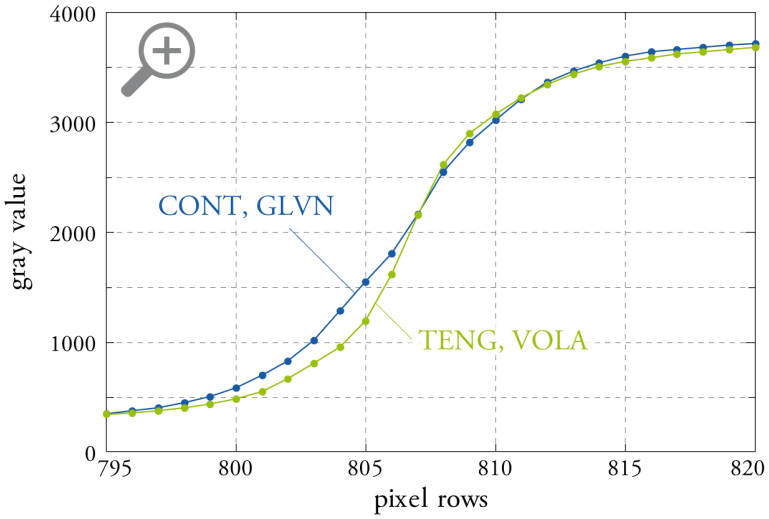

Figure 3.17: Magnification of the edges for $z_{\max}$ of CONT and GLVN and for $z_{\max}$ of TENG, and VOLA.

3.3.4 Performance of the Measurement Setup

The precision of the ESF measurement depends on some factors as the spectrum of the light source, the stability of camera and light source due to temperature and temporal noise, the focusing of the sample, and the distortions when using polarizing filters.

These factors were analyzed according to their influence on the measurement performance of the given setup. The measurement performance can directly be visualized by rating the detected ESF of the FS mirror. In general, distortions were identified by the steepness of the transition between light and dark part. The more this transition resembles a step function, the better is the precision of the image and therefore the precision of the measurement.

For some influencing factors, this identification of the measurement performance failed. In these cases, the rating of the performance is explained separately. Since there is no single identification, it was forebeared from introducing a general rating factor.

Spectrum of the Light Source

A broadband spectrum of the light source leads to chromatic aberration. For the ESF of the FS mirror this means that the edge is afflicted with a certain blurring. Figure 3.18 shows the measured ESFs for halogen and LED light source respectively. The blurring of the ESF measured with halogen light source is clearly visible. Even with the LED, the edge is not perfect. But in comparison to the previous broadband illumination, the accuracy could be improved noticeably. For higher improvements, a monochromatic light source or detection method would be necessary.

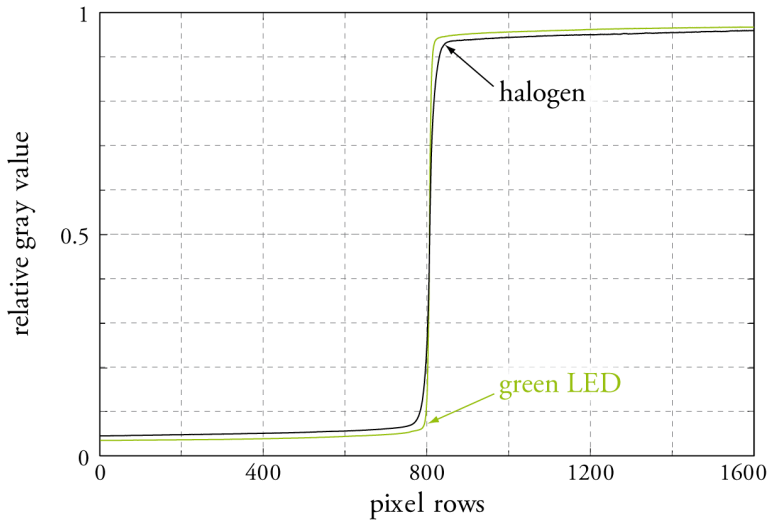

Figure 3.18: ESF of FS mirror for halogen and LED light source.

Temperature and Temporal Noise

The intensity and the emission spectrum of an LED depends on its temperature. When turning on the LED, the temperature increases. Cooling elements are self-evident when working with LED s. In the introduced measurement setup, a passive cooling element was used. Therefore, the LED's temperature increases for a certain time until a steady state is reached. It was found, that after a warming period of approximately 30 minutes the changes are insignificant. For the measurements, this warming period was maintained before the captures started.

The camera did not show any significant change due to temperature. Also, there was no significant influence of the temporal noise of the CCD chip. Therefore, there were no restrictions formulated for the use of the camera.

The temporal noise of the light source was found to be the source of some imprecisions of the measurement. Therefore, the temporal behavior of the two light sources, halogen and green LED, where investigated using a high-speed camera. The light sources were warmed up and the lamp housing was observed with 3200 frames per second. For each frame, the gray value averaged over the central part of light source was used as measure. Figure 3.19 compares the two flickering curves of halogen and LED light source, relative to their mean value.

The flickering of the LED is noisy but the extent of the flickering is relatively small and the flicker frequency is random. The halogen lamp shows a pronounced flicker frequency of 50 Hz.

The flickering of the light source becomes problematic, if the exposure time of the capture is small compared to the flicker frequency. Since the intensity of the halogen lamp is higher than the one of the LED, and therefore, the exposure times of captures with the halogen lamp were much shorter, the

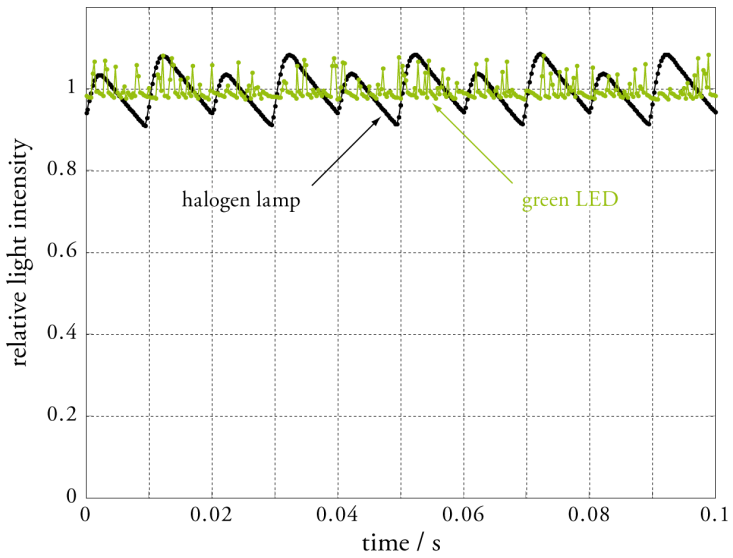

Figure 3.19: Temporal light flicker of halogen and LED light source.

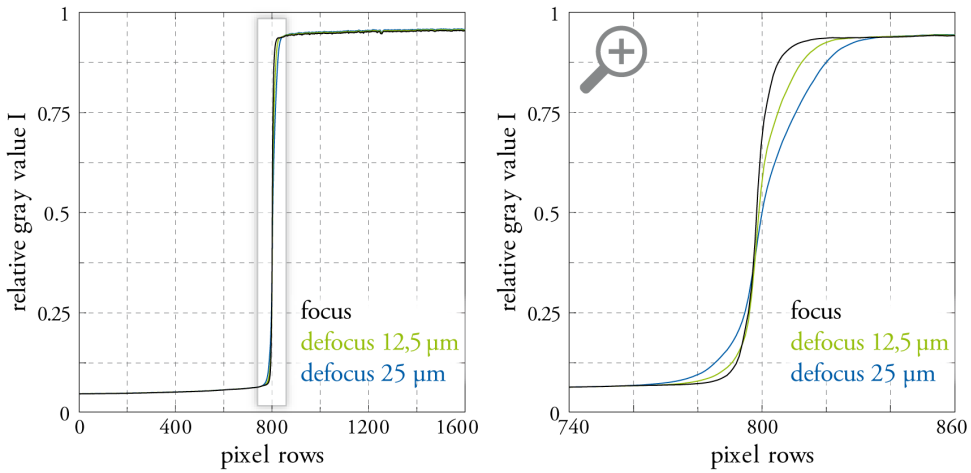

Figure 3.20: Comparison of focused ESF of FS mirror and measurements out of focus with 12.5 µm and .

unwanted flicker effect showed especially when using the halogen lamp. For LED captures, a repetition of nine captures for each measurement were found to be sufficient to reduce the temporal camera noise to an acceptable amount.

Focus

Being out of focus adds an additional blurring to the edge. Figure 3.20 compares three ESFs of the FS mirror; one with maximum focus according to the TENG measure, and two out-of-focus measurements with a 12.5 µm and a 25 µm deviation from the focus plane. In the magnification on the right hand side, the blurring effect is clearly visible.

Image Distortion

Image distortion means a non-uniform scaling of pixel rows and columns. Due to such a distortion, the light scattering measurement would be falsified. Typical distortions are barrel or pincushion distortion. Testing the imaging system for distortions, images of the CERAN stage micrometer were captured, where the micrometer scale was oriented in row and column direction respectively. These images, as shown in figure 3.21 were analyzed with respect to linearity of the lines of the scale. There was no noticeable distortion detected. The same test was performed taking an image of a CMOS chip, where the channels of the chip were checked for their linearity. Again, there was no noticeable distortion.

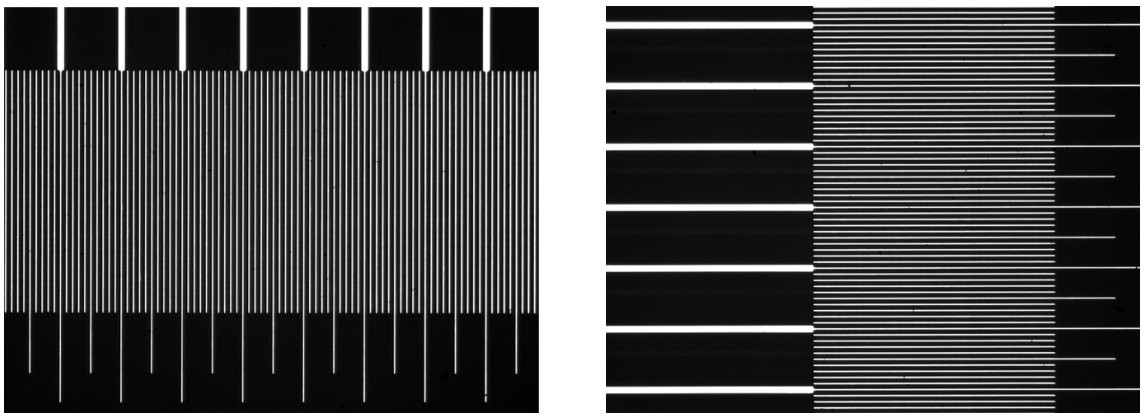

Figure 3.21: Test images of the stage micrometer for detecting image distortions.

Polarizing Filters

Analyzing the effect of surface roughness, two samples are needed that only differ in their surface characteristics. Here the opal glass was used. One side of the opal glass is polished, the other side is left untreated featuring a rough surface. ESF measurements were taken from both sides, each with and without polarizing filters respectively. Figure 3.22 presents the results. On the left hand side, the results without polarizing filters show a big deviation for the rough and the smooth surface of the opal glass. Due to the rough surface, the darker part is lightened up, the lighter part loses reflectance. On the right hand side, the curves for measurements using polarizing filters are very similar although not perfectly identical, but the surface effects were eliminated to a great extend.

Now, the question arises, whether the polarizing filters have a distortion effect on the measurement. For this reason, measurements were taken on the FS mirror, using either no polarizing filter, only the polarizer, or only the analyzer. The FS mirror was focused without any polarizing filter in the light path. Images were captured for each setup without refocusing. A combination of both polarizing filters could not be investigated in this way, because the noise of this measurement was dominating.

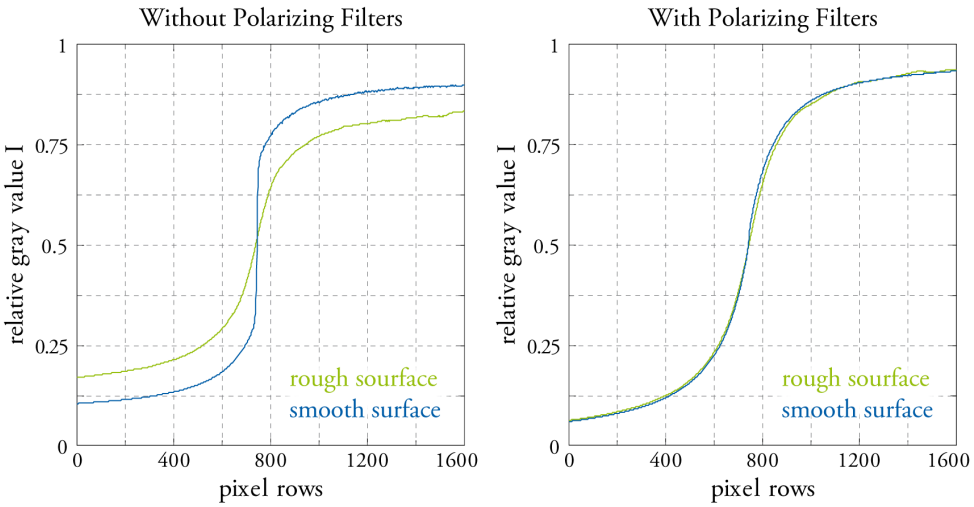

Figure 3.22: Comparison of measurements of the rough and the smooth side of the opal glass sample; without (left) and with polarizing filters (right).

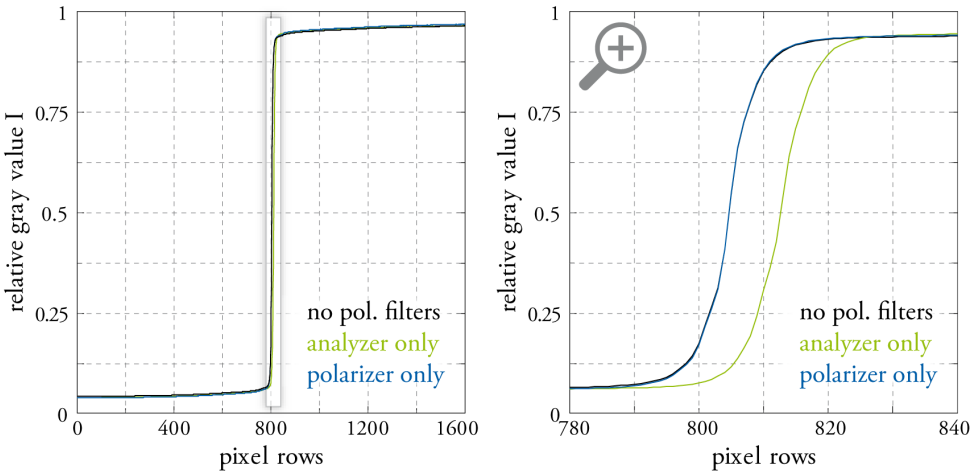

Figure 3.23: Comparison of measurements of FS mirror without polarizing filters, with polarizer only, and with analyzer only.

Figure 3.23 shows the resulting ESFs. The curves measured without polarizing filters and with polarizer are almost identical. Even the magnification on the right of figure 3.23 reveals no significant differences. In contrast to this, inserting the analyzer into the light path makes the edge shift. This shift would be added to the sample image - captured with both polarizing filters - when the reference is captured without any polarizing filters. Since one of the filters can remain in the light path for capturing the reference image, the filter that will be removed is the one that causes less deviations - which is the polarizer in this case.

Stray Light

The longer the exposure time of the capture, the higher the distortions of the captured image due to stray light. Stray light adds a certain amount of light on top of the measurement signal. This decreases the dynamic range of the measurement. The causes of stray light are additional light sources like room lights or a sunny window. With a zero-light measurement, performed under the same conditions as the measurement itself but with the light source turned off, the disturbance of stray light can be reduced. Still, the decrease of dynamic range cannot be undone. Therefore, stray light that is caused by external light sources should be avoided.

Showing the effect of stray light, measurements of the edge on opal glass were taken. One measurement was performed using the black curtain, as it can be seen in the background of figure 3.4 on the right, to suppress stray light from external light sources, one measurement was performed with the curtain removed, allowing the room light to fall onto the sample. For each measurement, a zero-light measurement was performed, turning off the LED. This way, stray light could be detected. Figure 3.24 shows the edges with and without stray light. On the left, the measurements are plotted without correction, on the right hand side, the zero-light measurements were subtracted before processing the images. This zero-light correction reduces the influence of stray light and the curves are almost identical.

A part of detectable stray light cannot be eliminated. It comes from internal reflections and light scattering inside the measurement setup, e.g. at lenses or optical windows, filters and other parts that affect the optical path of the light. Taking account of these deviations, the PSF of the imaging system $\mathcal{P}_o$ was introduced in equation 3.8.

A second source of stray light is light from internal reflections in the measurement device. An investigation showed that the captured internal reflections are drastically reduced using polarizing filters. This means that for the reference capture, the ESF is afflicted with stray light, while the sample capture is almost free of these deviations.

The correct detection of the amount of stray light is very difficult. Therefore, some assumptions will be made for the following measurements. The sample image is free of stray light. The reference image is afflicted with stray light. The amount of stray light is assumed to be 70 % of the darkest value of the reference ESF.

Figure 3.25 shows measurements with and without internal stray light correction. Without correction, the dark part of the reference ESF is lighter than the sample, and the light part is darker than the sample. From physical point of view, this cannot be explained than by the fact of stray light. With correction, the unwanted effect disappears.

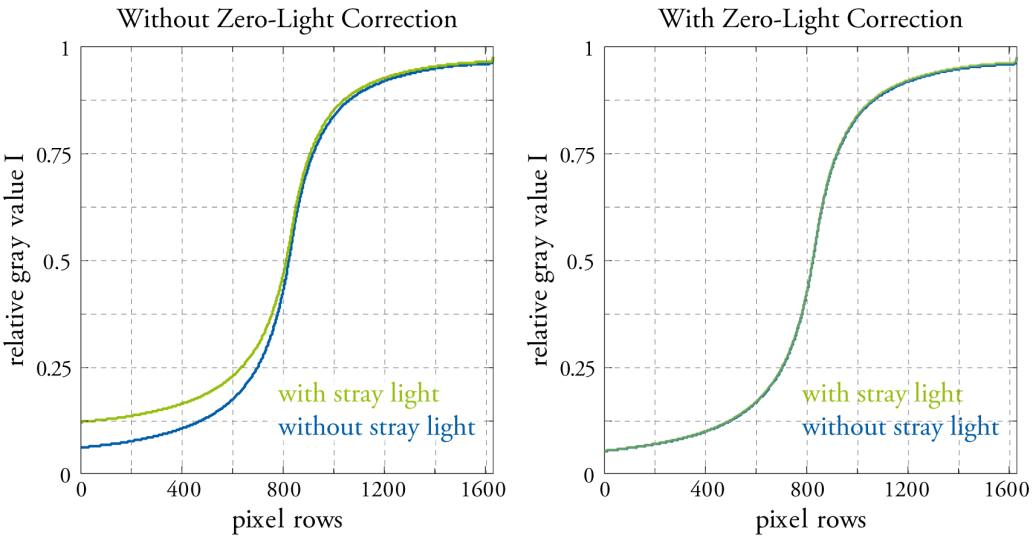

Figure 3.24: Comparison of measurements including and excluding straylight; without (left) and with zero-light correction (right).

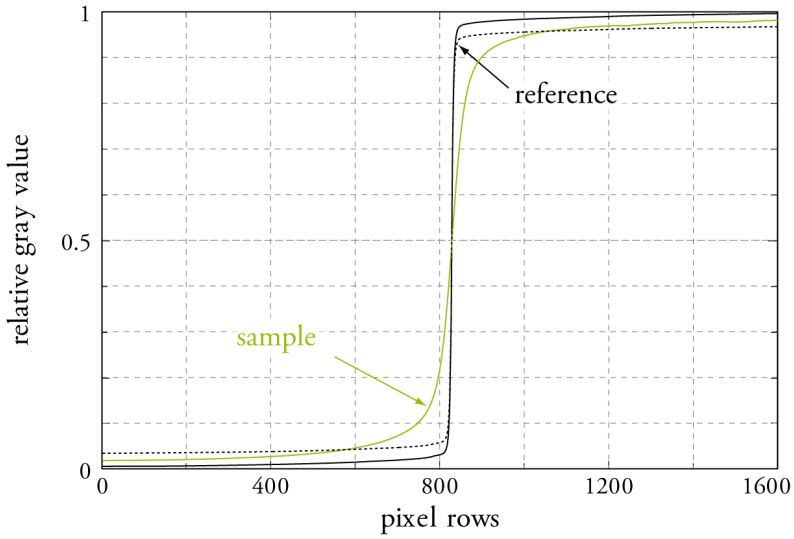

Figure 3.25: Correction of internal stray light: sample ESF (green), reference ESF without (dashed black line) and with correction for internal stray light (solid black line).

3.4 Results

The following results were obtained using the measurement principle derived in section 3.1, realized as described in section 3.3. The setup in brief:

- projection method
- light pattern: edge
- laterally resolved detection using CCD monochrome camera, 12 bit, 2 MP
- measurement geometry: 0°/0°
- spectral sensitivity reduced by using small-band LED as light source suppression of surface reflections by using polarizing filters for the sample measurements
- reduction of distortions of polarizing filters by leaving the analyzer in the light path for the FS mirror reference capture
- enhanced focusing using FS mirror as focusing tool and Tenengrad focus measure
- angular scattering measurement by pivotable sample holder
- pixel resolution of 0.54 µm/px
- suppression of external straylight using black curtain
- internal straylight correction of reference ESF

The measurement images where processed as derived in section 3.2. In total, 33 paper types were investigated, summarized in table 3.4. For each paper type, three samples were measured and the ESFs were averaged. Each sample was measured in six angles, taking nine shots per angle. The angular spacing was 30°. This way, a total angle of 180° was covered.

For each sample, a light reference measurement (unmasked illumination) was taken for deriving the relative gray values. For reducing the measurement effort, this light measurement was only performed for one angle. The applicability to the other angles without falsifying the measurement result was tested exemplarily for arbitrary samples.

For image processing, the images were adjusted according to their edge position, since the repeatability of the edge's position is not perfect and can differ up to 15 pixels.

The results of the ESF measurements can be viewed in figure 3.26. All ESFs significantly differ from the reference ESF captured from the FS mirror. For subsequent investigations, a characteristic length will be introduced, called the 0.1-distance $d_{0.1}$ in the following. This distance is the pixel difference of the ESF in which it decreases from 0.5, which is assumed to be the position of the edge, to 0.1:

$$\begin{aligned} d_{0.1} &= i_{0.5} - i_{0.1} \text{ where} \\ \mathcal{E}(i_{0.5}) &= 0.5 \text{ and} \\ \mathcal{E}(i_{0.1}) &= 0.1. \end{aligned} \tag{3.40}$$

Manufacturer	Series	Coating	Grammage
Felix Schöller	PE-Photopaper (swellable)	glossy	230 g/m^2
	PE-Photopaper (swellable)	matte	230 g/m^2
	PE-Photopaper (microporous)	glossy	240 g/m^2
	PE-Photopaper (microporous)	matte	240 g/m^2
	Proofing Paper	matte	200 g/m^2
	Proofing Paper	matte	275 g/m^2
	Epson Premium Glossy PP	glossy	255 g/m^2
Stora Enso	LumiArt	glossy	100 g/m^2
	LumiArt	glossy	250 g/m^2
	LumiArt	glossy	400 g/m^2
	LumiSilk	matte	100 g/m^2
	LumiSilk	matte	250 g/m^2
	LumiSilk	matte	400 g/m^2
Scheufelen	BVS	glossy	150 g/m^2
	BVS	glossy	170 g/m^2
	BVS	glossy	200 g/m^2
	BVS	glossy	300 g/m^2
	BVS	matte	90 g/m^2
	BVS	matte	115 g/m^2
	BVS	matte	130 g/m^2
	BVS	matte	135 g/m^2
	BVS	matte	150 g/m^2
	BVS	matte	170 g/m^2
	BVS	matte	200 g/m^2
	BVS	matte	300 g/m^2
	Consort Royal	matte	135 g/m^2
	Consort Royal	matte	250 g/m^2
	Job Parilux	glossy	135 g/m^2
	Job Parilux	matte	135 g/m^2
	Job Parilux	matte	250 g/m^2
	heaven 42	matte	250 g/m^2
IGEPA	Evergreen Natural	uncoated	90 g/m^2
	Evergreen Technique	uncoated	148 g/m^2

Table 3.4: Papers investigated.

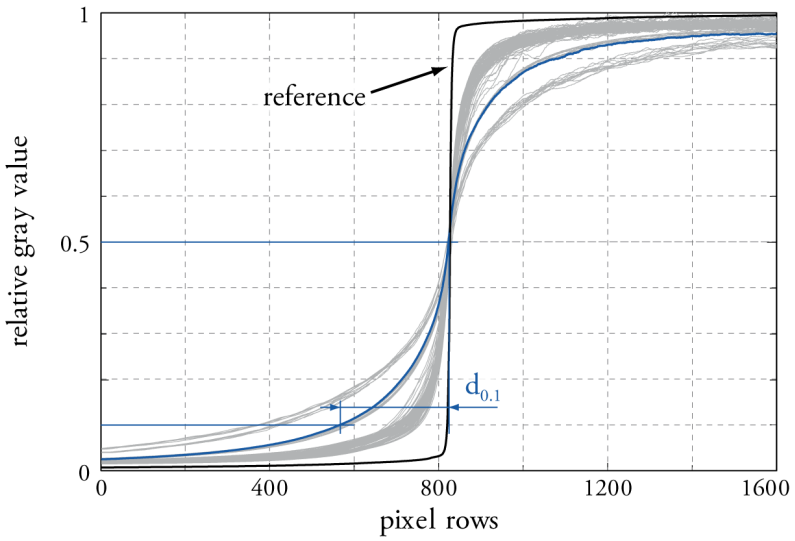

Figure 3.26: ESFs measured for all papers and all angles (gray) in comparison to reference ESF for FS mirror (black); 0.1-distance ($d_{0.1}$) displayed for an arbitrary sample (blue).

In figure 3.26, the 0.1-distance is sketched for an arbitrary sample. Detailed plots of the ESFs for the different papers of the research can be found in appendix B.

3.4.1 Anisotropy of Light Scattering in Paper

For the analysis of the anisotropy of light scattering in paper, the measurements were evaluated with respect to the different rotation angles of the samples. For each measurement, the 0.1-distances were calculated. These distances can be plotted in a polar diagram, where the angle refers to the rotation angle of the measurement and the radius refers to the 0.1-distance. It was assumed that the results correspond for opposing angles, such that the six measurements can be copied for deriving a full circle description. This way, the polar diagram can serve as a kind of indicatrix for easily detecting anisotropy of light scattering. Perfect isotropic scattering would result in equal radii for each measurement angle. The advantage of the 0.1-distances compared to PSF isolines is that the indicatrix can directly be deduced from the ESF and needs no LSF or PSF calculation.

Figure 3.27 shows the indicatrices for selected papers of the research. There is almost no anisotropy for any paper. Thus, the measurements will be averaged over the angles in the following. Detailed indicatrices for all papers can be found in appendix B.

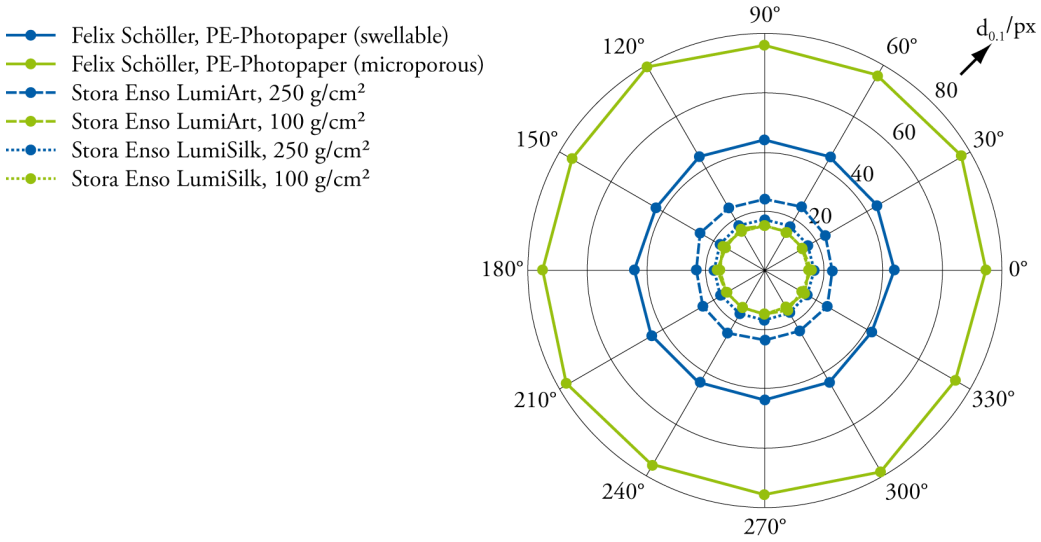

Figure 3.27: Indicatrices of 0.1-distances ($d_{0.1}$) for selected papers of the research.

3.4.2 Light Scattering Classes

Figure 3.26 shows a certain clustering of the ESFs. This implies that paper types can be classified into a limited number of *light scattering classes* (LSC). This way, the complex process of light scattering could be characterized by a single number that could be featured by paper producers [91].

For deriving the light scattering classes, the 0.1-distances were calculated. Figure 3.28 shows a cluster plot of $d_{0.1}$. Here, the similarities of papers can be seen clearly. There are three clusters of papers that can be grouped to light scattering classes, here denoted by the numbers 1 to 3.

The first light scatter class includes all coated and uncoated fine-art papers. They possess very similar light scattering properties. In the second light scattering class, the microporous ink-jet papers can be found. The swellable ink-jet papers are the third light-scatter class. Of course, this classification is very rough. For distinguishing between the papers in one light scattering class, additional information would be needed. Thus, a representation of light scattering using a PSF with a single variable, the form parameter s, would be desirable.

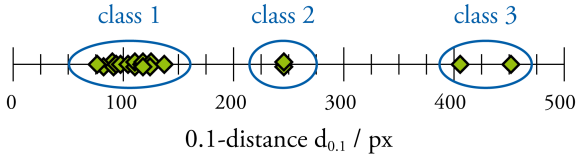

Figure 3.28: Plot of 0.1-distances ($d_{0.1}$) for the different paper types and their clustering into light scattering classes (LSC).

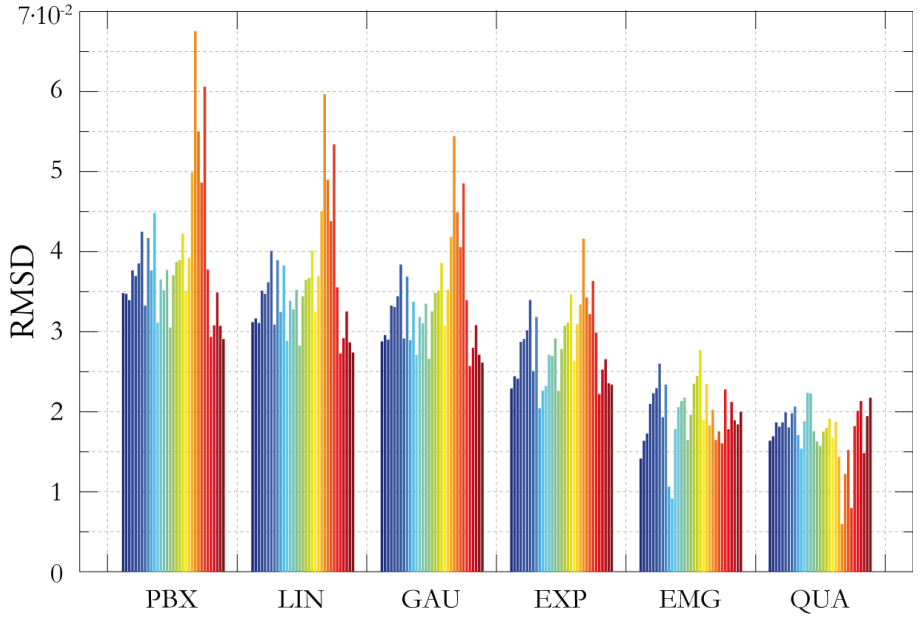

Figure 3.29: RMSD for the different empirical functions as indicator for their performance as LSF approximation for the different papers of the research, variable size of the LSF.

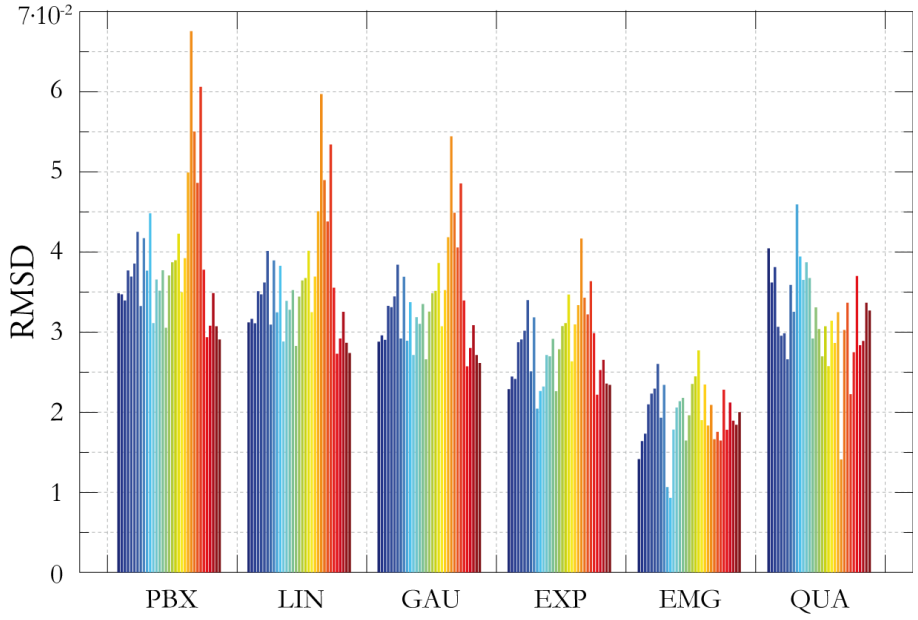

Figure 3.30: RMSD for the different empirical functions as indicator for their performance as LSF approximation for the different papers of the research, fixed size of the LSF.

3.4.3 LSF and PSF Calculation

The processing of PSFs requires an LSF calculation first. The first approach was to fit known empirical functions to the measurements. The analytical LSF formulations were derived from the PSFs, which can be found in appendix A.3. These LSFs were convoluted to the reference ESF derived from the FS mirror, which is assumed to be the best ESF achievable. For the fitting, the *root-mean-square deviations* (RMSD) were minimized using the "fminsearch" MATLAB algorithm. The form parameter s for the best fit was inserted into the analytical formulation of the PSF.

The performance of the different empirical formula was found to be depending on the type and the grammage of the papers. In general, Gustavson's modified exponential formula EMG and the quadratic function QUA featured the best results. Figure 3.29 shows the RMSDs for the different papers (indicated by different colors) and empirical functions as an indicator for the goodness of the fits. These results were derived with variable size of the LSF. In a second run, the extent of the LSF was set to 1600 px, which is the size of the ESF evaluated. Fixing the size of the LSF affects the RMSDs noticeably for the quadratic function QUA, as it can be seen in figure 3.30. This is caused by its formulation, where the scaling factor depends on the extent of the LSF since the indefinite integral cannot be solved, see appendix A.3.

An example of the resulting ESF approximations for the different functions can be viewed in figure 3.31. The reference ESF, used for convolution with the LSF, is marked with a black solid line, the sample ESF with a red solid line. The numbers in the legend indicate the RMSD performance of the functions. Detailed RMSD and the identified LSF and PSF results can be found in appendix B.

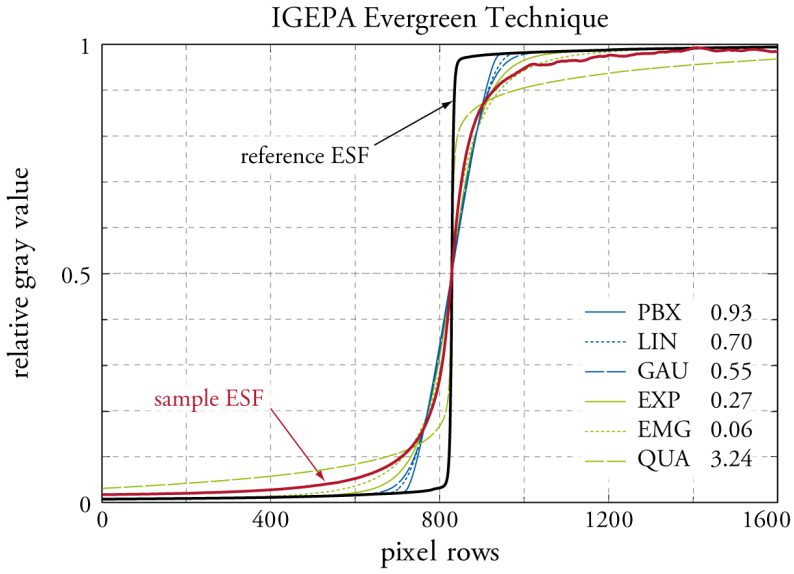

Figure 3.31: IGEPA Evergreen Technique ESF approximations for the different empirical functions, fixed size of the LSF; numbers in the legend indicate the RMSD.

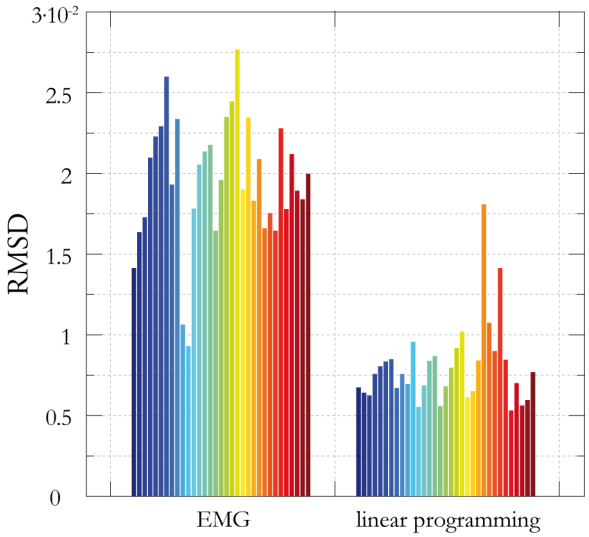

Figure 3.32: Comparison of RMSDs for the best empirical function EMG with the RMSDs for linear programming for the different papers of the research.

In a second step, the linear programming approach was tested to derive the LSFs. In order to reduce the long calculation times, the size of each LSF was restricted to 1601 px. Figure 3.32 compares the resulting RMSD for the linear programming approach with the RMSD for the EMG empirical function. Using linear programming, the RMSD could be reduced drastically for some paper samples.

Figure 3.33 presents the calculated LSFs for IGEPA Natural Technique, an uncoated paper. The LSF derived by linear programming is piecewise linear. This fact implies that the degree of freedom of the linear programming was too high. This effect was observed for all papers of the research.

The only empirical function that is similar to the general run of the LSF derived by linear programming is the EMG-LSF. This is a first hint for the validity of this function. All other empirical functions will be omitted for the subsequent investigations.

3.4.4 Spectral Properties of Light Scattering

Light scattering depends on the spectral distribution of the light source. Thus, a spectral measurement of light scattering could be used to improve light scattering models. For deriving spectral properties of light scattering, the green LED was replaced by a red and a blue LED. These different spectral characteristics were used to generate a rough spectral estimation of light scattering. The maximum wavelengths of the LEDs were at approximately 457 nm, 536 nm, and 632 nm respectively. The approximated form parameters s for the EMG empirical equation were plotted over the maximum wavelengths of the LEDs, see figure 3.34.

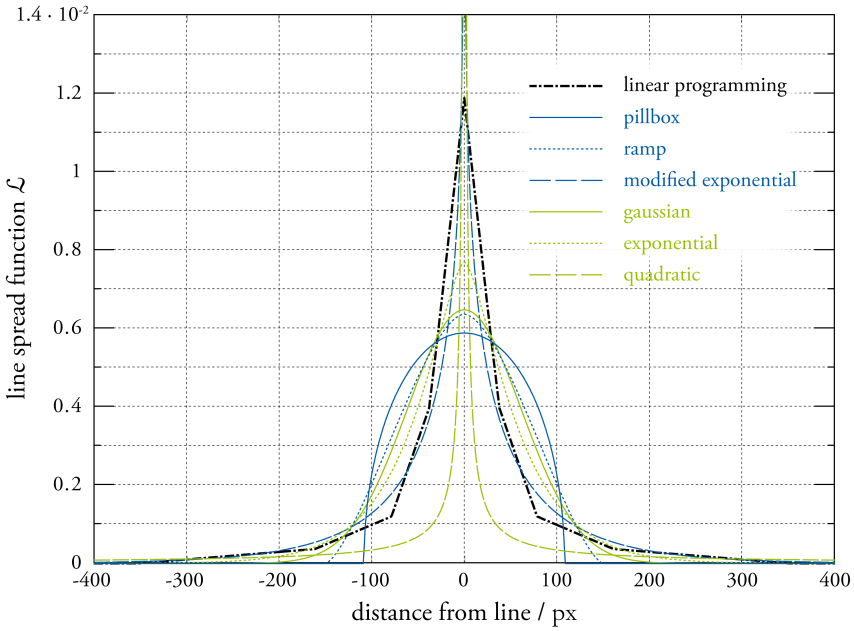

Figure 3.33: Approximated LSFs for IGEPA Evergreen Technique.

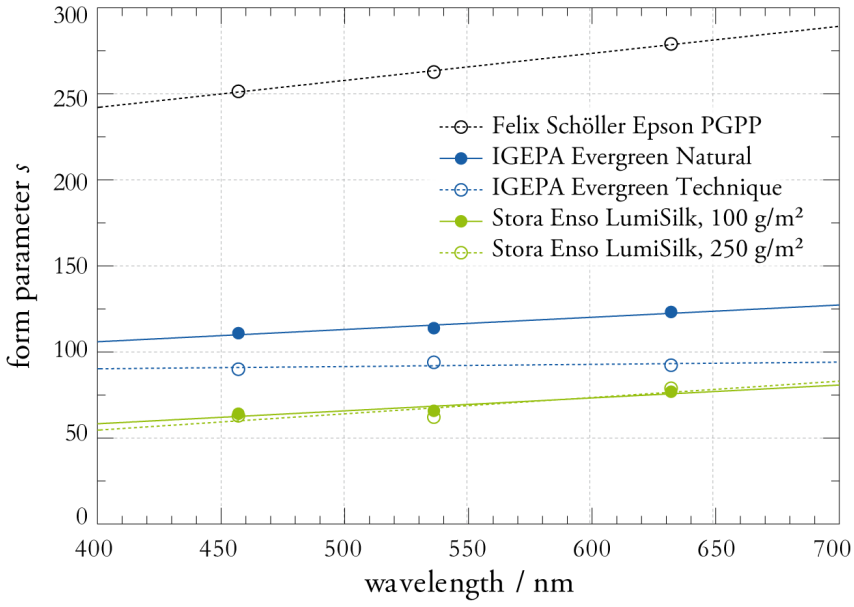

Figure 3.34: Form parameters s over the maximum wavelength of the three LEDs.

For most papers of this investigation, a linear approximation seems to be reasonable. The parameters of these linear equations are assumed to be a function of the mean form parameter s. However, a clear relation could not be found and needs further investigations. A general trend for increasing light scattering with higher wavelengths can be noticed. Nevertheless, this spectral trend is small compared to the difference between papers and the measurement accuracy. Therefore, the light scattering will be assumed to be constant over the wavelength for the following chapter.

4

Application on Monochrome Halftones

With the measurement setup presented in chapter 3.3 the light scattering properties of paper were measured. However, the applicability of the measurements for predicting *optical dot gain* (ODG) must be ascertained. Therefore, simulations of ODG were computed which were based on some exemplary measurements of the results in section 3.4. This simulated ODG was compared with direct ODG measurements from microscopic and densitometric measurements. The results of this comparison will be presented in sections 4.1 and 4.2. The results of this investigation serves as a validation for the measurement results.

The additional benefit of the light scattering description by means of a PSF is that it allows for analytical evaluations. This will be demonstrated by deriving an empirical function for ODG that only depends on known parameters like the transmittance of the ink, the screen frequency, the fractional area coverage of the halftone, and the light scattering parameter that was identified by the measurements using the setup presented. The advantage of such a representation for ODG is the fact, that there is no need for printing patches and fitting parameters like it is common practice i.e. for deriving the n-factor of the Yule-Nielsen model of ODG.

For the following sections, all light scattering will be based on the EMG function and the dimension of the scattering will be described using the form parameter s. To limit complexity, all halftones used for the investigations were conventional AM screens.

4.1 Contact Method with Halftone Pattern

The first approach to validate the light scattering measurements of the previous chapter was based on a different measurement design for light scattering, that can be easily compared to real prints.

Contact method and halftone pattern of a developed film were used to simulate perfect dots on the substrates. With a spectrodensitometer, a measurement geometry of 45°/0° with area integrated measurement of the reflectance was realized. As it is typical for densitometric measurements, polarizing filters were used. From the measurements, the tone response curves were derived and compared to simulated results that were based on the PSF calculations according to the previous measurements.

This investigation was taken out on selected substrates:

- opal glass, glossy side
- Stora Enso, LumiSilk, 100 g/m^2
- Stora Enso, LumiSilk, 250 g/m^2
- Felix Schöller, Epson Premium Glossy Photo Paper, 255 g/m^2

4.1.1 Measurements

For the experiment, a film was designed containing patches with different fractional area coverages using a conventional AM screen with $f_s = 40$ l/cm frequency. The nominal coverages were 5 %, 10 %, 20 %, 30 %, 40 %, and 50 % with positive dots, 60 %, 70 %, 80 %, and 90 % with negative dots, as well as 0 % and 100 % solid patches.

Determining the geometrical coverages, the film was measured with the digital microscope Techkon DMS 910 (film mode). The measured geometrical coverages $A_{g,m}$ can be found in table 4.1.

For the densitometric measurements, the spectrodensitometer Techkon SpectroDens was used. This device calculates the density according to DIN 16536 [34] from the measured spectra, having a 45°/0° geometry and polarizing filters. The film patches were placed on top of the sample and the density for black ink D'_k was measured. The reference for unprinted substrate was measured using the 0 %-patch. The solid ink density was substituted by a measurement of the 100 %-patch.

It was found that the density measurements vary for the same patch. The cause for this fact is the coarse screen and the small field of detection of the measurement device. Therefore, each density measurement was taken five times, repositioning the densitometer each time.

From these measurements, the effective coverages $A_{e,m}$ were calculated according to inverse Murray-Davies (equation 2.42):

$$A_{e,m} = \frac{1 - 10^{-D'_A}}{1 - 10^{-D'_i}}$$

where D' is the relative ink density of the full tone (index i) and the halftone (index A). The results are summarized in table 4.1 and figures 4.3 and 4.3 show the related tone response curves on the left hand side, the ODG curves on the right hand side.

4.1.2 Simulation

The simulation of ODG was based on the screen of the film patches. For each measured geometrical coverage $A_{g,m}$, digital masks $\mathcal{M}$ for the screen cells were generated with geometric coverages $A_{g,s}$. Due to discretization, the desired values from the measured coverages could not be perfectly realized. The pixel size of the mask was fixed to 0.54 µm, which equals the camera resolution of the measurement setup in section 3.3. This way, the scattering measurements could directly be applied to the screen cells. The pixels of the masks took only two values: zero (indicating a dot) and one (indicating transparency).

From spectral measurements, the reflectance of the substrate and the transmittance of the solid 100 %-patch of the film were determined. All spectra were approximately constant over the visible wavelength range. Therefore, a mean reflectance R_p of the substrate and a mean transmittance T_i were calculated.

The model for the reflectance simulation of the halftones is illustrated in figure 4.1. The dot gain process was divided into three subsystems. The first is when the light passes the film the first time. Here, the transmittance of the film and the pattern of the mask $\mathcal{M}_A(i,j)$ create a lateral light distribution $I_{1,A}$ which depends on the fractional area coverage A. Assuming a uniform irradiance $I_0(i,j) = I_0$, the light distribution behind the film is:

$$I_{1,A}(i,j) = I_0 \cdot [\mathcal{M}_A(i,j) + (1 - \mathcal{M}_A(i,j)) \cdot T_{45^\circ}] \,, \tag{4.1}$$

where T_{45° is the transmittance of the full tone for the path length of 45° irradiance.

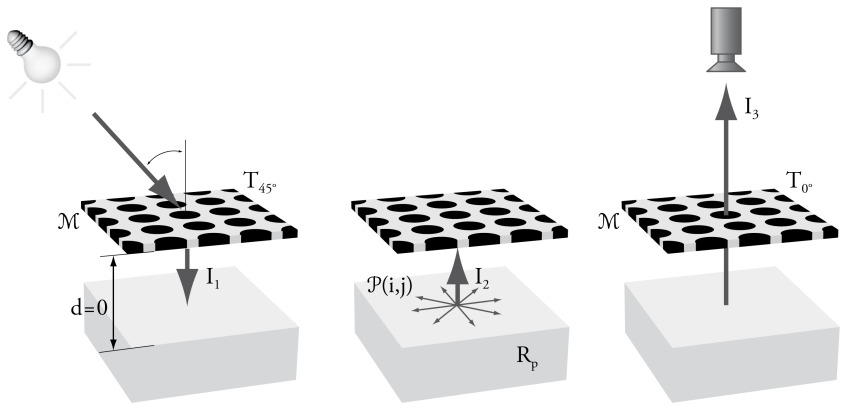

Figure 4.1: Simulation of effective reflectance of a halftone for the prediction of optical dot gain. The measurement geometry equals to that of densitometric measurements.

T_{45° can be calculated from the measured transmittance T using the law of Bouguer-Lambert [92]:

$$T_{45^\circ} = T^{\frac{\sqrt{2}}{1+\sqrt{2}}}. \tag{4.2}$$

The transmittance for 0° observation can be calculated accordingly:

$$T_{0^\circ} = T^{\frac{\sqrt{1}}{1+\sqrt{2}}}. \tag{4.3}$$

The second subsystem describes the light scattering and the reflectance of the substrate. The exitance $I_{2,A}$ can be calculated from the irradiance $I_{1,A}$ as follows:

$$I_{2,A}(i,j) = R_p \cdot I_{1,A}(i,j) * \mathcal{P}, \tag{4.4}$$

where R_p is the reflectance and $\mathcal{P}$ the PSF of the substrate as derived from the measurements of section 3.4.

In the last subsystem, the light passes the film a second time, now in 0° observation angle. This yields to the total exitance:

$$I_{3,A}(i,j) = I_{2,A}(i,j) \cdot \left[\mathcal{M}_A(i,j) + (1 - \mathcal{M}_A(i,j)) \cdot T_{0^\circ}\right]. \tag{4.5}$$

With the constant irradiance I_0, the simulated reflectance distribution can be calculated:

$$R_{s,A}(i,j) = I_{3,A}(i,j)/I_0. \tag{4.6}$$

Figure 4.2 illustrates the digital halftone masks $\mathcal{M}(i,j)$, the simulated reflectance distribution $R_{s,A}(i,j)$ based on the light scattering measurements for opal glass, and captures from the camera of the halftone film on the opal glass sample. The digital halftone mask, which is shown in the top row, can also be seen as a representative for a totally non-scattering medium. An example for this could be a perfect FS mirror. Each halftone consists only of two reflectance values: low reflectance at dot locations and high reflectance for the uncovered space in between. The transition between these two reflectances is a perfect step.

In contrast to this, the simulated reflectance of the halftones in the second row show the typical dark halo and a general darkening of the uncovered space between the dots. These effects are caused by the light scattering in the medium. Also the captured micrographs of the real opal glass sample covered with the halftone film show similar effects (bottom row of figure 4.2).

For simulating ODG, the lateral distribution of the reflectance was simulated as illustrated in figure 4.2). For the subsequent calculations, the mean reflectance $\overline{R}_{s,A}$ was computed according to:

$$\overline{R}_{s,A} = \frac{1}{i \cdot j} \sum_i \sum_j R_{s,A}(i,j). \tag{4.7}$$

From this value, the effective coverage $A_{e,s}$ could be calculated according to the inverse Murray-Davies equation 2.41. The results can be found in table 4.1 and figures 4.3 and 4.3.

For each simulation, an n-factor of the Yule-Nielsen model (equation 2.43) was fitted to the results. The relevant curves are plotted in figures 4.3 and 4.3. The Yule-Nielsen curve is for reference only. It will not be included into the discussion of the results.

4.1.3 Discussion of Results

Table 4.1 presents the results of the measurements and the simulations. For the simulations, the measured geometric coverages of the film could not be reproduced perfectly. The source for this deviation is the lateral discretization of the masks. Especially at small coverages, this deviation is significant. Therefore, the tone response curves for the measurements in figures 4.3 and 4.3 show the measured effective coverages $A_{e,m}$ against the measured geometric coverages $A_{g,m}$ of the film as abscissa, whereas the simulated effective coverages $A_{e,s}$ are plotted against the geometric coverages $A_{g,s}$ of the digital masks.

Figures 4.3 and 4.3 show the tone response curves and the curves for ODG for the simulated and measured results. The simulations are a satisfactory approximation for the measured optical dot gain, especially for the midtones 30 %, 40 %, and 50 %. For opal glass, the measurements and simulations of

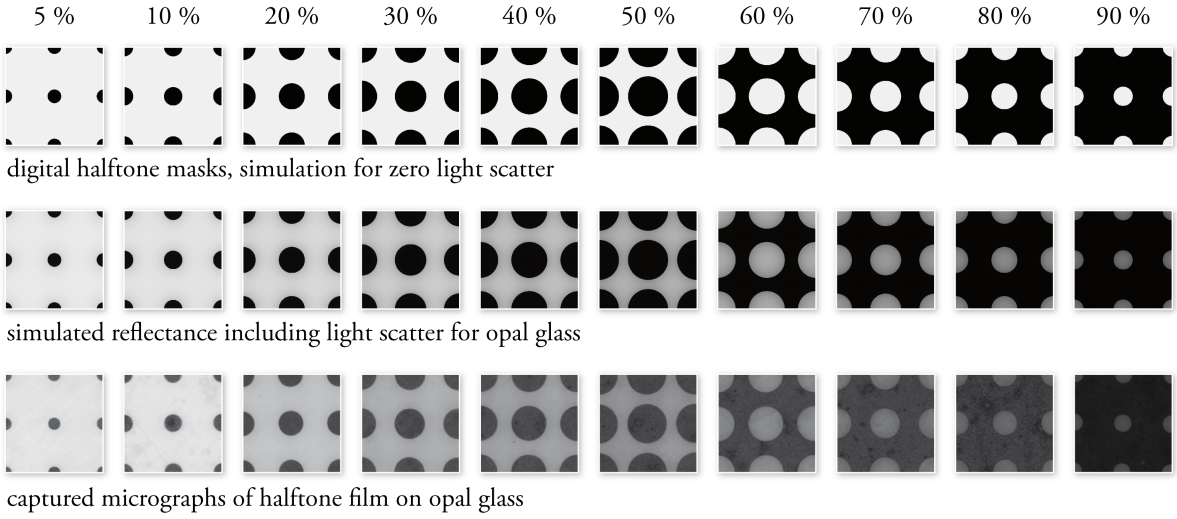

Figure 4.2: Exemplary screen cells; simulation for zero light scattering (top), simulation for light scattering of opal glass (center), and captured micrograph on opal glass (bottom).

Nominal			**5**	**10**	**20**	**30**	**40**	**50**	**60**	**70**	**80**	**90**
Opal glass												
measured	geometric	$A_{g,m}$	6	10	20	30	42	52	58	69	78	88
	effective	$A_{e,m}$	6	11	31	44	57	70	73	87	93	97
simulated	geometric	$A_{g,s}$	6	11	22	32	42	52	58	69	78	88
	effective	$A_{e,s}$	10	17	32	45	56	67	72	81	88	94
Stora Enso LumiSilk 100 g/m^2												
measured	geometric	$A_{g,m}$	6	10	20	30	42	52	58	69	78	88
	effective	$A_{e,m}$	7	16	30	40	51	61	66	75	84	92
simulated	geometric	$A_{g,s}$	6	11	22	32	42	52	58	69	78	88
	effective	$A_{e,s}$	9	15	28	39	50	61	66	76	84	92
Stora Enso LumiSilk 250 g/m^2												
measured	geometric	$A_{g,m}$	6	10	20	30	42	52	58	69	78	88
	effective	$A_{e,m}$	9	15	28	40	50	61	66	74	83	91
simulated	geometric	$A_{g,s}$	6	11	22	32	42	52	58	69	78	88
	effective	$A_{e,s}$	9	15	28	39	50	61	66	76	84	92
Felix Schöller Epson Premium Glossy Photo Paper												
measured	geometric	$A_{g,m}$	6	10	20	30	42	52	58	69	78	88
	effective	$A_{e,m}$	11	22	36	49	60	71	75	83	91	96
simulated	geometric	$A_{g,s}$	6	11	22	32	42	52	58	69	78	88
	effective	$A_{e,s}$	11	17	32	45	57	67	73	82	88	95

Table 4.1: Comparison of geometric and effective coverages for the ODG experiment using a halftone film.

the negative screens from 60 % to 90 % show bigger deviations. Also, the lighter tones 5 % and 10 % do not fit very well. The cause for these differences can be either errors in the measurement of the geometric coverages of the film or errors in the densitometric measurements.

For the two LumiSilk samples, the simulated and measured effective coverages show good conformity for almost all coverages. For the Epson Photo Paper, the ODG is slightly underestimated. Nevertheless, it can be assumed that for the papers of this investigation, the measured PSF is valid. The differences in measurement and simulation are assumed to be caused by the uncertainty of densitometric or microscopic measurements of the coverages. An additional cause might be the possible shadowing from the 45°/0° measurement geometry or multiple reflections in the film.

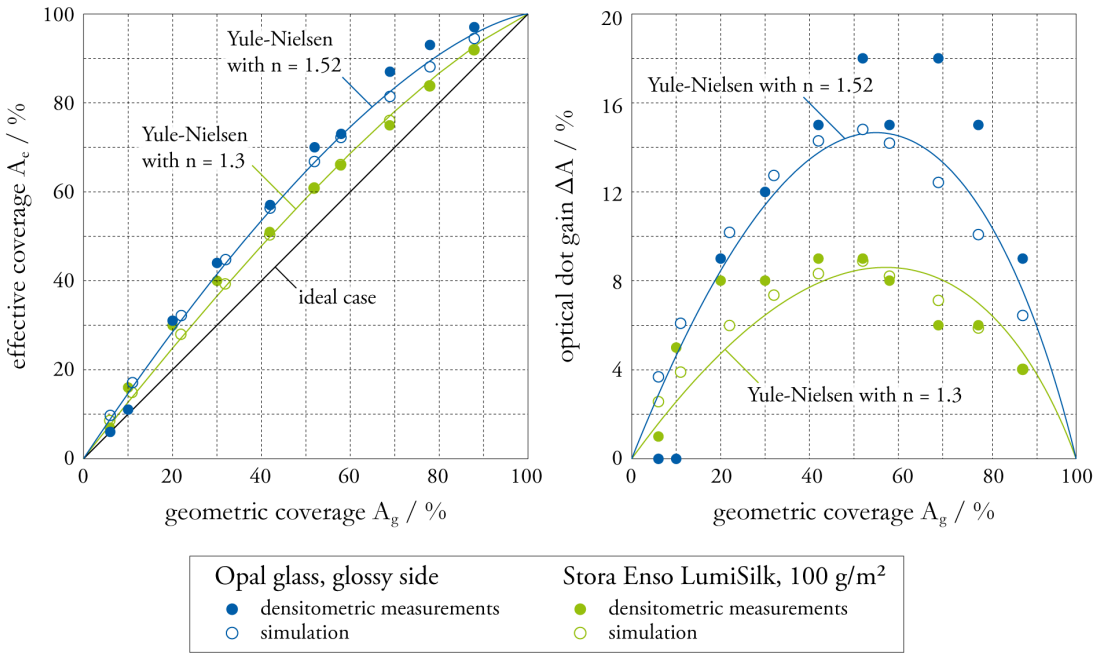

Figure 4.3: Results of the experiment of a halftone film attached to the samples; tone response curves and ODG curves from densitometric measurement, dot gain simulation, and Yule-Nielsen approximations for opal glass and Stora Enso LumiSilk 100 g/m^2.

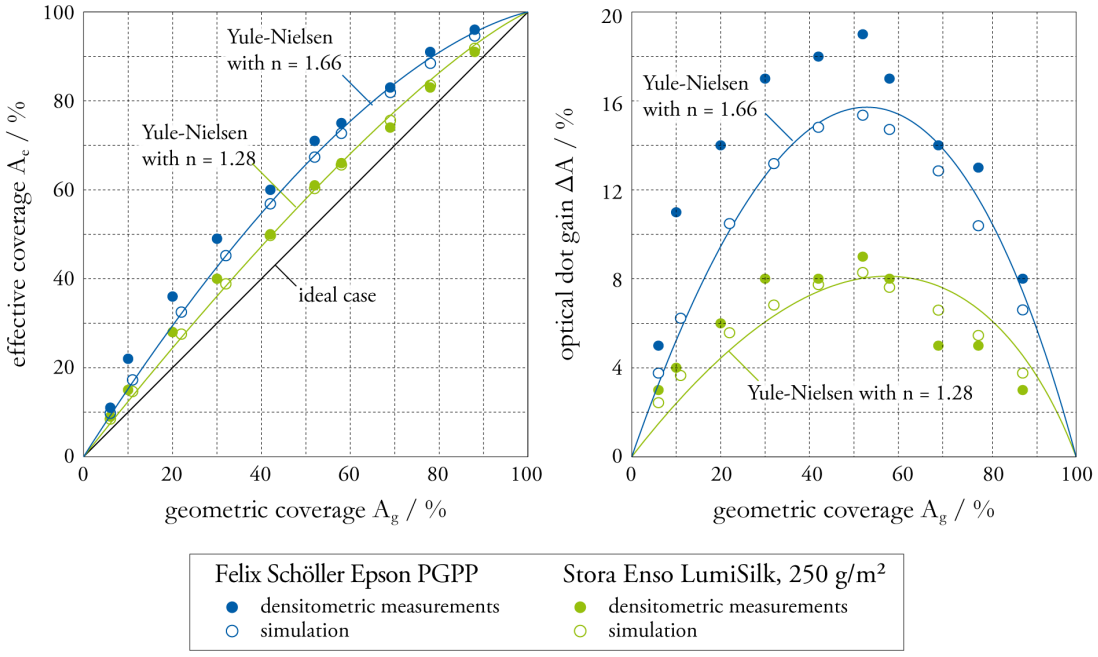

Figure 4.4: Results of the experiment of a halftone film attached to the samples; tone response curves and ODG curves from densitometric measurement, dot gain simulation, and Yule-Nielsen approximations for Felix Schöller Epson Premium Glossy Photo Paper and Stora Enso LumiSilk 250 g/m^2.

4.2 Application on Monochrome Prints

In the following section, the light scattering measurements were applied to real prints. For reasons of comparability, a conventional AM screen was chosen, again with a 40 l/cm frequency (as in section 4.1).

4.2.1 Experiment

For printing the chosen AM screen, a layout was designed that was printed with a DIMATIX Inkjet Printing System DMP-2831, where each drop of ink can be controlled separately and no *raster image processor* (RIP) is needed.

The two papers of this investigation were Stora Enso Lumisilk (250 g/m^2) and Felix Schöller Epson Premium Glossy Photo Paper (PGPP). The ink spread on the two papers differed. Therefore, different dot frequencies had to be used. The Felix Schöller Epson PGPP was printed with a dot pitch of 30 µm (847 dpi), Lumisilk with a dot pitch of 40 µm (635 dpi). The screen frequency was fixed at 40 l/cm.

The geometric area coverage was derived using micrographs that were captured with the Techkon DMS 910, and calculated using a Photoshop algorithm similar to the one presented by Nyström [93], which proved to be more reliable than the integrated algorithm of the associated Techkon software.

Ink densities and reflectances were measured with the Techkon SpectroDens. Effective area coverage and ODG were calculated, as already presented in section 4.1.1. The reflectances of the prints were simulated as described in section 4.1.2 and the effective area coverage and ODG of the simulation were calculated accordingly. The results are summarized in table 4.2 and figure 4.5 shows the related tone response curves on the left hand side, the ODG curves on the right hand side.

4.2.2 Discussion of Results

Table 4.2 and figure 4.5 present the results of the measurements and the simulations. While the prediction for Stora Enso LumiSilk was close to the measurement, the deviation between simulation and measurement for the Felix Schöller Epson PGPP was significant.

It is unlikely, that the deviations for the inkjet paper of Felix Schöller only arise from inaccuracies of the measurements, or from different measurement geometries of densitometric and light scattering measurements. It seems, that for the printed samples, some more effects have to be taken into account in order to accurately model ODG. Two examples for such extended models in literature are the transmittance based model of Ukishima [94] and the physical model of the toner distribution of an electrophotography printer presented by Mourad [7]. Here, ink-spread and inhomogeneous distribution of the ink layer thickness have been taken into account. It is reasonable, that the ODG simulation could be enhanced noticeably when incorporating these two effects into the simulation model. Nevertheless, this would go beyond the scope of this work.

Nominal			**5**	**10**	**20**	**30**	**40**	**50**	**60**	**70**	**80**	**90**
Stora Enso LumiSilk 250 g/m^2												
measured	geometric	$A_{g,m}$	9	15	25	35	46	54	56	66	75	84
	effective	$A_{e,m}$	9	16	30	41	52	62	64	74	83	92
simulated	geometric	$A_{g,s}$	6	11	22	32	42	52	58	69	78	88
	effective	$A_{e,s}$	8	13	25	36	47	57	63	73	81	90
Felix Schöller Epson Premium Glossy Photo Paper												
measured	geometric	$A_{g,m}$	10	16	29	41	50	59	61	72	80	90
	effective	$A_{e,m}$	20	32	50	63	73	80	81	88	93	97
simulated	geometric	$A_{g,s}$	6	11	22	32	42	52	58	69	78	88
	effective	$A_{e,s}$	9	17	31	44	55	66	71	81	87	94

Table 4.2: Comparison of geometric and effective coverages for the ODG experiment with printed samples.

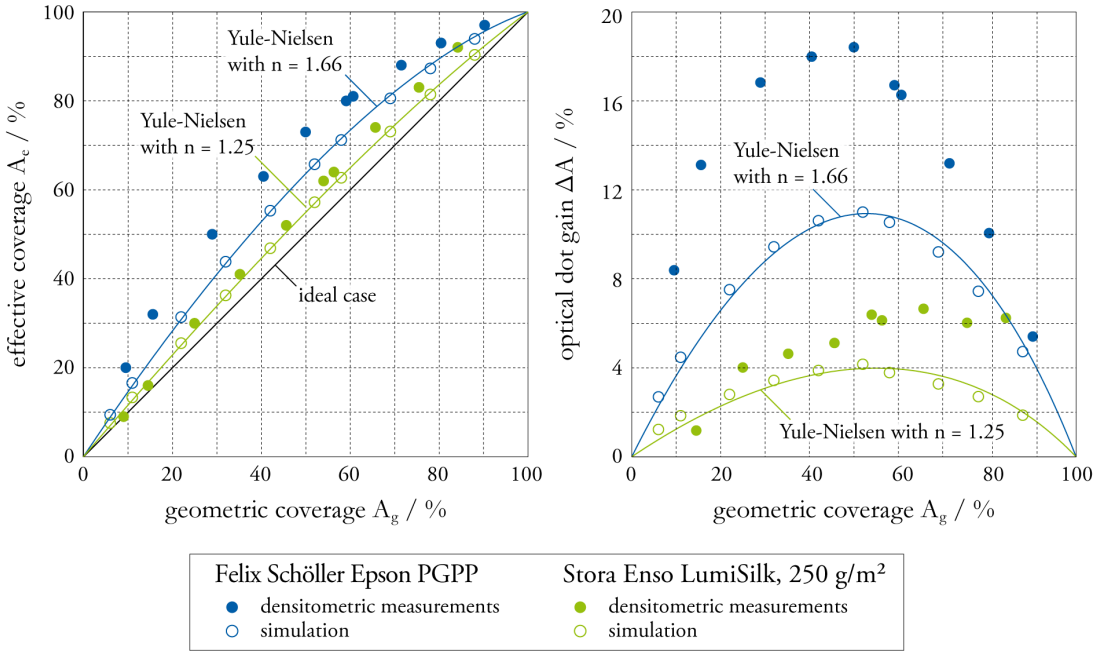

Figure 4.5: Results of the experiment with printed samples; tone response curves and ODG curves from densitometric measurement, dot gain simulation, and Yule-Nielsen approximations for Felix Schöller Epson Photo Paper and Stora Enso LumiSilk 250 g/m^2.

4.3 New Considerations on Optical Dot Gain

The results found in the previous investigations lead to the assumption, that there must be a simple connection between optical dot gain ΔA and parameters like the light scattering form parameter s, the reflectance of the paper R_p, the transmittance of the ink T_i, the screen frequency of the halftone f_s, and the geometrical coverage of the halftone A_g. Therefore, a parameter study was taken out, where the considered parameters were varied and their influence on ODG was analyzed. For all following calculations, light scattering was simulated using PSFs of EMG shape.

4.3.1 Parameter Spot Test

In a preliminary study, different parameters were investigated according to their impact on ODG. The parameters investigated were:

- screen frequency f_s
- light scatter form parameter s
- reflectance of paper R_p
- transmittance of ink T_i
- geometrical coverage of halftone A_g

For the evaluations, an AM screen was used. The ODG calculations were performed as described in section 4.1.1.

Since the investigated parameters open a 5-dim solution space, only a spot test could be performed. For each parameter, 3 to 4 representative values were chosen, where one value is close to the upper and lower limit for printing applications respectively, and at least one value lies approximately in the center of the covered interval. The chosen values can be found in table 4.3. For these parameters, ODG was calculated as described in section 4.1.2.

Parameter	**Symbol**	**Investigated Values**
screen frequency	f_s	40 l/cm, 80 l/cm, 160 l/cm
form parameter of light scattering	s	50 px, 100 px, 200 px, 300 px
reflectance of paper	R_p	0.6, 0.8, 0.95
transmittance of ink	T_i	0.01, 0.05, 0.1
geometrical coverage of halftone	A_g	10 %, 50 %, 90 %

Table 4.3: Investigated parameters for spot test on ODG.

Figure 4.6 shows the calculated ODG ΔA for the investigated parameters. Screen frequency, light scattering, transmittance of the ink, and fractional coverage of the halftone clearly influence the ODG, whereas the reflectance of paper does not show any effect. A closer investigation of the results for the three paper reflectances revealed that the differences of the simulated ODGs were less than 3×10^{-13} which can be interpreted as discretization errors only.

The results for screen frequency and light scattering were found to be directly coupled. Thus, a auxiliary variable *fs* for the product of screen frequency f_s and light scattering form parameter s was defined. When converting screen frequency (here in l/cm) and light scattering parameter (here in px) into conforming units using the conversion factor f_c (here in µm/px), the auxiliary variable *fs* gets dimensionless:

$$fs = f_s \cdot s \cdot f_c. \tag{4.8}$$

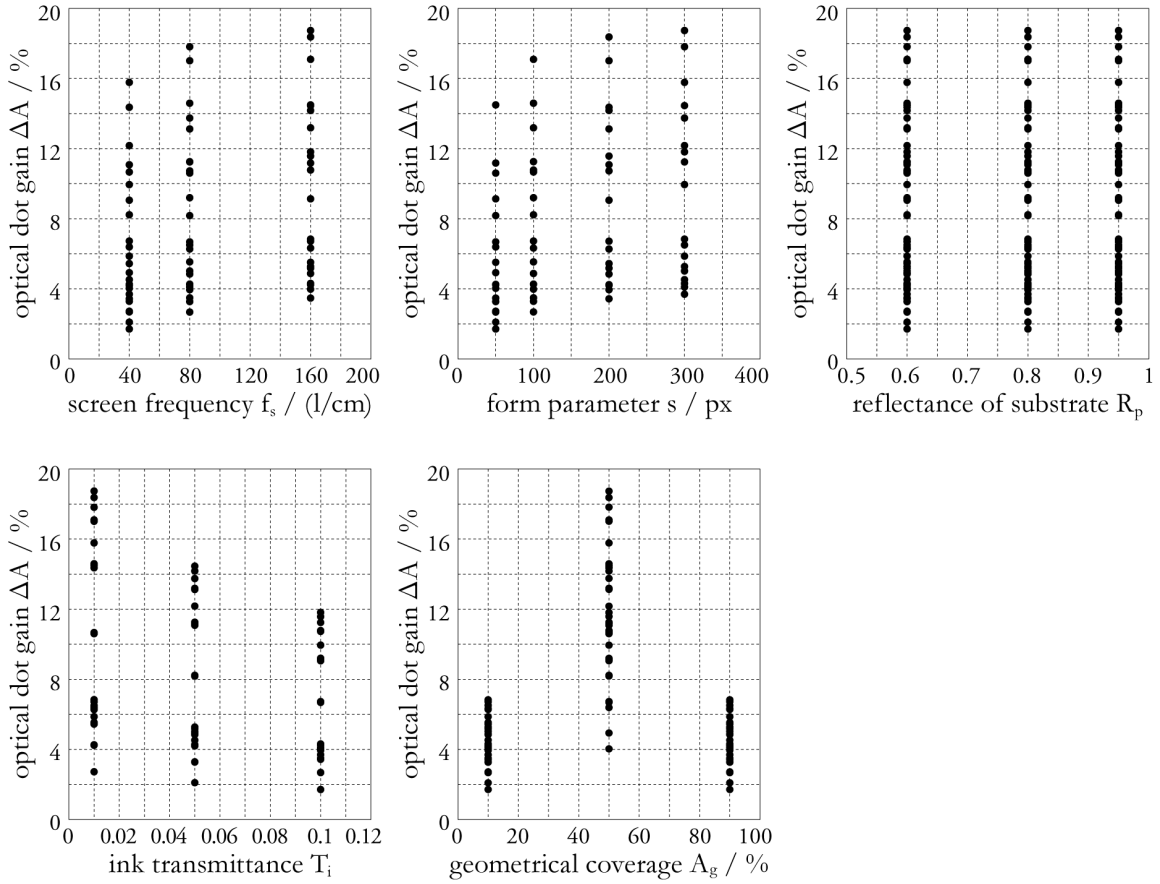

Figure 4.6: Results of the spot test of the different parameters and their influence on optical dot gain (ODG).

This way, the ODG parameter study could be reduced to three dimensions:

$$\Delta A = f\left(fs, T_i, A_g\right). \tag{4.9}$$

4.3.2 New Function for Optical Dot Gain

An extended parameter study was taken out to reveal functional relations of the three parameters with ODG. The parameters and their investigated values can be found in table 4.4. In this study, the screen frequency f_s was fixed with the constant value 160 l/cm and the auxiliary variable *fs* was varied by changing the light scattering form parameter s alone. Halftones up to 65 % were simulated with positive dots and halftones from 40 % upwards with negative dots. This created an overlap between 40 % and 65 %, where positive as well as negative screens were evaluated.

In Figure 4.7 the results of the extended parameter study are plotted against the three parameters. With increasing auxiliary variable *fs* the ODG grows. For high *fs* the different ODG curves approach an horizontal asymptote.

This behavior is reasonable if considering the leveling effect of light scattering. Figure 4.9 illustrates this effect with the help of the simulation model that was presented in section 4.1.2. The three rows show the light distributions after the first passing of the ink layer (I_1, left), after light scattering (I_2, center), and after the light passed the ink layer the second time (I_3, right). For the top row, zero light scattering was assumed (form parameter $s \to 0$). This equals infinitesimal screen frequency ($f_s \to 0$). In other words, if the light scattering is small compared to the distance between the dots, there will be no remarkable light transport and ODG will stay insignificantly small. The center row presents the effect that is most important for printing. Here, the auxiliary variable lies somewhere between zero and infinity ($0 < fs < 1$). Neither light scattering (s) nor screen frequency f_s are very small or very large. This way, changes in either screen frequency or light scattering form parameter effect ODG noticeable. For the last case, infinite light scattering or screen frequency result in a total leveling of the light distribution after light scattering. In other words, if the light scattering is very large compared to the distance of the dots, all differences in the light distribution will be completely evened to a constant light intensity. In this case,

Parameter	**Symbol**	**Investigated Values**
form parameter of light scattering	s	10 px, 20 px, 50 px, 100 px, 200 px, 500 px
transmittance of ink	T_i	0.01, 0.02, 0.05, 0.1, 0.2, 0.5
geometrical coverage of halftone	A_g	1 %, 5 %, 10 %, 15 %, ..., 85 %, 90 %, 95 %, 99 %

Table 4.4: Investigated parameters for extended parameter study on ODG.

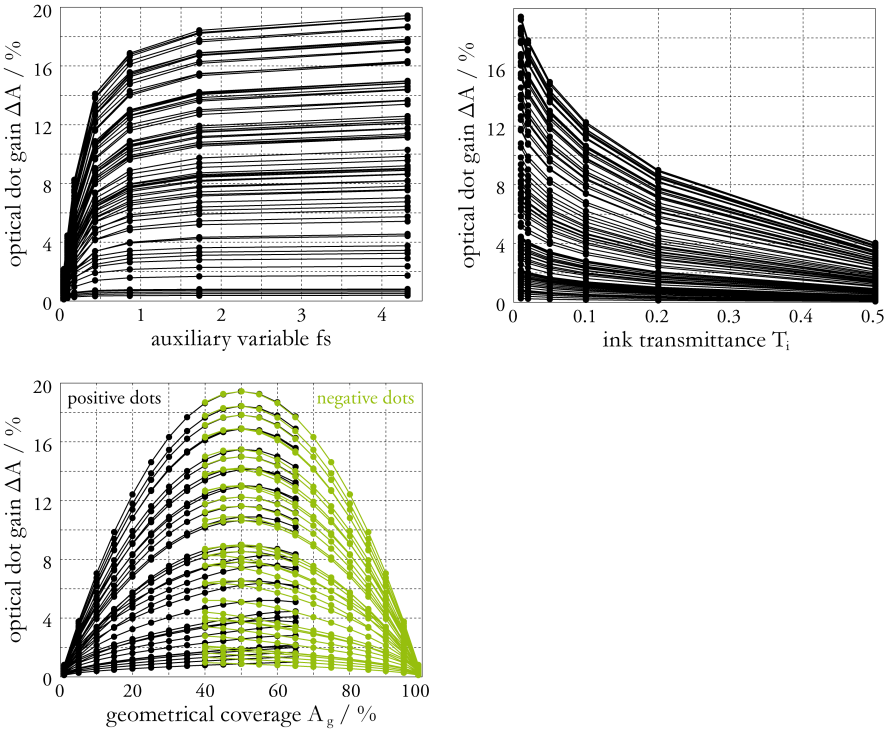

Figure 4.7: Results of the extended parameter study on optical dot gain (ODG).

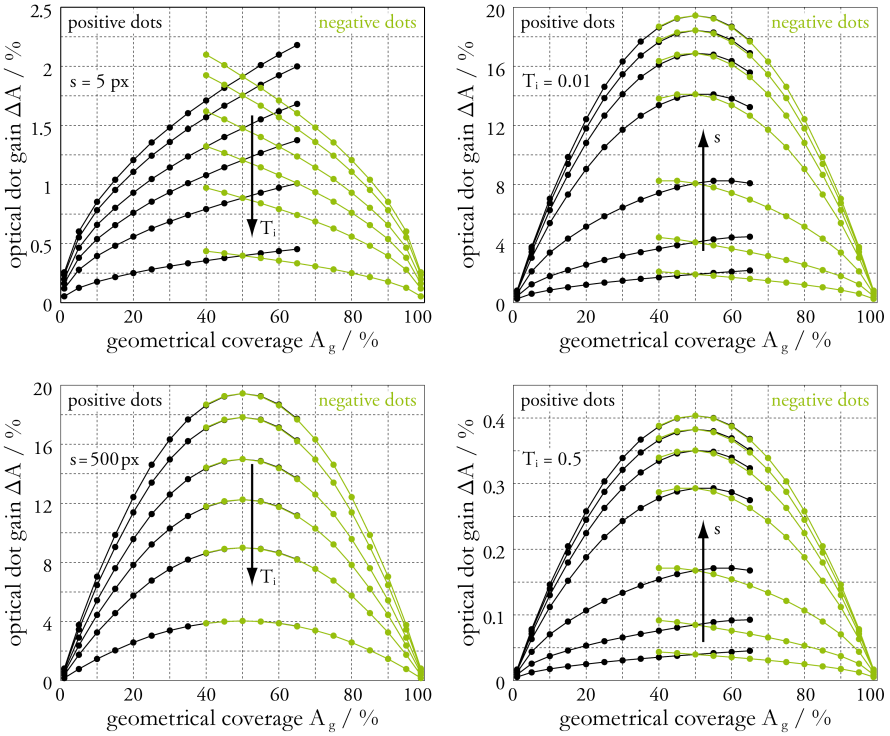

Figure 4.8: Details from the results of the extended parameter study on optical dot gain (ODG); selected curves for $s = 5$ px, $s = 500$ px, $T_i = 0.01$, and $T_i = 0.5$.

changes in screen frequency or light scattering form parameter will not have a noticeable effect. This is the horizontal asymptote in figure 4.7, top left.

The transmittance of the ink has an inverse effect. Increasing transmittance, i.e. increasing transparency of the ink reduces the optical dot gain. An explanation for this is, that with higher absorption of the ink, the less of the light that is "trapped" under the dots can come out again. Although the amount of light, that is transported from an unprinted location to a printed dot stays the same, less of it can pass the ink and come out. At the same time, the light that is transported from under the dots to unprinted locations is already weakened by the higher absorption when passing the ink layer and entering the paper.

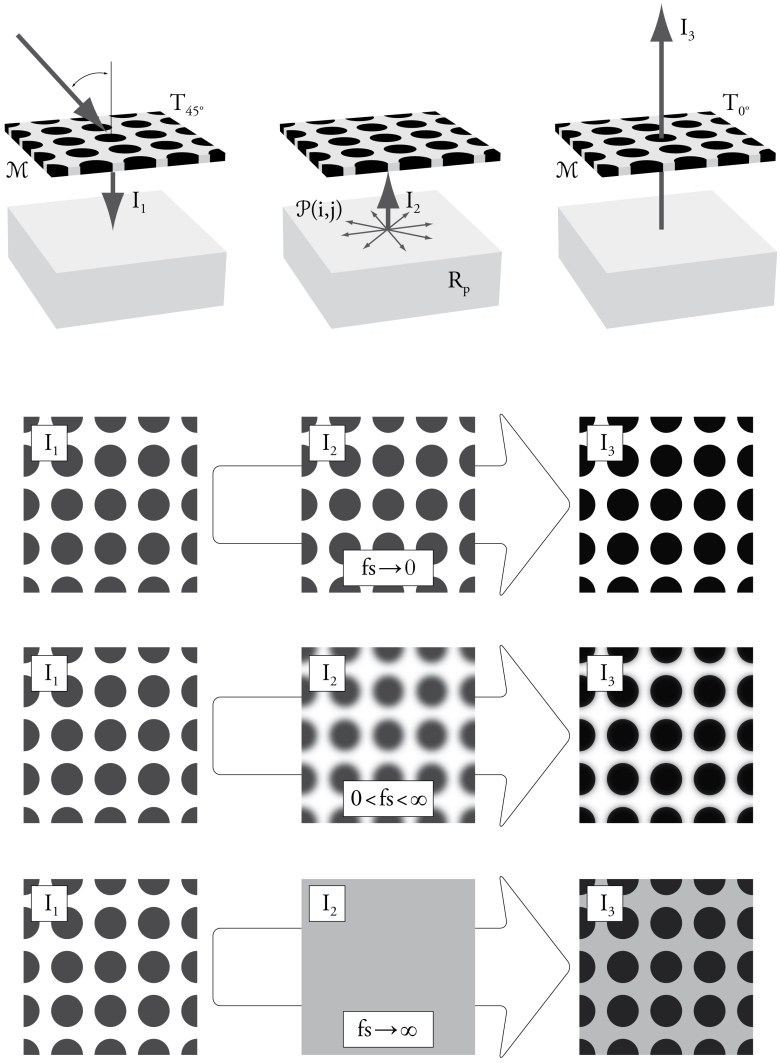

Figure 4.9: Leveling effect of light scattering. The lateral distribution of the light before it passes the ink layer the second time depends on the auxiliary variable of light scattering *fs*; top row: no light scattering and/or infinitesimal screen frequency, central row: medium light scattering and medium screen frequency, bottom row: infinite light scattering and/or infinite screen frequency.

The relation of ODG to fractional area coverage revealed some interesting facts. First, the maximum ODG is not always found for 50 %, but the location of maximum ODG travels to higher tonal values for lower auxiliary variables *fs*. This is valid for positive dots, the curves for negative dots were found to be mirror-inverted at 50 % fractional area coverage. The second fact is that the curves for positive and negative dots only meet for very high auxiliary variables *fs* and thus very pronounced ODG curves. For lower *fs* the point of transition between positive and negative dots can clearly influence the resulting ODG curve. This can be seen clearly in figure 4.8, where the curves for $s = 5$ px, $s = 500$ px, $T_i = 0.01$, and $T_i = 0.5$ are plotted. Obviously the ink transmittance has no influence on the shift of the location of maximum ODG.

An approximation for ODG that takes into account these relations was formulated by analyzing the different dependencies of the parameters that were found in the parameter study. For the auxiliary variable *fs*, the arc tangent function was postulated, while its horizontal asymptote was assumed to be a function of fractional area coverage A_g and transmittance of the ink T_i. The approach was as follows:

$$\begin{aligned} \Delta A &= a \cdot \arctan\left[b \cdot c\right] \text{ where} \\ a &= f(A_g, T_i), \\ b &= f(A_g, T_i), \\ c &= f(fs). \end{aligned} \tag{4.10}$$

Fitting the variables a, b, and c to the results of the parameter study, the following solution could be found:

$$\begin{aligned} \Delta A &= \left(A_g - A_g^2\right) \cdot \left(p_1 \cdot T_i^{p_2} + p_3\right) \cdot \arctan\left[f(A_g) \cdot fs\right] \text{ where} \\ f(A_g) &= \left(p_4 \cdot \exp\left(p_5 \cdot A_g\right) + p_6 \cdot A_g^2 + p_7 \cdot A_g + p_8\right). \end{aligned} \tag{4.11}$$

For negative dots, A_g has to be replaced by $1 - A_g$. The parameter p_1 to p_8 were fitted to the simulated results of the parameter study:

$$p = (-0.242 \quad 0.255 \quad 0.761 \quad 5.99 \quad -22.08 \quad 7.60 \quad -5.05 \quad 4.77). \tag{4.12}$$

The performance of the fit was evaluated in terms of absolute errors of the predicted with the simulated ODG. The mean absolute error was 0.11 %, where the percentage sign refers to ODG, which is usually given in percent. The median absolute error was calculated to 0.07 % and the maximum absolute error to 0.5 %.

Figure 4.10 shows, how ODG can be predicted by means of the derived function. Here, three different values for ink transmittance were chosen exemplarily. The y- and the x-axis are the auxiliary variable *fs* and geometrical area coverage A_g respectively. The z-axis indicates the ODG.

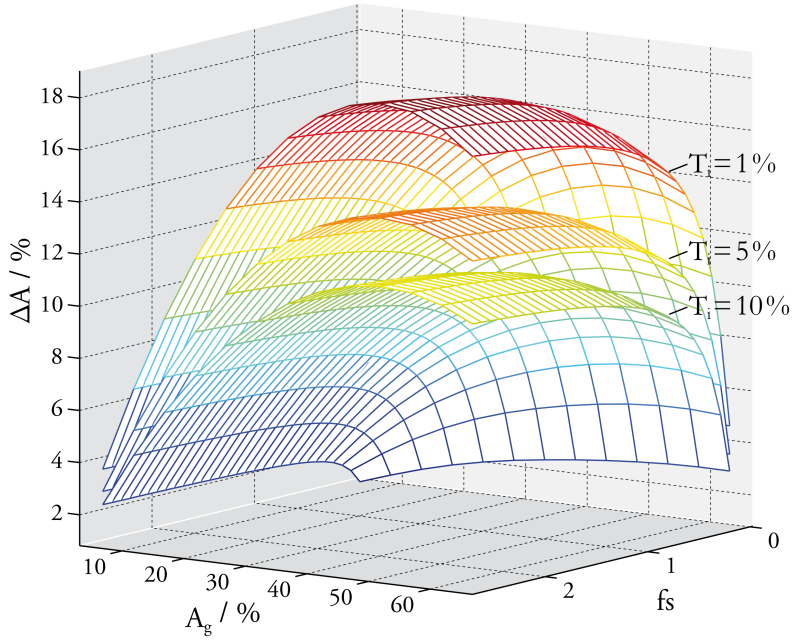

Figure 4.10: Prediction of ODG with empirical equation 4.12, shown for three different values for ink transmittance.

Without any further fitting, ODG can be calculated with very restricted information input; only the knowledge of screen frequency, light scatter parameter, and ink transmittance are required to predict ODG for any geometrical area coverage.

5

Conclusions

In the following sections, the main outcomes of this work will be summarized and discussed. For the summary (section 5.1), the facts will be stated without further explanation and the reasons, why these choices were made or why simplifications and necessary conditions were formulated. For detailed information, please be referred to the related chapters.

In section 5.2, the outcomes of this work are discussed. Unsolved challenges or assumptions on causing effects that could not be included into the main chapters will be stated here. These open up topics for future research.

5.1 Summary

The aim of this work was to introduce a measurement setup for light scattering in paper, to present representative measurement results, and to show possible applications for the prediction of printed halftones. In order to derive a suitable measurement setup, basic principles on light scattering, optical models, and printing were summarized in chapter 2.

A literature review of known measurement setups lead to a morphological analysis of principle measurement designs (section 3.1), which was the basis for the chosen measurement setup in this research:

- projection method
- light pattern: edge
- laterally resolved detection using CCD monochrome camera, 12 bit, 2 MP
- measurement geometry: 0°/0°
- spectral sensitivity reduced by using small-band LED as light source
- suppression of surface reflections by using polarizing filters for the sample measurements
- reduction of distortions of polarizing filters by leaving the analyzer in the light path for the first surface (FS) mirror reference capture

- enhanced focusing using FS mirror as focusing tool and Tenengrad focus measure
- angular scattering measurement by pivotable sample holder
- pixel resolution of 0.54 µm/px
- suppression of external straylight using black curtain
- internal straylight correction of reference ESF

It was found, that for the chosen setup, four images are necessary to obtain a complete measurement. The types of these images were gained from theoretical considerations, see section 3.2:

- reference (FS mirror), unmasked illumination (no edge) ($\boldsymbol{V}_{\mathrm{ref}}$)
- reference (FS mirror), masked illumination (edge) ($\boldsymbol{V}_{\mathcal{M},\mathrm{ref}}$)
- sample (paper), unmasked illumination (no edge) ($\boldsymbol{V}$)
- sample (paper), masked illumination (edge) ($\boldsymbol{V}_{\mathcal{M}}$)

The derived measurement equation describes the necessary processing of these images to a single measurement of an *edge spread function* (ESF). Additionally, some requisitions were formulated that have to be satisfied in order to apply this measurement equation correctly. These are:

1. The acquisition of the images of each specimen (sample or reference) with masked and unmasked illumination should be performed using the same exposure time.
2. The images of the reference (masked and unmasked) must be taken without polarizing filters, the sample images with polarizing filters.
3. Absorption and fluorescence in the sample must be negligible for the spectral distribution of the light source.
4. For each image, the capture must be repeated several times.
5. The edge must be well aligned along pixel direction.

In section 3.3, the measurement setup is presented in detail. An important improvement is the enhanced focusing that was realized using a focus measure and a FS mirror as focusing tool. Different focus measures were analyzed with respect to their applicability on the image motives, that have to be captured for one measurement. The best conditions were featured by the Tenengrad focus measure (TENG), which was used for all subsequent analyses and measurements.

The performance of the measurement setup was evaluated, investigating the following aspects:

- spectrum of the light source
- temperature and temporal noise
- focus
- image distortion

- polarizing filters
- stray light

If necessary, counter measures were presented and implemented to improve the performance.

With these adjustments, measurements on 33 papers were conducted (section 3.4). These measurements were analyzed according to the anisotropy of light scattering. It was found, that the anisotropy of papers is not significant compared to the lateral inhomogeneity of paper. Thus, measurements were averaged over all captured angles for all subsequent investigations.

The different types of papers formed three groups, here called the light scattering classes. As presented, a definition of such classes could be advantageous for printing applications, if paper producers included this information into their data sheets.

Even more information on the light scattering of a paper sample can be featured by its *line* or *point spread functions* (LSF, PSF). Thus, two approaches were presented to calculate the LSF and PSF from the measured ESF of one paper sample. The first approach was the fitting of empirical functions from literature to the measured ESFs. From the evaluated empirical functions, the modified exponential PSF according to Gustavson (EMG) was found to be the best description of the measurements. Also, the second approach using linear programming resulted in similar PSFs.

A spectral analysis using different LED spectra as illumination led to the conclusion, that light scattering depends on the light's wavelength. Nevertheless, the spectral differences for one paper were small compared to the differences between the papers, such that the spectral dependency was not investigated with more detail.

In chapter 4, the measurement results were applied to the prediction of *optical dot gain* (ODG) in monochrome halftones. Here, PSFs on the basis of the EMG empirical function were used. Spectral and angular influences on the scattering properties were neglected.

Since printing includes mechanisms, that increase the fractional area coverage but are not related to ODG, the first experiment of section 4.1 was designed in such a way that printing was not necessary using a halftone film. The measured fractional area coverages and the simulations on the basis of the measurements were compared. It could be shown that the simulations approximated the measured results. Although the tendencies coincide, the simulation was not a perfect match for the measurement.

The same result was found for a similar experiment using printed samples, see section 4.2. Again, the tendencies of simulation and measurement were the same. Nevertheless, the differences between simulation and measurement diverged even more for this experiment. It was concluded, that the main reasons for these deviations come from the different measurement geometries, imprecisions in the measurement of the area coverages, and – for the experiment with printed samples – from the inhomogeneous distribution of the ink layer thickness.

The last investigation (section 4.3) showed a new possibility from light scattering description using PSFs. A broad parameter study showed, that ODG only depends on the following parameter:

- the product of form parameter of light scattering and screen frequency
- the transmittance of ink
- the geometrical fractional area coverage of the halftone

Using these parameter, a prediction function was derived, which can be used to predict ODG without printing any patches.

5.2 Discussion

An outcome of this work is the morphological analysis of subfunctions of the measurement setup, presented in section 3.1. It allows to easily vary the setup design by choosing a different solution for a subfunction. Unfortunately, not every combination is feasible. Also, some solutions will not work on certain samples. An example for the latter is the use of polarizing filters, when the sample has a polarizing effect. This was found when evaluating white foils, like they are used for some printing applications. The stretch forming during the foils' production process is the reason, why these foils polarize light. This resulted in a strong anisotropy of the measurements, which was found to be caused only by polarization.

The 1D measurement equation 3.27, introduced in section 3.2 is based on several conditions. If the measurement setup does not fit these conditions, the application of the measurement equation might be afflicted with errors. One example is the constancy of the lateral light distribution, which was determined and adjusted for the measurement setup of this work, see figure 3.10. Nevertheless, there have been no investigations on the impact on the measurement performance, when this light distribution severely differs from conformity. This could be an aspect to be examined in future.

Introducing the enhanced focusing tools is an important improvement compared to previous setups. In literature, information on the way of focusing are missing. It can only be guessed, that in previous researches, the focus was adjusted manually and judged subjectively by the researcher. One of the enhancements is based on the sample holder. Here, the focusing of the rough sample is replaced by focusing the smooth FS mirror and then just swivel in the sample. The second enhancement is the focus measure, which helps to judge the quality of focus objectively. It is also the first step to an auto-focus for future measurement setups. Nevertheless, the chosen Tenengrad (TENG) focus measure depends on the general light intensity of the illumination. When the LED got brighter, the focus measure increased without changing the focus – which was a challenge to ignore when focusing. This drawback could be solved by either decouple the TENG focus measure from the light intensity or by enhancing the stability of the light source, here the LED.

The measurement results presented in section 3.4 still open up some questions. The lack of anisotropy in the papers was astonishing in first place – which was even found for uncoated papers. Nevertheless, this can be explained by the large region that is used when averaging the pixel rows. This way, the influence of the single fiber decreases. An interesting approach might be to find materials, where the anisotropy of light scattering is already known. Then it could be investigated, if the isotropy of light scattering is really caused by material properties or if there are other reasons that hide the anisotropy behind measurement errors.

A second interesting fact was, that the light scattering properties of the coated fine art papers did not follow systematic rules. For some paper series, the light scattering increased with increasing grammage, for some series they decreased. At the same time, the differences between the investigated paper series were surprisingly small. The reason for this might be, that the fillers used in the coatings are very similar for all papers. Again, a research on defined and well characterized samples might be interesting. Then, the research could also include fluorescence as a new aspect.

Although in literature, the spectral dependency on light scatter is also described as low [46, 94], it would be interesting to verify this finding with other experiments. Measurements with monochromatic illumination could deliver new insight.

As seen in chapter 4, the application of the measurement results to printed AM halftones is not very satisfying, yet. Although for some samples, the prediction of ODG is acceptable, samples with pronounced light scattering (i.e. opal glass and Felix Schöller Epson PGPP) were not approximated very well. There might be several reasons for this mismatch, as they were already mentioned before. Among measurement geometry and incorrect detection of the geometrical area coverages, the insufficient measurement accuracy of the ink transmittance is assumed to be an important factor. Additionally, the incorporation of an ink thickness distribution instead of a constant ink thickness for each dot could provide the essential improvement for the prediction model – similar to the approach presented by Emmel and Hersch [44]. A second improvement on the prediction model would be to incorporate light scattering in the ink, which is up to now assumed to be a perfect filter with only absorption. Here, the Kubelka-Munk model could be used.

Since the prediction was only tested on AM screens, the applicability on FM screens is not verified, yet.

However, there is also a new possible application of the presented model. Since the determination of the geometrical area coverage of halftones is still afflicted with uncertainties in the state of the art measurement procedures, the inverse effect of light scattering could be used to enhance this prediction. If light scattering of the paper is known, the detected image of a halftone could be deconvoluted by the PSF in order to derive the image without ODG. And from this, the geometrical area coverage could be calculated.

5.3 Scientific Added Value

This work presents the necessary means to design a measurement setup for the measurement of light scattering in paper or other substrates.

The main enhancements of the derived measurement setup are the advanced focusing tools, the investigation of the sources of possible measurement errors, and the angular resolved measurement to detect anisotropy.

For AM screens it was shown that with the representation of light scattering using a PSF, the optical dot gain can be predicted without printing any patches. Only one parameter, the form parameter s of the PSF, is necessary to describe light scattering, and the ink transmittance and screen frequency have to be known.

A prerequisite of this optical dot gain prediction is an accurate and reliable measurement of the form parameter s for light scattering. The measurement setup presented in this work offers the possibility of such a measurement.

This way, this work is a contribution to improve first principle printer models by decoupling optical dot gain and other physical dot gain sources like ink spread.

References

[1] Kathrin Happel, Marius Walter, Philipp Urban, and Edgar Dörsam. Measuring Anisotropic Light Scatter within Graphic Arts Papers For Modeling Optical Dot Gain. In *Color and Imaging Conference, San Antonio, Texas*, pp. 347–352. IS&T/SID, 2010.

[2] David R. Wyble and Roy S. Berns. A critical review of spectral models applied to binary color printing. *Color Research and Application*, 25:4–19, 2000.

[3] Helmut Kipphan. *Handbook of Print Media : Technologies and Production Methods*. Springer, Berlin, 2000.

[4] Paul Kubelka and Franz Munk. Ein Beitrag zur Optik der Farbanstriche. *Zeitschrift für technische Physik*, 11a:593–601, 1931.

[5] Hans G. Völz. *Industrial Color Testing – Fundamentals and Techniques*. Wiley-VCH, Weinheim, 2001.

[6] Felix Berg. *Isotrope Lichtstreuung in Papier - Neue Überlegungen zur Kubelka-Munk-Theorie*. PhD thesis, Technische Hochschule Darmstadt, Darmstadt, Germany, 1997. <http://tubiblio.ulb.tu-darmstadt.de/903/>

[7] Safer Mourad. *Color predicting model for electrophotographic prints on common office paper*. PhD thesis, École Polytechnique Fédérale de Lausanne, Lausanne, Switzerland, 2003. <http://library.epfl.ch/theses/?nr=2708>

[8] Edgar Dörsam. *Farbwiedergabe in den Medien*. Technische Universität Darmstadt, Institute of Printing Science and Technology, WS 2010/11. Lecture notes. <http://www.idd.tu-darmstadt.de/studium_lehre/vorlesungen_2/fim/fim_ws_2010_11/>

[9] Günther Wyszecki and Walter Stanley Stiles. *Color science : concepts and methods, quantitative data and formulae*. Wiley-Interscience, New York, 2000.

[10] Ludwig Bergmann, Clemens Schaefer, and Heinz Niedrig. *Lehrbuch der Experimentalphysik Bd. 3 - Optik : Wellen- und Teilchenoptik*. de Gruyter, Berlin, 2004.

[11] Edgar Dörsam. *Farbwiedergabe in den Medien*. Technische Universität Darmstadt, Institute of Printing Science and Technology, WS 2008/09. Lecture notes.

[12] Gustav Mie. Beiträge zur Optik trüber Medien, speziell kolloidaler Metallösungen. *Annalen der Physik*, 330(3):377–445, 1908. <http://dx.doi.org/10.1002/andp.19083300302>

[13] Gustav Mie. *Contributions to the optics of turbid media, particularly of colloidal metal solutions*, 1976.

[14] *Rayleigh- versus Mie- Scattering*. Radartutorial.eu. Online, 2011. <http://www.radartutorial.eu/18.explanations/ex22.en.html> [cited April 20, 2011]

[15] A. Ishimaru. Theory and application of wave propagation and scattering in random media. *Proceedings of the IEEE*, 65(7):1030 – 1061, 1977.

[16] Georg A. Klein. *Farbenphysik für industrielle Anwendungen*. Springer, Berlin, 2004.

[17] J.S. Arney, Jim Chauvin, Josh Nauman, and Peter G. Anderson. Kubelka-Munk Theory and the MTF of Paper. *Journal of Imaging Science and Technology*, 47(4):339–345, 2003.

[18] Erich W. Marchand. Derivation of the Point Spread Function from the Line Spread Function. *Journal of the Optical Society of America*, 54(7):915–919, 1964. <http://www.opticsinfobase.org/abstract.cfm?URI=josa-54-7-915>

[19] Erich W. Marchand. From Line to Point Spread Function: The General Case. *Journal of the Optical Society of America*, 55(4):352–352, 1965. <http://www.opticsinfobase.org/abstract.cfm?URI=josa-55-4-352>

[20] Glenn D. Boreman. *Modulation transfer function in optical and electro-optical systems*. Tutorial texts in optical engineering ; v. TT 52. SPIE Press, Bellingham, Wash, 2001.

[21] J.S. Arney, P.G. Engeldrum, C.D. Arney, and M. Katsube. An MTF Analysis of Paper. *Journal of Imaging Science and Technology*, 40:19–25, 1996.

[22] Deane Brewster Judd. Terms, Definitions, and Symbols in Reflectometry. *Journal of the Optical Society of America*, 57(4):445–450, 1967. <http://www.opticsinfobase.org/abstract.cfm?URI=josa-57-4-445>

[23] Heike Hupp. *Qualitäts- und Prozesskontrolle gedruckter Interferenzeffektfarben erster Generation.* PhD thesis, Technische Universität Darmstadt, Darmstadt, Germany, 2008. <http://tubiblio.ulb.tu-darmstadt.de/38480/>

[24] Katharina Kehren, Edgar Dörsam, and Heike Hupp. Printed interference effect colours - process control and quality assurance. In *36th International Research Conference of Iarigai*, pp. 329–336, 2009. <http://tubiblio.ulb.tu-darmstadt.de/41298/>

[25] F. E. Nicodemus, J. C. Richmond, J. J. Hsia, I. W. Ginsberg, and T. Limperis. Geometrical considerations and nomenclature for reflectance. *Science And Technology*, 160:1–52, 1977. <http://www.mendeley.com/research/geometric-considerations-and-nomenclature-for-reflectance>

[26] Andreas Höpe and Kai-Olaf Hauer. Three-dimensional appearance characterization of diffuse standard reflection materials. *Metrologia*, 47(3):295, 2010. <http://stacks.iop.org/0026-1394/47/i=3/a=021>

[27] *Strahlungsphysikalische und lichttechnische Eigenschaften von Materialien – Teil 3: Meßverfahren für lichttechnische und spektrale strahlungsphysikalische Kennzahlen.* DIN 5036-3, German Standard, DIN, 1979.

[28] Arne Valberg. *Light Vision Color.* John Wiley & Sons, Chichester, 2005.

[29] *Farbmessung – Teil 1: Grundbegriffe der Farbmetrik.* EN DIN 5033-1:2008, German Standard, EN DIN, 2008.

[30] Edgar Dörsam. *Praktische Farbmessung.* Technische Universität Darmstadt, Institute of Printing Science and Technology, SS 2010. Lecture notes. <http://www.idd.tu-darmstadt.de/studium_lehre/vorlesungen_2/prfm/prfm_ss_2010/>

[31] *Colorimetry – Part 1: CIE standard colorimetric observers.* ISO 11664-1:2007, International Standard, CIE, 2007.

[32] Roy S. Berns. *Billmeyer and Saltzmann's Principles of Color Technology.* John Wiley & Sons, New York, 2000.

[33] D Tollenaar and P Ernst. Optical Density and Ink Layer Thickness. In *Proceedings of the Sixth International Conference of Printing Research Institutes (1961 IARIGAI Proceedings)*, pp. 214–234., New York, 1961. Pergamon Press.

[34] *Prüfung von Drucken und Druckfarben der Drucktechnik – Farbdichtemessungen an Drucken – Teil 2: Anforderungen an die Messanordnung von Farbdichtemessgeräten und ihre Prüfung.* DIN 16536-2:1995, German Standard, DIN, 1995.

[35] T. Celio, F. Mast, and H. Ott. The Use of Polarizing Filters in the Measurement of Optical Reflection Density. *Journal Of Imaging Technology*, 17, 1991.

[36] *Colorimetry*. CIE 15:2004, International Standard, CIE, 2004.

[37] Edgar Dörsam. *Konstruktionsprinzipien im Druckmaschinenbau*. Technische Universität Darmstadt, Institute of Printing Science and Technology, WS 2010/11. Lecture notes. <http://www.idd.tu-darmstadt.de/studium_lehre/vorlesungen_2/kid/kid_ws_2010_10/>

[38] Arnold Opherden et al. *Zellstoff Papier*. VRB Fachbuchverlag, Leipzig, 1976.

[39] *Fiber crop*. Wikimedia Foundation, Inc. Online, May 2011. <http://en.wikipedia.org/wiki/fiber_crop> [cited May 9, 2011]

[40] J.H. Bos and Martin Staberock. *Das Papierbuch : Handbuch der Papierherstellung*. ECA Pulp & Paper, Houten, 2006.

[41] Samuel Schabel. *Einführung in die Papierfabrikation*. Technische Universität Darmstadt, Chair of Paper Technology and Mechanical Process Engineering, WS 2010/11. Lecture notes.

[42] Walter Steiger, Gilbert Küffer, and Andreas Stock. Rauigkeit als vernachlässigte Einflussgrösse der Druckqualität. Technical report, Ugra, 2004. Ugra-Mitteilungen, pp. 34–37.

[43] J. A. C. Yule and W. J. Nielsen. The Penetration of Light into Paper and its Effect on Halftone Reproduction. In *Proceedings of the 3rd Annual Technical Meeting, TAGA*, pp. 65–76, 1951.

[44] Patrick Emmel and Roger David Hersch. A Unified model for color prediction of halftoned prints. *Journal of Imaging Science and Technology*, 44(4):351–359, 2000.

[45] A. Murray. A monochrome reproduction in photoengraving. *Journal of the Franklin Institute*, 221:721–744, 1936.

[46] Christiane Ackermann, Hermann Praast, and Lothar Göttsching. *Einfluss von Lichtstreuung und Lichtabsorption auf die Bildwiedergabe gedruckter Rasterflächen*. AiF-Schlussbericht, AiF-Nr. 12395N, 2002.

[47] J.A.C. Yule, D.J. Howe, and J.H. Altman. The Effect of the Spread-Function of Paper on Halftone Reproduction. *TAPPI Journal 50*, 7:337 – 344, 1967.

[48] Hiromu Wakeshima and Tatsuo Kunishi. Light Scattering in Paper and Its Effect on Halftone Reproduction. *Journal of the Optical Society of America*, 58:272–273, 1968.

[49] Peter G. Engeldrum and Brian Pridham. Application of Turbid Medium Theory to Paper Spread Function Measurements. *TAGA Proceedings*, 1:339–352, 1995.

[50] Shinichi Inoue, Norimichi Tsumura, and Yoichi Miyake. Measuring MTF of Paper by Sinusoidal Test Pattern Projection. *Journal of Imaging Science and Technology*, 41(6):657–661, 1997.

[51] Geoffrey L. Rogers. Measurement of the modulation transfer function of paper. *Applied Optics*, 37(31):7235–7240, 1998.

[52] Masayuki Ukishima, H. Kaneko, T. Nakaguchi, N. Tsumura, M. Hauta-Kasari, J. Parkkinen, and Y. Miyake. A Simple Method to Measure MTF of Paper and its Application for Dot Gain Analysis. *IEICE Transactions on Fondamentals of Electronics, Communications and Computer Sciences*, 12:3328–3335, 2009.

[53] *Sinusoidal Precision Sine Test Array*. Applied Image, Inc. Online, 2011. <http://www.aig-imaging.com/Sinusoidal-MTF-Optical-Test-Chart.html> [cited July 3, 2011]

[54] Nils Bornemann. *Personal Conversation*, March 2011.

[55] Ferran Laguart Bertran, Roger Artigas Pursals, and Cristina Cadevall Artigues. *Dual technology optical profilometer*. US000007636167B2. Patent, December 2009.

[56] *MatlabCentral*. The MathWorks, Inc. Online, 2011. <http://www.mathworks.com/matlabcentral/> [cited April 12, 2011]

[57] F.R. Ruckdeschel and O.G. Hauser. Yule-Nielsen effect in printing: a physical analysis. *Applied Optics*, 17:3376–3383, 1978.

[58] Gerhard Fischer, Jorge Rodriguez-Giles, and Karl R. Scheuter. Ein physikalisches Modell für die Beschreibung von Lichtstreuprozessen. *Die Farbe*, 30:199–220, 1982.

[59] Philipp Urban. *Personal Conversation*, July 2010.

[60] Marius Walter. Methode zur Messung orthotroper Lichtstreuung in grafischen Papieren. Master's thesis, Technische Universität Darmstadt, 2009.

[61] Ernst Leitz GmbH, Wetzlar. *ORTHOPLAN – Universelles Großfeldmikroskop*. Manual, Wetzlar, 1972.

[62] Ernst Leitz GmbH, Wetzlar. *PLOEMOPAK 2.1 u. 2.2 Fluoreszenz-Auflichtilluminator*. Manual, Wetzlar, 1974.

[63] Basler Vision Technologies. *Basler scA1600-14gm Camera Specification – Measurement protocol using the EMVA Standard 1288*. Manual, 2007.

[64] *Metallic Mirror Coatings*. Edmund Optics, Inc. Online, 2011. <http://www.edmundoptics.com/technical-support/optics/metallic-mirror-coatings/?&viewall> [cited July 2, 2011]

[65] Lumileds Lighting. *Technical Datasheet DS23 – Power Light Source Luxeon Star*. Manual, 2005.

[66] European Commission, Joint Research Center, Institute for Reference Materials and Measurements. *Certified Reference Material BCR - 406*. Certificate of Analysis, 2007.

[67] D. Hünerhoff, U. Grusemann, and Andreas Höpe. New robot-based gonioreflectometer for measuring spectral diffuse reflection. *Metrologia*, 43(2):S11, 2006. <http://stacks.iop.org/0026-1394/43/i=2/a=S03>

[68] David R. Caprette. *Measurement with the Light Microscope*. Rice University. Online, May 2005. <http://www.ruf.rice.edu/~bioslabs/methods/microscopy/measuring.html> [cited March 21, 2011]

[69] *Stage Micrometers*. POG Präzisionsoptik Gera GmbH. Online, 2008. <http://www.pog.eu/en/products_ms_08.html> [cited March 21, 2011]

[70] Christian Gerthsen and Dieter Meschede. *Gerthsen Physik*. Springer, Berlin, 2002.

[71] Michael J. Nasse and Jörg C. Woehl. Realistic modeling of the illumination point spread function in confocal scanning optical microscopy. *Journal of the Optical Society of America A*, 27(2):295–302, 2010. <http://josaa.osa.org/abstract.cfm?URI=josaa-27-2-295>

[72] Eric Krotkov. Focusing. *International Journal of Computer Vision*, 1:223–237, 1988. <http://dx.doi.org/10.1007/BF00127822>

[73] Murali Subbarao, Tae Choi, and Arman Nikzad. Focusing Techniques. *Optical Engineering*, 32(11):2824–2836, 1993. <http://dx.doi.org/10.1117/12.147706>

[74] A. M. Eskicioglu and P. S. Fisher. Image quality measures and their performance. *IEEE Transactions on Communications*, 43(12):2959–2965, 1995. <http://dx.doi.org/10.1109/26.477498>

[75] L Firestone, K Cook, K Culp, N Talsania, and K Preston. Comparison of autofocus methods for automated microscopy. *Cytometry*, 12(3):195–206, 1991. <http://www.ncbi.nlm.nih.gov/pubmed/2036914>

[76] Jan-Mark Geusebroek, Frans Cornelissen, Arnold W. M. Smeulders, and Hugo Geerts. Robust autofocusing in microscopy. *Cytometry*, 39(1):1–9, 2000. <http://dx.doi.org/10.1002/(SICI)1097-0320(20000101)39:1<1::AID-CYTO2>3.0.CO;2-J>

[77] F. S. Helmli and S. Scherer. Adaptive shape from focus with an error estimation in light microscopy. In *Proceedings of the 2nd International Symposium on Image and Signal Processing and Analysis ISPA 2001*, pp. 188–193, 2001. <http://dx.doi.org/10.1109/ISPA.2001.938626>

[78] Eric Krotkov and J.-P. Martin. Range from focus. In *Proceedings of IEEE International Conference on Robotics and Automation*, Vol. 3, pp. 1093–1098, 1986. <http://dx.doi.org/10.1109/ROBOT.1986.1087510>

[79] Sang-Yong Lee, Jae-Tack Yoo, Y. Kumar, and Soo-Won Kim. Reduced Energy-Ratio Measure for Robust Autofocusing in Digital Camera. *IEEE Signal Processing Letters*, 16(2):133–136, 2009. <http://dx.doi.org/10.1109/LSP.2008.2008938>

[80] Rashid Minhas, Abdul Mohammed, Q. Wu, and Maher Sid-Ahmed. 3D Shape from Focus and Depth Map Computation Using Steerable Filters. In Mohamed Kamel and Aurelio Campilho, editors, *Image Analysis and Recognition*, Vol. 5627 of *Lecture Notes in Computer Science*, pp. 573–583. Springer Berlin / Heidelberg, 2009. <http://dx.doi.org/10.1007/978-3-642-02611-9_57>

[81] Harsh Nanda and Ross Cutler. Practical calibrations for a real-time digital omnidirectional camera. Technical report, In Technical Sketches, Computer Vision and Pattern Recognition, 2001.

[82] Shree Nayar. Shape from Focus. Technical report, Carnegie Mellon University, 1989.

[83] J. L. Pech-Pacheco, G. Cristóbal, J. Chamorro-Martínez, and J. Fernández-Valdivia. Diatom Autofocusing in Brightfield Microscopy: a Comparative Study. *Pattern Recognition, International Conference on*, 3:3318, 2000. <http://dx.doi.org/10.1109/ICPR.2000.903548>

[84] A. Santos, C. Ortiz de Solórzano, J. J. Vaquero, J. M. Pena, N. Malpica, and F. del Pozo. Evaluation of autofocus functions in molecular cytogenetic analysis. *Journal of Microscopy*, 188(3):264–272, 1997. <http://dx.doi.org/10.1046/j.1365-2818.1997.2630819.x>

[85] Chun-Hung Shen and H. H. Chen. Robust focus measure for low-contrast images. In *Digest of Technical Papers of the International Conference on Consumer Electronics (ICCE)*, pp. 69–70, 2006. <http://dx.doi.org/10.1109/ICCE.2006.1598314>

[86] M. V. Shirvaikar. An optimal measure for camera focus and exposure. In *Proceedings of the Thirty-Sixth Southeastern Symposium on System Theory*, pp. 472–475, 2004. <http://dx.doi.org/10.1109/SSST.2004.1295702>

[87] A. Thelen, S. Frey, S. Hirsch, and P. Hering. Improvements in Shape-From-Focus for Holographic Reconstructions With Regard to Focus Operators, Neighborhood-Size, and Height Value Interpolation. *IEEE Transactions on Image Processing*, 18(1):151–157, 2009. <http://dx.doi.org/10.1109/TIP.2008.2007049>

[88] Hui Xie, Weibin Rong, and Lining Sun. Wavelet-Based Focus Measure and 3-D Surface Reconstruction Method for Microscopy Images. In *Proceedings of IEEE/RSJ International Intelligent Robots and Systems Conference*, pp. 229–234, 2006. <http://dx.doi.org/10.1109/IROS.2006.282641>

[89] Ge Yang and B. J. Nelson. Wavelet-based autofocusing and unsupervised segmentation of microscopic images. In *Proceedings of IEEE/RSJ International Conference on Intelligent Robots and Systems (IROS 2003)*, Vol. 3, pp. 2143–2148, 2003. <http://dx.doi.org/10.1109/IROS.2003.1249188>

[90] Said Pertuz. *Focus Measure*. The MathWorks, Inc. Online, April 2010. <http://www.mathworks.com/matlabcentral/fileexchange/27314-focus-measure> [cited March 29, 2011]

[91] Kathrin Happel, Philipp Urban, Edgar Dörsam, and Xaver Ludewig. Classifying Papers According to Their Light Scatter Properties. In *Midterm Meeting of the International Colour Association (AIC), Zürich, Switzerland*, pp. 138–141. AIC, 2011.

[92] Gottfried Schröder and Hanskarl Treiber. *Technische Optik : Grundlagen und Anwendungen*. Vogel, Würzburg, 2002.

[93] Daniel Nyström. *High Resolution Analysis of Halftone Prints - A Colorimetric and Multispectral Study*. PhD thesis, Linköping University, Linköping, Sweden, 2008.

[94] Masayuki Ukishima. *Prediction and Evaluation of Color Halftone Print Quality Based on Microscopic Measurement*. PhD thesis, University of Eastern Finland, 2010.

[95] Stefan Gustavson. *Dot gain in colour halftones*. PhD thesis, Linköping University, Linköping, Sweden, 1997.

Appendix A

Mathematical Appendix

A.1 Convolution

A.1.1 Convolution of 1D Functions

The convolution of two continuous functions $A(x)$ and $B(x)$ is defined as:

$$\begin{aligned}(A * B)(x) &= \int_{-\infty}^{\infty} A(\xi)B(x-\xi)\,\mathrm{d}\xi \\ &= \int_{-\infty}^{\infty} A(x-\xi)B(\xi)\,\mathrm{d}\xi\end{aligned} \tag{A.1}$$

where $*$ is the convolution operator and the variable ξ allows the two functions to shift, passing each other. The discrete form of the convolution for the functions $A(i)$ and $B(i)$ is:

$$\begin{aligned}(A * B)(i) &= \sum_{\iota} A(\iota)B(i-\iota) \\ &= \sum_{\iota} A(i-\iota)B(\iota)\end{aligned} \tag{A.2}$$

A.1.2 Convolution of 2D Functions

When the considered functions $A(x, y)$ and $B(x, y)$ depend on two variables, the convolution is defined as:

$$\begin{aligned}(A * B)(x, y) &= \int_{-\infty}^{\infty}\int_{-\infty}^{\infty} A(\xi, \upsilon)B(x-\xi, y-\upsilon)\,\mathrm{d}\xi\,\mathrm{d}\upsilon \\ &= \int_{-\infty}^{\infty}\int_{-\infty}^{\infty} A(x-\xi, y-\upsilon)B(\xi, \upsilon)\,\mathrm{d}\xi\,\mathrm{d}\upsilon\end{aligned} \tag{A.3}$$

The corresponding discrete convolution of $A(i, j)$ and $B(i, j)$ is:

$$\begin{aligned}(A * B)(i, j) &= \sum_{\kappa}\sum_{\iota} A(\iota, \kappa)B(i-\iota, j-\kappa) \\ &= \sum_{\kappa}\sum_{\iota} A(i-\iota, j-\kappa)B(\iota, \kappa)\end{aligned} \tag{A.4}$$

A.1.3 Convolution Theorem

The convolution theorem states, that the convolution of two functions is the pointwise product of their Fourier transforms $\mathcal{F}$:

$$\mathcal{F}[A * B] = \mathcal{F}[A] \cdot \mathcal{F}[B] \tag{A.5}$$

Thus, a deconvolution can be performed by dividing the fourier transform of the convoluted functions by the fourier transform of one single function and perform the inverse Fourier transform $\mathcal{F}^{-1}$:

$$A = \mathcal{F}^{-1}\left[\frac{\mathcal{F}[A * B]}{\mathcal{F}[B]}\right] \tag{A.6}$$

A.2 Transformation Equations of PSF, LSF, and ESF

The equations presented here rely on the transformation equations derived by Marchand [18, 19]. They are valid only for isotropic scattering. This means, that the polar formulation of the PSF $\mathcal{P}(r, \phi)$ depends only on the radius r and not on the angle ϕ:

$$\mathcal{P}(r, \phi) = \mathcal{P}(r). \tag{A.7}$$

Starting from this assumption, the following equations can be formulated:

$$\mathcal{L}(x) = 2 \cdot \int_x^\infty \mathcal{P}(r) \frac{r}{\sqrt{r^2 - x^2}} \, \mathrm{d}r \tag{A.8}$$

$$\mathcal{P}(r) = -\frac{1}{\pi} \int_r^\infty \frac{\mathcal{L}'(x)}{\sqrt{x^2 - r^2}} \, \mathrm{d}x \tag{A.9}$$

$$\mathcal{E}(x) = \int_{-\infty}^x \mathcal{L}(u) \, \mathrm{d}u \tag{A.10}$$

$$\mathcal{L}(x) = \frac{\mathrm{d}}{\mathrm{d}x} \mathcal{E}(x). \tag{A.11}$$

They will be derived in the following paragraphs. Additional assumptions are that absorption α and surface reflection ρ can be neglected. Additionally, the medium is assumed to be optically thick, so that transmittance T can be disregarded, too.

$$\alpha = 0, \quad \rho = 0, \quad T = 0$$

In this case, the law of energy conservation constitutes that all energy incident on the surface (irradiance E), must be emitted again (exitance M).

$$\int_{-\infty}^\infty \int_{-\infty}^\infty M(x, y) \, \mathrm{d}x \, \mathrm{d}y = \int_{-\infty}^\infty \int_{-\infty}^\infty E(x, y) \, \mathrm{d}x \, \mathrm{d}y \tag{A.12}$$

The lateral distribution of the exitance E is given by the convolution of the irradiance M and the PSF $\mathcal{P}$:

$$\boxed{M(x, y) = (E * \mathcal{P})(x, y)} \tag{A.13}$$

With equation A.13, equation A.12 can be written as:

$$\int_{-\infty}^\infty \int_{-\infty}^\infty (E * \mathcal{P})(x, y) \, \mathrm{d}x \, \mathrm{d}y = \int_{-\infty}^\infty \int_{-\infty}^\infty E(x, y) \, \mathrm{d}x \, \mathrm{d}y \tag{A.14}$$

This can only be valid if

$$\int_{-\infty}^{\infty}\int_{-\infty}^{\infty}\mathcal{P}(x,y)\,\mathrm{d}x\,\mathrm{d}y = 1 \quad \text{or} \quad \int_{0}^{2\pi}\int_{0}^{\infty}\mathcal{P}(r,\phi)\,r\,\mathrm{d}r\,\mathrm{d}\phi = 1 \tag{A.15}$$

In case of isotropic scattering, equation A.15 can be simplified:

$$2\pi\int_{0}^{\infty}\mathcal{P}(r)\,r\,\mathrm{d}r = 1 \tag{A.16}$$

When using the integral form of equation A.13

$$M(x,y) = \int_{-\infty}^{\infty}\int_{-\infty}^{\infty}E(x-\xi,y-\upsilon)\mathcal{P}(\xi,\upsilon)\,\mathrm{d}\xi\,\mathrm{d}\upsilon \tag{A.17}$$

and the irradiance E and therefore also the exitance M are constant over y and $y-\upsilon$ respectively, it can be written as:

$$M(x) = \int_{-\infty}^{\infty}E(x-\xi)\int_{-\infty}^{\infty}\mathcal{P}(\xi,\upsilon)\,\mathrm{d}\upsilon\,\mathrm{d}\xi \tag{A.18}$$

Replacement of the inner integral with a function $\mathcal{L}(\xi)$ leads to the 1D convolution

$$M(x) = \int_{-\infty}^{\infty}E(x-\xi)\mathcal{L}(\xi)\,\mathrm{d}\xi \tag{A.19}$$

$$\boxed{M(x) = (E * \mathcal{L})(x)} \tag{A.20}$$

where $\mathcal{L}$ is the *line spread function* (LSF):

$$\boxed{\mathcal{L}(x) = \int_{-\infty}^{\infty}\mathcal{P}(x,y)\,\mathrm{d}y} \tag{A.21}$$

For constant irradiance, equation A.12 becomes:

$$\int_{-\infty}^{\infty}M(x)\,\mathrm{d}x = \int_{-\infty}^{\infty}E(x)\,\mathrm{d}x \tag{A.22}$$

and by using equation A.20, M can be eliminated:

$$\int_{-\infty}^{\infty}(E * \mathcal{L})(x)\,\mathrm{d}x = \int_{-\infty}^{\infty}E(x)\,\mathrm{d}x \tag{A.23}$$

With the integration of a convolution according to Fubini's theorem, this leads to

$$\int_{-\infty}^{\infty}E(x)\,\mathrm{d}x\cdot\int_{-\infty}^{\infty}\mathcal{L}(x)\,\mathrm{d}x = \int_{-\infty}^{\infty}E(x)\,\mathrm{d}x, \tag{A.24}$$

which requires that:

$$\boxed{\int_{-\infty}^{\infty} \mathcal{L}(x)\,\mathrm{d}x = 1} \tag{A.25}$$

When using the polar description of the PSF $\mathcal{P}(r)$

$$\mathcal{P}(r) = \mathcal{P}(\sqrt{x^2+y^2}) \tag{A.26}$$

in equation A.2, this leads to:

$$\mathcal{L}(x) = \int_{-\infty}^{\infty} \mathcal{P}(\sqrt{x^2+y^2})\,\mathrm{d}y \tag{A.27}$$

$$= 2 \cdot \int_{0}^{\infty} \mathcal{P}(\sqrt{x^2+y^2})\,\mathrm{d}y \tag{A.28}$$

Substituting y by r with

$$y = \sqrt{r^2-x^2}, \quad \frac{\mathrm{d}y}{\mathrm{d}r} = \frac{r}{\sqrt{r^2-x^2}}, \quad r(y=0) = x, \quad r(y\to\infty) \to \infty \tag{A.29}$$

the LSF can be written as:

$$\boxed{\mathcal{L}(x) = 2 \cdot \int_{x}^{\infty} \mathcal{P}(r) \frac{r}{\sqrt{r^2-x^2}}\,\mathrm{d}r} \tag{A.30}$$

The transformation from LSF to ESF $E(x)$ is given by integrating the LSF from negative infinity to x:

$$\boxed{\mathcal{E}(x) = \int_{-infty}^{x} \mathcal{L}(u)\,\mathrm{d}u} \tag{A.31}$$

This can be reverted by differentiating the ESF with respect to x, which leads to the following formulation of the LSF:

$$\mathcal{L}(x) = \frac{\mathrm{d}}{\mathrm{d}x}\mathcal{E}(x). \tag{A.32}$$

For the transformation equation from LSF to PSF, equation A.28 must be solved for $\mathcal{P}$. For this purpose, the Abelian itegration equation can be used, as described by Marchand [18, 19]. For the case at hand, Marchand presents the following equation for the PSF:

$$\mathcal{P}(z) = -\frac{2}{\pi} \int_{0}^{\infty} \mathcal{L}'(v^2+z)\,\mathrm{d}v, \tag{A.33}$$

where t, v, and z are auxiliary variables defined by

$$t = v^2 + z = x^2. \tag{A.34}$$

Therefore, the derivative $\mathcal{L}'$ can be transformed to:

$$\mathcal{L}'(v^2 + z) = \mathcal{L}'(t) = \frac{\mathrm{d}\mathcal{L}}{\mathrm{d}t}. \tag{A.35}$$

With $t = x^2$ and thus

$$\frac{\mathrm{d}}{\mathrm{d}t} = \frac{1}{2x}\frac{\mathrm{d}}{\mathrm{d}x} \tag{A.36}$$

the right hand side of equation A.2 becomes

$$-\frac{2}{\pi}\int_0^\infty \frac{1}{2x}\mathcal{L}'(x)\,\mathrm{d}v. \tag{A.37}$$

Substituting v with x, while

$$v^2 = x^2 - r^2, \quad \frac{\mathrm{d}v}{\mathrm{d}x} = \frac{x}{\sqrt{x^2 - r^2}}, \quad x(v = 0) = r, \quad x(v \to \infty) \to \infty, \tag{A.38}$$

the PSF can be formulated by:

$$\mathcal{P}(r) = -\frac{1}{\pi}\int_r^\infty \frac{\mathcal{L}'(x)}{\sqrt{x^2 - r^2}}\,\mathrm{d}x. \tag{A.39}$$

A.3 LSFs from PSF Functions

The following PSFs will be presented:

- Pillbox PSF (PBX)
- Ramp PSF (RAM)
- Gaussian PSF (GAU)
- Exponential PSF (EXP)
- Modified exponential PSF according to Gustavson (EMG)
- Quadratic-Rational PSF (QUA)

All functions will be presented in dimensionless coordinates

$$u = \frac{r}{s} \quad \text{and} \quad v = \frac{x}{s},$$

where s is a characteristic length, called the form parameter in the previous chapters. The corresponding functions, all isotropic, are:

$$\mathcal{P}_{\mathrm{PBX}}(u) = \begin{cases} a & \text{for } u \leq 1 \\ 0 & \text{else} \end{cases} \tag{A.40}$$

$$\mathcal{P}_{\mathrm{RAM}}(u) = \begin{cases} 3a \cdot (1-u) & \text{for } u \leq 1 \\ 0 & \text{else} \end{cases} \tag{A.41}$$

$$\mathcal{P}_{\mathrm{GAU}}(u) = \frac{a}{2} \cdot \exp\left(-\frac{1}{2}\,u^2\right) \tag{A.42}$$

$$\mathcal{P}_{\mathrm{EXP}}(u) = \frac{a}{2} \cdot \exp\left(-u\right) \tag{A.43}$$

$$\mathcal{P}_{\mathrm{EMG}}(u) = \frac{a}{2u} \cdot \exp\left(-u\right) \tag{A.44}$$

$$\mathcal{P}_{\mathrm{QUA}}(u) = \frac{a}{2} \cdot \sinh^{-1}(b) \cdot \frac{1}{1+u^2} \tag{A.45}$$

where

$$a = \frac{1}{2\pi} \quad \text{and} \quad b = u_{\max} = \frac{r_{\max}}{s}$$

with $r_{\max}$ being the radius that is the last evaluated. All functions are normalized that the law of energy conservation is satisfied. This means that all $\mathcal{P}_i$ satisfy equation A.2. The scaling factor for $\mathcal{P}_{\mathrm{QUA}}$ depends on the size of the evaluated region, which stands in contrast with physical considerations.

Figures A.1a and A.2a show the different PSFs in independent coordinates r/s and $\mathcal{P} \cdot s^2$. Figures A.1b and A.2b present, the corresponding LSFs, again in independent coordinates x/s and $\mathcal{L} \cdot s$. The LSFs

are normalized to $\int \mathcal{L}(x)\,\mathrm{d}x = 1$. For the plot of the quadratic-rational PSF and its LSF the evaluation limit b is set to 5.

Pillbox PSF

A very simple PSF is the pillbox PSF $\mathcal{P}_{\mathrm{PBX}}$. For a defined radius $r = s$, the PSF has a constant value and drops to zero for $r > s$. This creates the typical pillbox shape. The pillbox PSF is defined by:

$$\mathcal{P}_{\mathrm{PBX}}(u) = \begin{cases} a & \text{for } u \leq 1 \\ 0 & \text{else} \end{cases} \tag{A.46}$$

From the pillbox PSF, an LSF $\mathcal{L}_{\mathrm{PBX}}$ can be derived that shows a semi-circular center.

$$\mathcal{L}_{\mathrm{PBX}}(v) = \begin{cases} 2as\sqrt{1-v^2} & \text{for } |v| \leq 1 \\ 0 & \text{else} \end{cases} \tag{A.47}$$

Ramp PSF

The ramp PSF drops linearly from a given starting value and reaches zero at the radius $r = s$. For radii $r > s$ it is zero. This way, the PSF has a conical form. It is defined by:

$$\mathcal{P}_{\mathrm{RAM}}(u) = \begin{cases} 3a \cdot (1-u) & \text{for } u \leq 1 \\ 0 & \text{else.} \end{cases} \tag{A.48}$$

The corresponding LSF is defined by:

$$\mathcal{L}_{\mathrm{RAM}}(v) = \begin{cases} 3as \cdot \left(\sqrt{1-v^2} + v^2 \ln\left[\dfrac{|v|}{1+\sqrt{1-v^2}} \right] \right) & \text{for } |v| \leq s \\ 0 & \text{else.} \end{cases} \tag{A.49}$$

This LSF function is not defined for $x = 0$. Nevertheless, this is a removable discontinuity using $\mathcal{L}_{\mathrm{RAM}}(x = 0) = a \cdot s$. This leads to the complete definition:

$$\mathcal{L}_{\mathrm{RAM}}(v) = \begin{cases} 3as \cdot \left(\sqrt{1-v^2} + v^2 \ln\left[\dfrac{|v|}{1+\sqrt{1-v^2}} \right] \right) & \text{for } |v||v| \leq s \\ 3as & \text{for } v = 0 \\ 0 & \text{else.} \end{cases} \tag{A.50}$$

Gaussian PSF

The Gaussian PSF and its corresponding LSF both show a continuous and smooth run. The PSF is defined by:

$$\mathcal{P}_{\mathrm{GAU}}(u) = \frac{a}{2} \cdot \exp\left(-\frac{1}{2}\, u^2 \right) \tag{A.51}$$

The corresponding LSF is defined by:

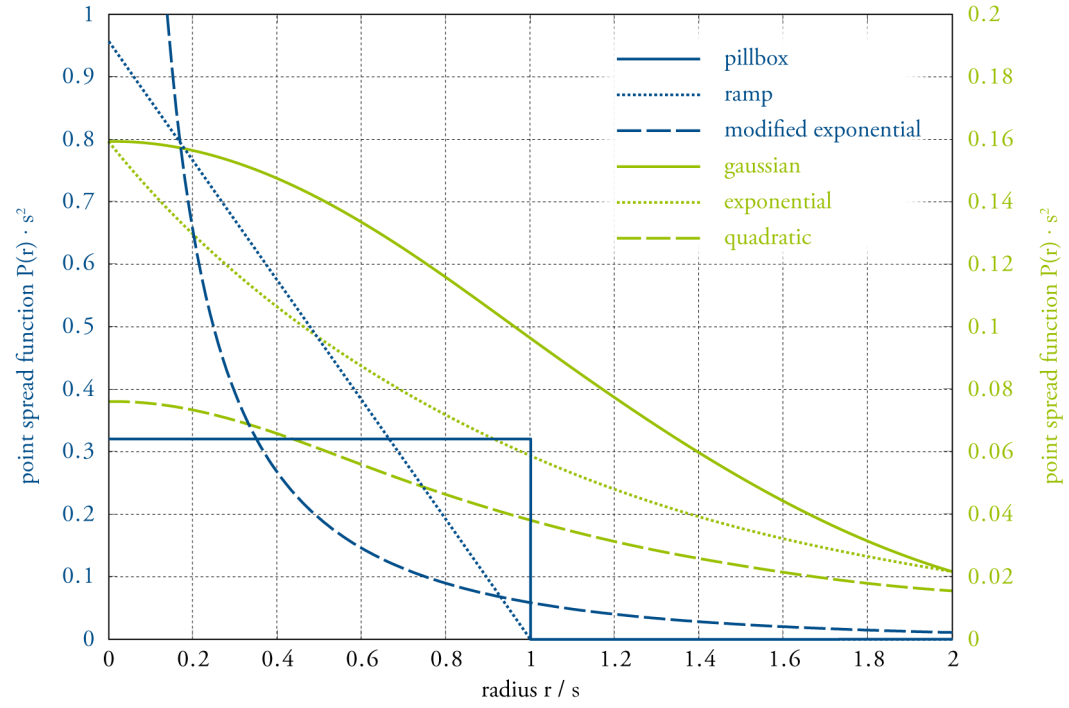

(a) Point Spread Functions

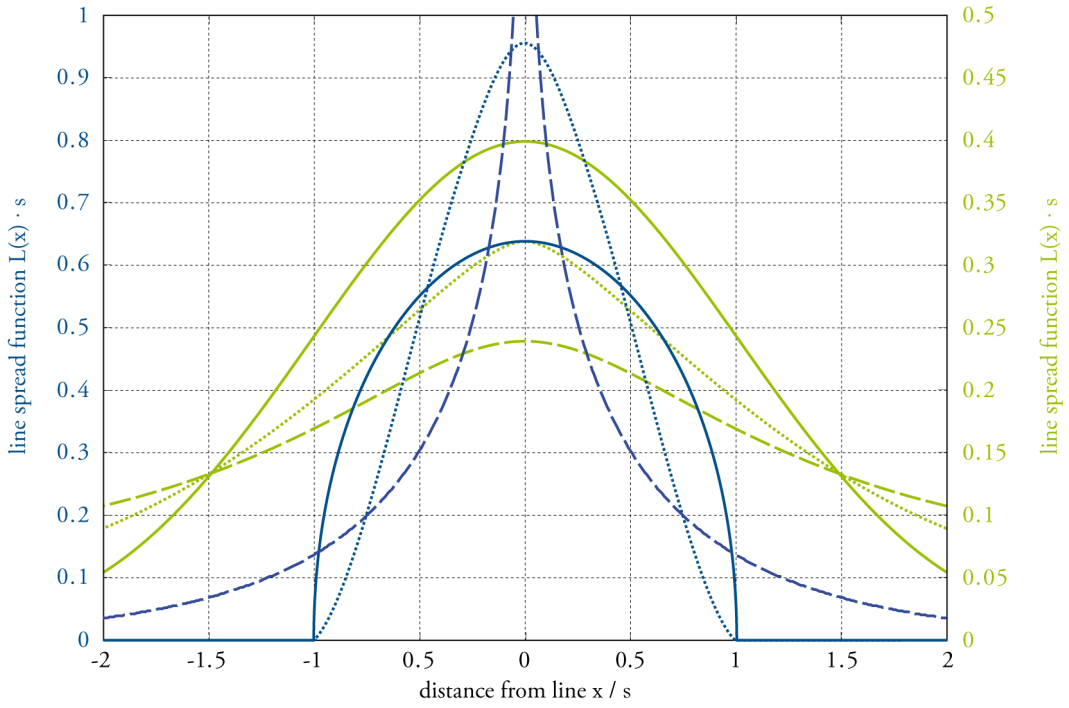

(b) Line Spread Functions

Figure A.1: Different types of PSFs (a) and their corresponding LSFs (b), linear scale.

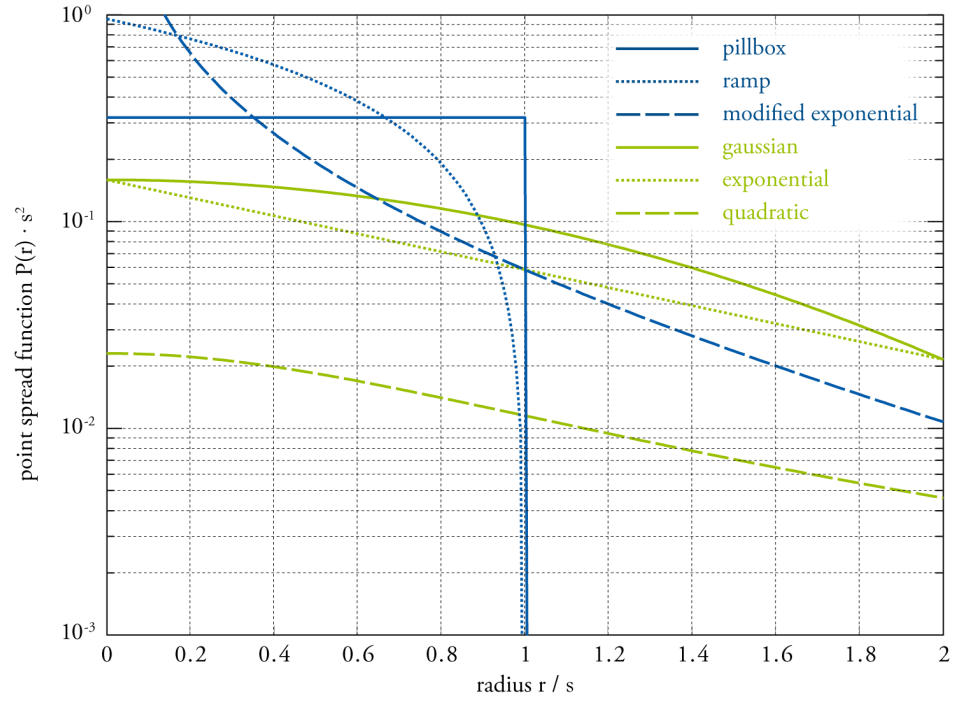

(a) Point Spread Functions

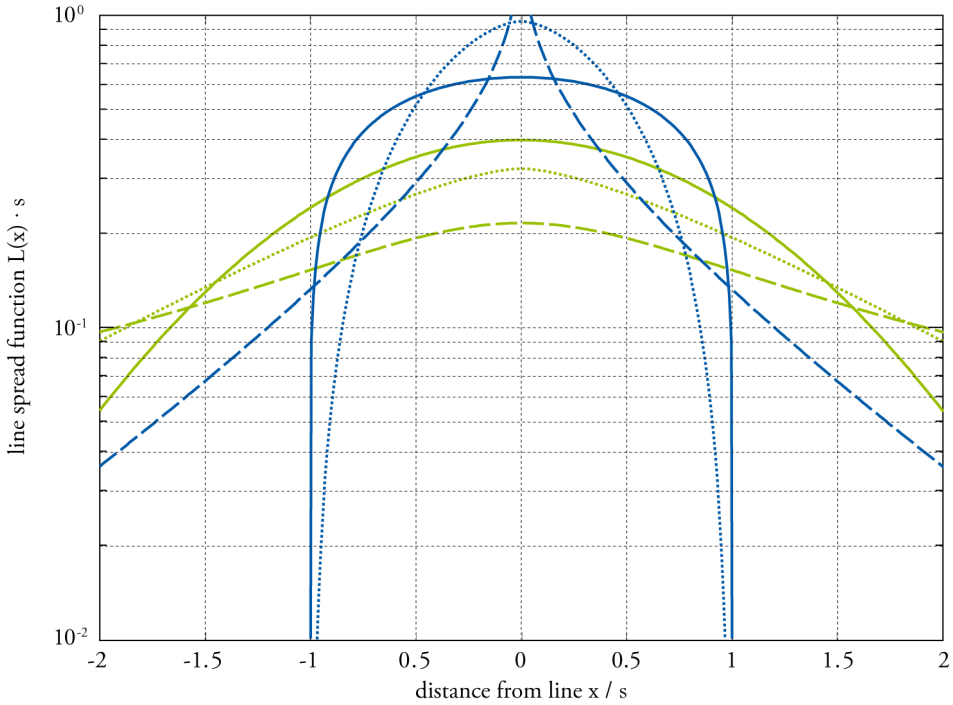

(b) Line Spread Functions

Figure A.2: Different types of PSFs (a) and their corresponding LSFs (b), logarithmic scale.

$$\mathcal{L}_{\mathrm{GAU}}(v) = \lim_{b\to\infty} as \cdot \int_u^b \exp\left(-\frac{1}{2}\,u^2\right) \frac{u}{\sqrt{u^2 - v^2}}\,\mathrm{d}u \tag{A.52}$$

$$\approx as\sqrt{\frac{\pi}{2}} \cdot \exp\left(-\frac{1}{2}\,v^2\right). \tag{A.53}$$

Exponential PSF

The exponential PSF is a continuous function, but it is not smooth at $r = 0$. It is defined by:

$$\mathcal{P}_{\mathrm{EXP}}(u) = \frac{a}{2} \cdot \exp\left(-u\right) \tag{A.54}$$

Using the Bessel function K_n of the second kind, the LSF can be written as:

$$\mathcal{L}_{\mathrm{EXP}}(v) = as|u| \cdot K_1(|u|). \tag{A.55}$$

Modified Exponential According to Gustavson

This is a modification of the exponential equation, introduced by Gustavson [95].

$$\mathcal{P}_{\mathrm{EMG}}(u) = \frac{a}{2u} \cdot \exp\left(-u\right) \tag{A.56}$$

This PSF and its corresponding LSF go to infinity for $x \to 0$, which causes a discontinuity of the LSF that cannot be removed:

$$\mathcal{L}_{\mathrm{EMG}}(v) = as \cdot K_1(|u|). \tag{A.57}$$

where K_n is the Bessel function of the second kind. For computations in this work, the values of the LSF for $x = 0$ were replaced by their values at $x = s/1000$.

Quadratic PSF

The quadratic PSF and its corresponding LSF show a continuous and smooth run. The indefinite integral of the LSF tends to infinity. Therefore, the amplitude of LSF and PSF depend on their extent, denoted by the maximum radius that is evaluated $r_{\max} = b \cdot s$. This way, the PSF can be written as:

$$\mathcal{P}_{\mathrm{QUA}}(u) = \frac{a}{2} \cdot \sinh^{-1}(b) \cdot \frac{1}{1 + u^2}. \tag{A.58}$$

The corresponding LSF can be written as:

$$\mathcal{L}_{\mathrm{QUA}}(v) = \frac{a\pi s}{2} \cdot \sinh^{-1}(b) \cdot \frac{1}{\sqrt{1 + u^2}}. \tag{A.59}$$

Appendix B

Measurements

This appendix summarizes all measurements that were performed for this thesis. All reflectance measurements were taken using Techkon SpectroDens Pro, spectrophotometer with 45°/0° measurement geometry, using a black backing. This way, differences in transparency due to different paper weights are visible.

For the illustrations of light scattering measurements, the measured ESFs are presented. All measurements of this appendix were derived using the green LED. For each paper sample, three specimen were measured and their ESFs were averaged. The black solid line always indicates the reference ESF of the FS mirror. The indicatrices were derived with six measurements with an angular difference of 30°. For visualization purposes, these measurements were duplicated to cover a full range of 360°.

For the LSF and PSF calculations, all ESFs of each paper type were averaged. In the LSF illustrations, also the result of the linear programming is plotted. The tables summarize the RMSD of the fittings and the linear programming, as well as the form parameters s.

B.1 Felix Schöller Papers

Series	Coating	Grammage	Color
PE-Photopaper (swellable)	glossy	230 g/m^2	Ultra 8
	matte	230 g/m^2	Ultra 8
PE-Photopaper (microporous)	glossy	240 g/m^2	UltraWhite
	matte	240 g/m^2	UltraWhite
Proofing Paper	matte	200 g/m^2	ND
	matte	275 g/m^2	ND
Epson Premium Glossy PP	glossy	255 g/m^2	ND

Table B.1: Investigated Felix Schöller papers.

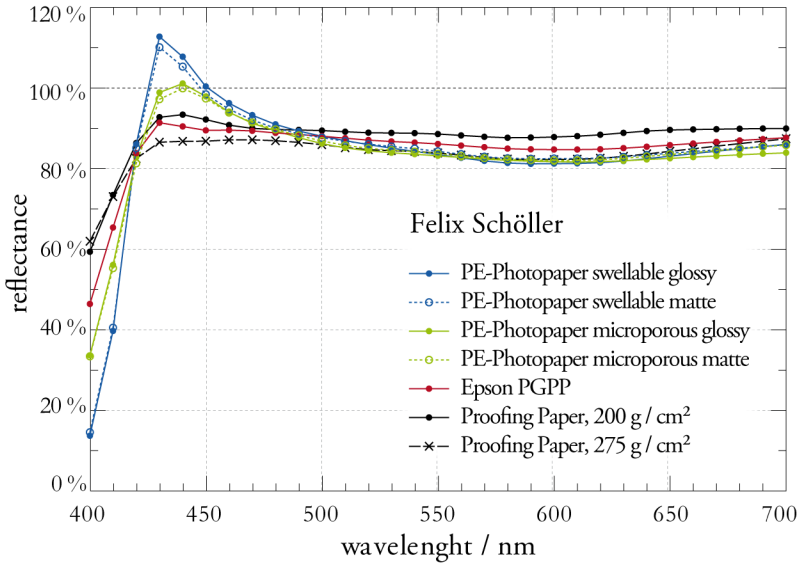

Figure B.1: Reflectance spectra for Felix Schöller papers.

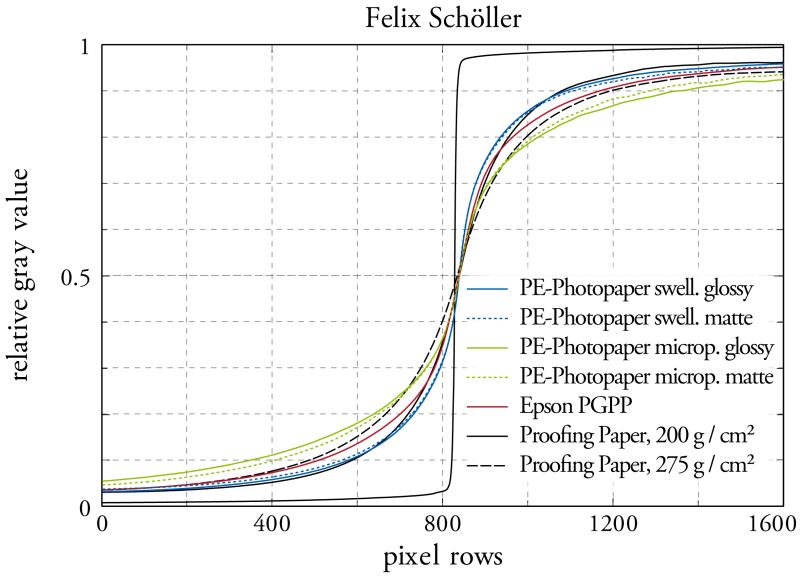

Figure B.2: ESFs for Felix Schöller papers.

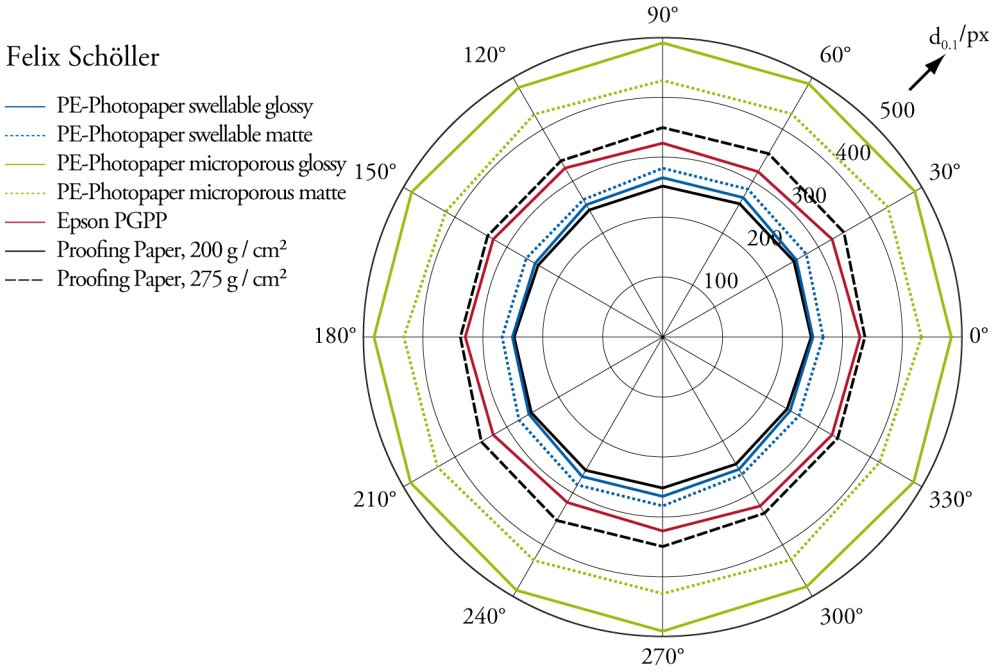

Figure B.3: 0.1-indicatrices for Felix Schöller papers.

Value	PBX	LIN	GAU	EXP	EMG	QUA	linprog
PE-Photopaper, swellable, glossy							
s/px	229	318	131	89	200	0,62	
RMSD·1000	49,89	45,07	41,82	33,36	18,30	32,47	8,39
PE-Photopaper, swellable, matte							
s/px	229	319	131	89	200	0,63	
RMSD·1000	48,59	43,79	40,55	32,18	17,53	33,66	8,98
PE-Photopaper, microporous, glossy							
s/px	465	648	265	174	385	10,08	
RMSD·1000	67,54	59,68	54,42	41,66	20,88	14,08	18,07
PE-Photopaper, microporous, matte							
s/px	413	573	235	156	342	7,15	
RMSD·1000	60,60	53,39	48,52	36,33	16,44	22,21	14,12
Proofing Paper, matte, 200 g/m^2							
s/px	250	344	141	94	207	0,95	
RMSD·1000	37,64	32,44	28,91	20,41	10,62	45,91	6,94
Proofing Paper, matte, 275 g/m^2							
s/px	355	491	201	133	292	4,84	
RMSD·1000	44,80	38,25	33,72	22,62	9,28	39,42	9,55
Epson Premium Glossy Photo Paper							
s/px	315	438	180	121	268	2,82	
RMSD·1000	55,00	48,97	44,88	34,26	16,60	30,25	10,74

Table B.2: Results of the LSF calculation for investigated Felix Schöller papers; form parameter s and RMSD.

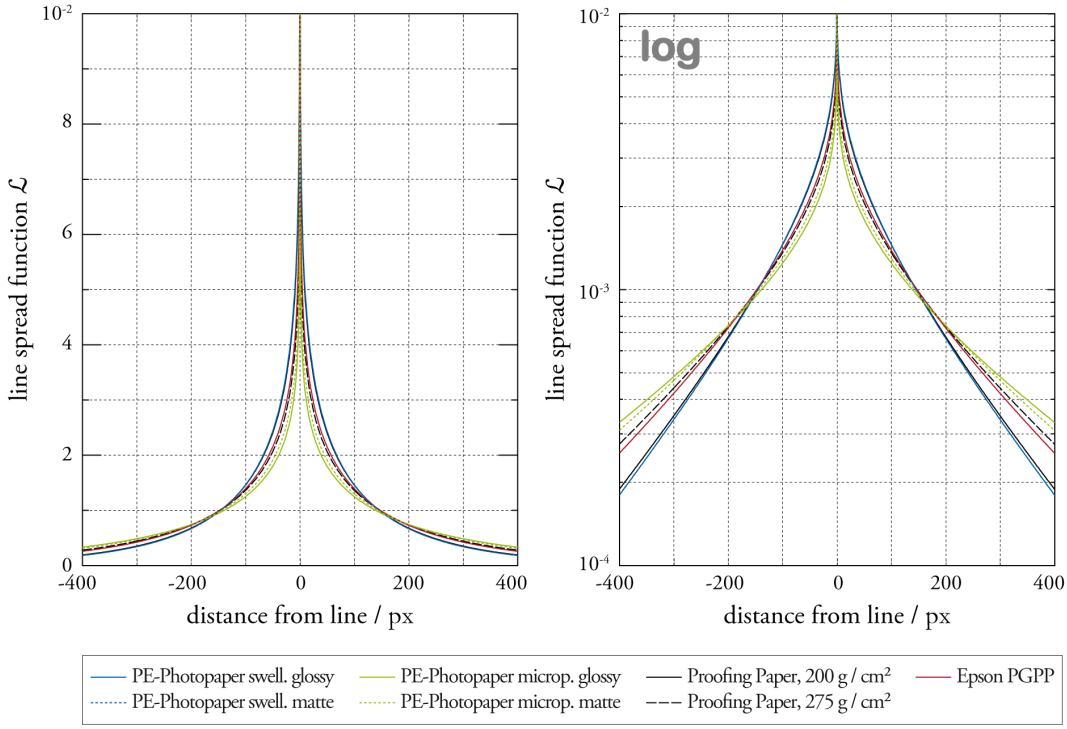

Figure B.4: LSFs for Felix Schöller papers.

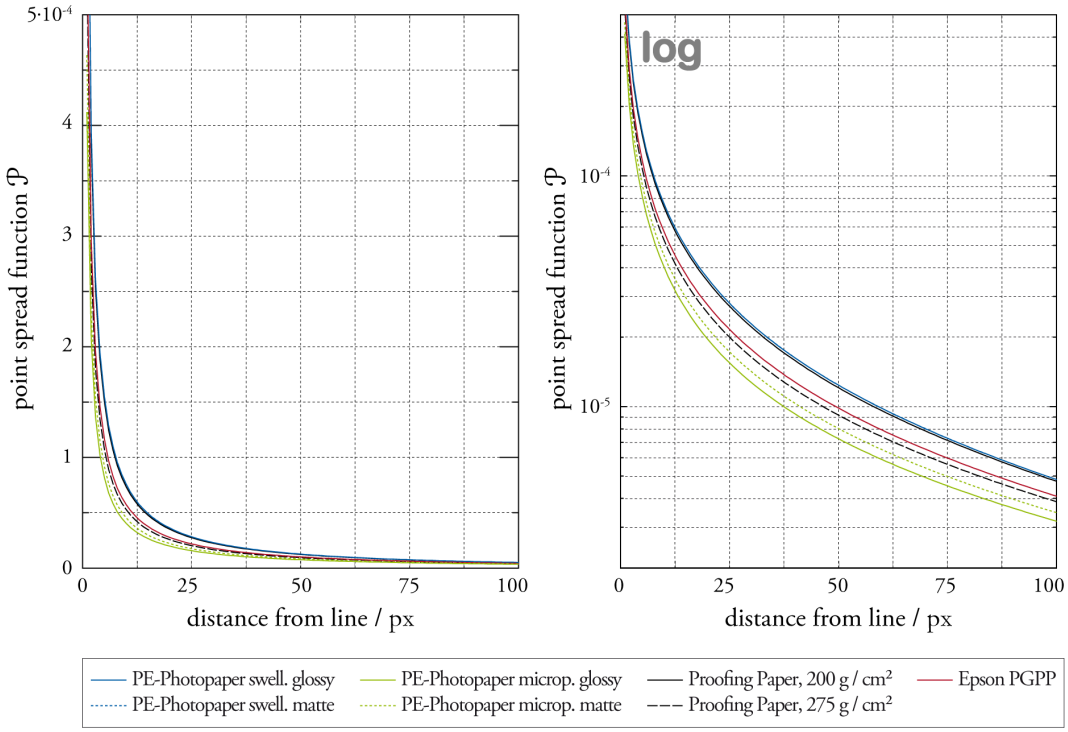

Figure B.5: PSFs for Felix Schöller papers.

B.2 IGEPA Papers

Series	Coating	Grammage	Color
Evergreen Natural	uncoated	90 g/m^2	white
Evergreen Technique	uncoated	148 g/m^2	crystal white

Table B.3: Investigated IGEPA papers.

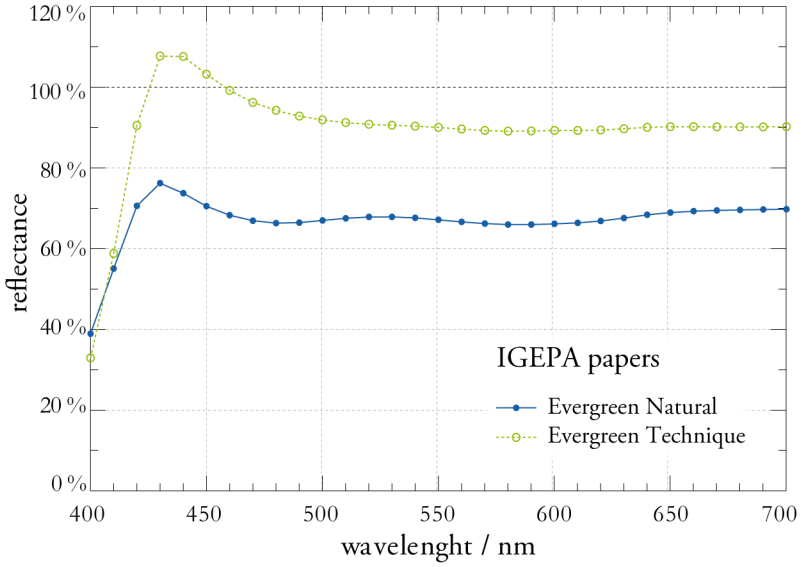

Figure B.6: Reflectance spectra for IGEPA papers.

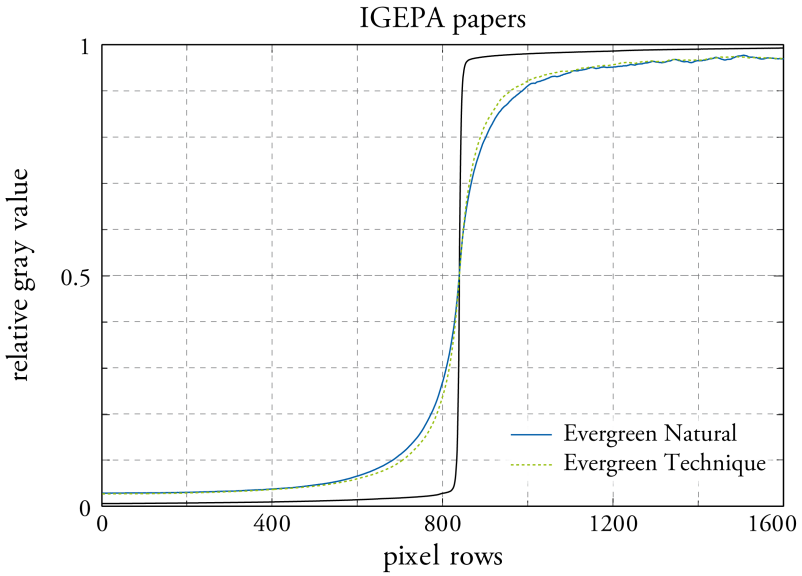

Figure B.7: ESFs for IGEPA papers.

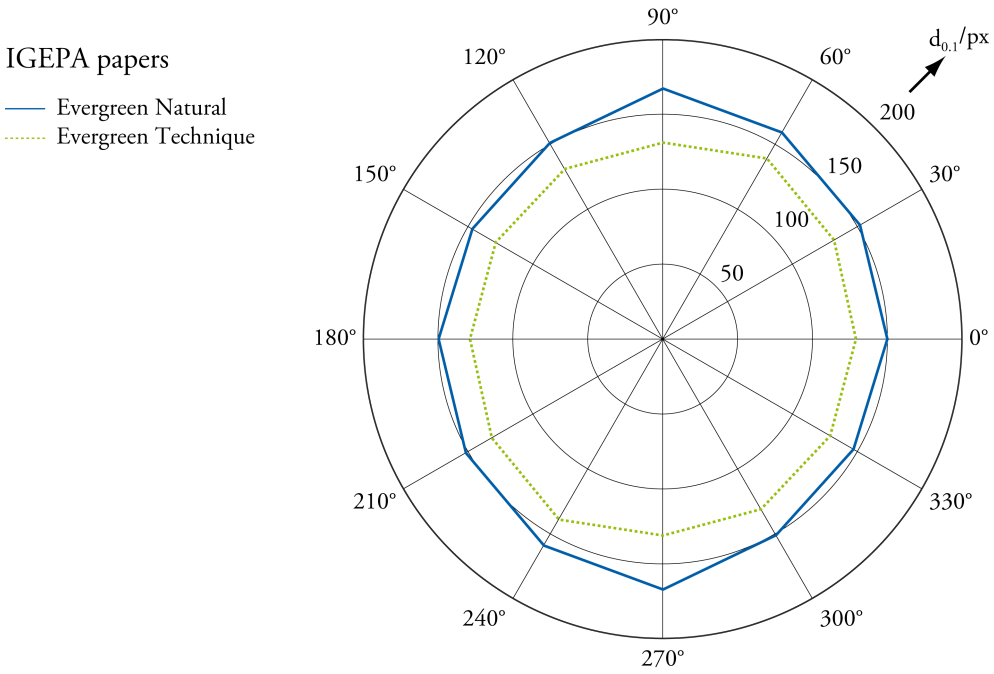

Figure B.8: 0.1-indicatrices for IGEPA papers.

Value	PBX	LIN	GAU	EXP	EMG	QUA	linprog
Evergreen Natural							
s/px	142	197	81	54	122	0,13	
RMSD·1000	34,81	31,17	28,76	22,86	14,12	40,41	6,72
Evergreen Technique							
s/px	114	158	65	44	101	0,09	
RMSD·1000	34,70	31,62	29,54	24,42	16,36	36,15	6,40

Table B.4: Results of the LSF calculation for investigated IGEPA papers; form parameter s and RMSD.

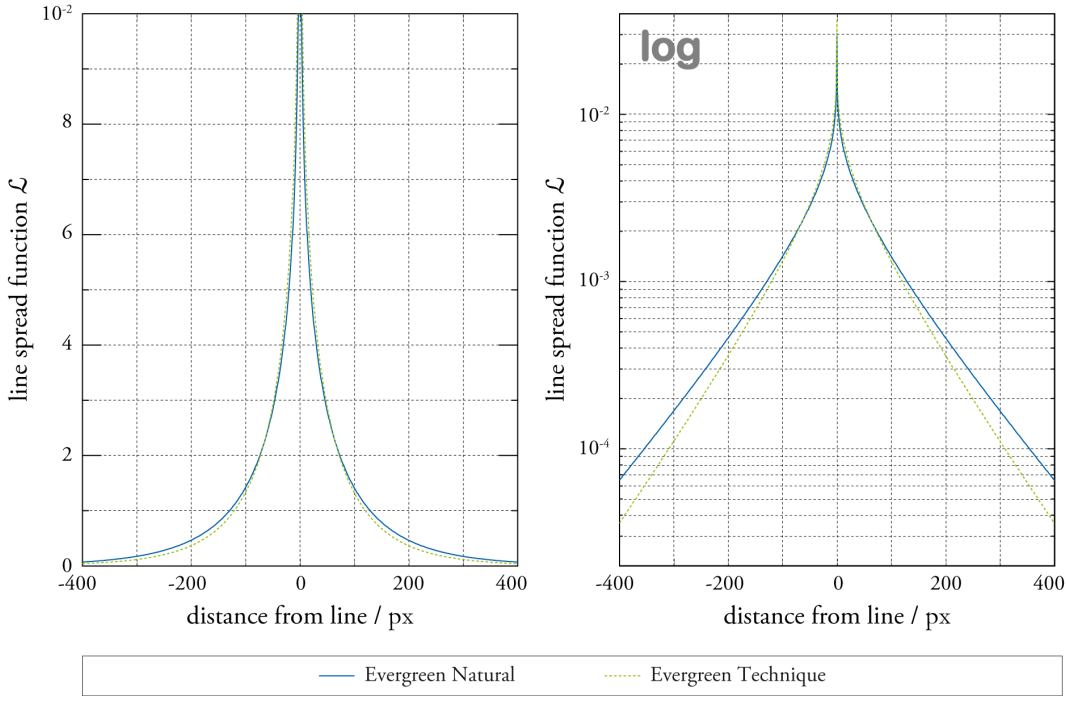

Figure B.9: LSFs for IGEPA papers.

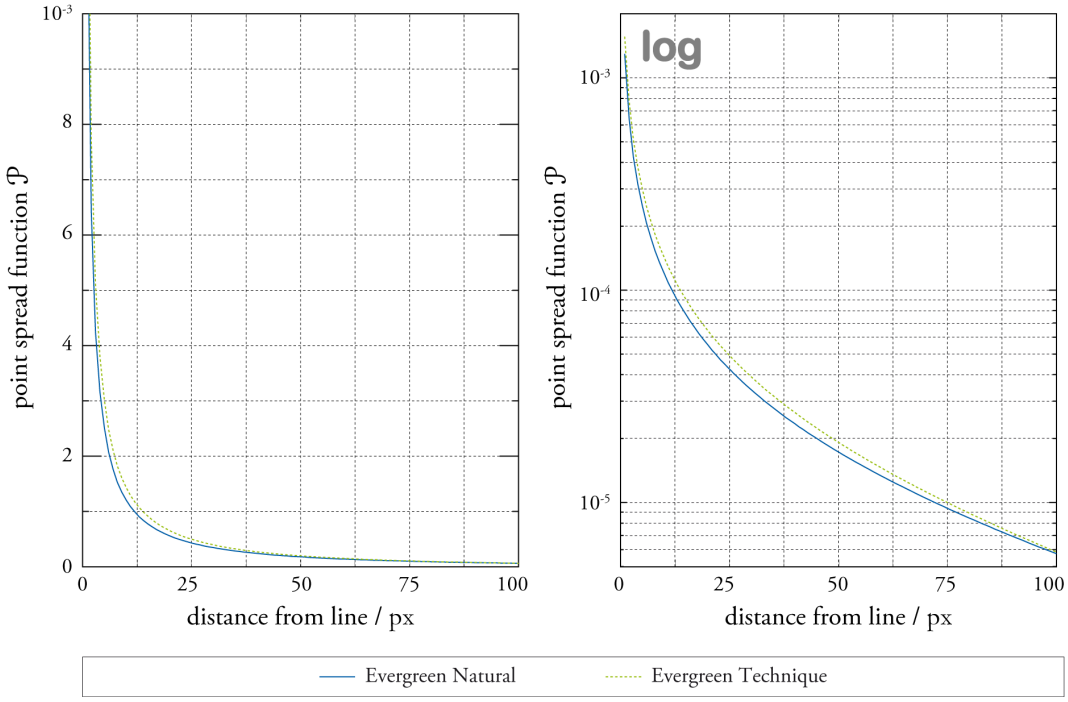

Figure B.10: PSFs for IGEPA papers.

B.3 Scheufelen Papers

Series	Coating	Grammage	Color
BVS	glossy	150 g/m^2	gloss white
	glossy	170 g/m^2	gloss white
	glossy	200 g/m^2	gloss white
	glossy	300 g/m^2	gloss white
	matte	90 g/m^2	dull white
	matte	115 g/m^2	dull white
	matte	130 g/m^2	dull white
	matte	135 g/m^2	dull white
	matte	150 g/m^2	dull white
	matte	170 g/m^2	dull white
	matte	200 g/m^2	dull white
	matte	300 g/m^2	dull white
Consort Royal	matte	135 g/m^2	silk tint
	matte	250 g/m^2	silk tint
Job Parilux	glossy	135 g/m^2	gloss white
	matte	135 g/m^2	silk white
	matte	250 g/m^2	dull cream
heaven 42	matte	250 g/m^2	soft dull absolute white

Table B.5: Investigated Scheufelen papers.

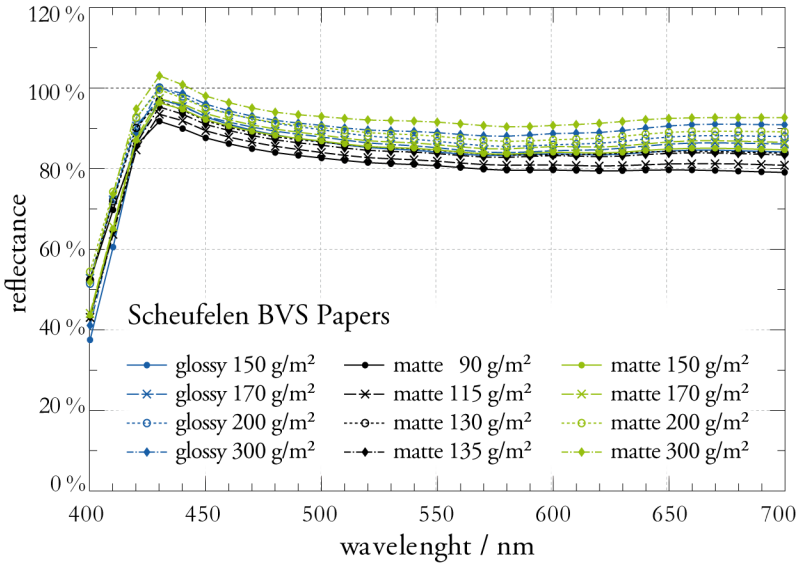

Figure B.11: Reflectance spectra for Scheufelen BVS papers.

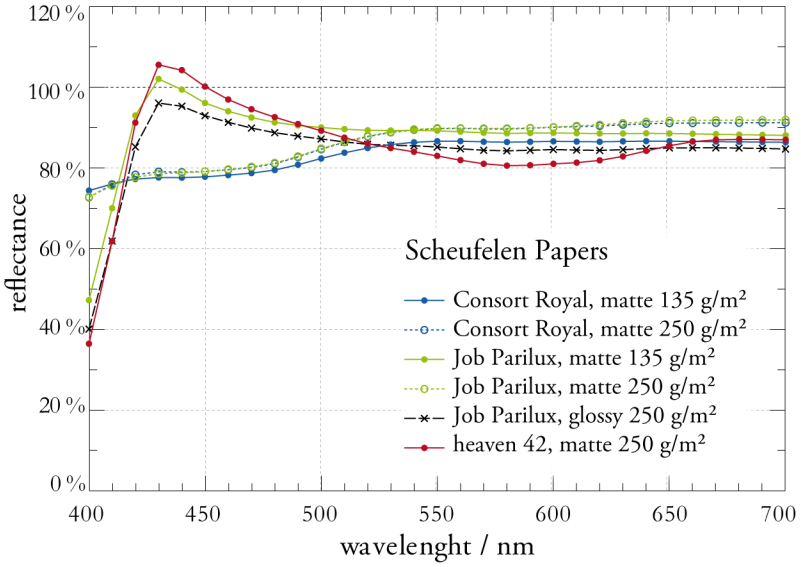

Figure B.12: Reflectance spectra for other Scheufelen papers.

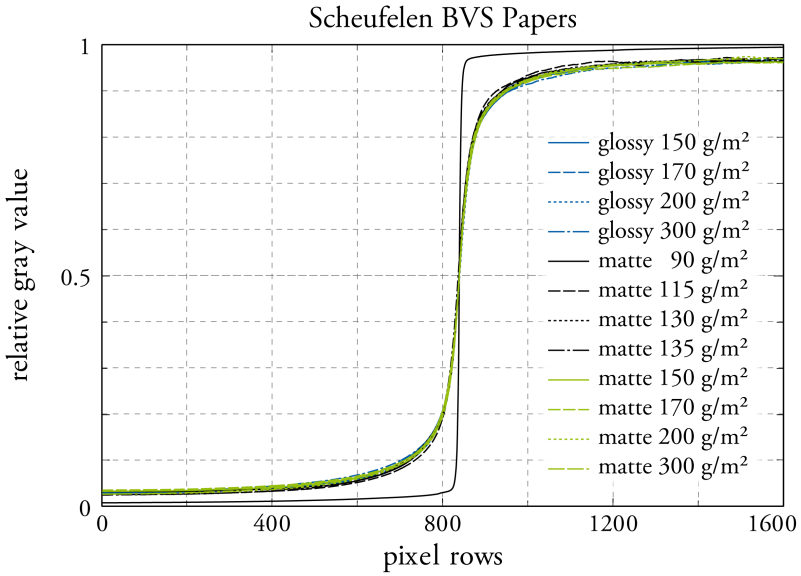

Figure B.13: ESFs for Scheufelen BVS papers.

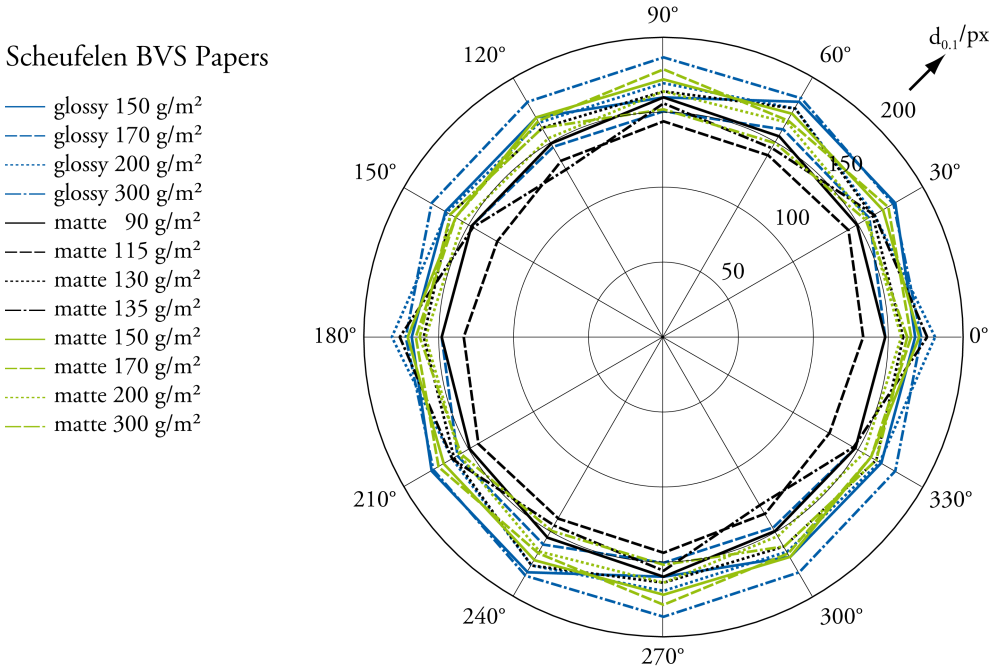

Figure B.14: 0.1-indicatrices for Scheufelen BVS papers.

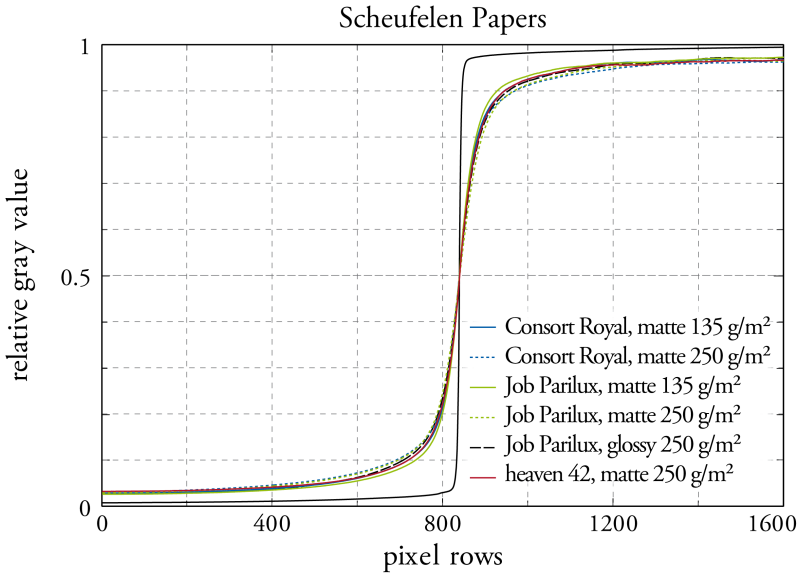

Figure B.15: ESFs for other Scheufelen papers.

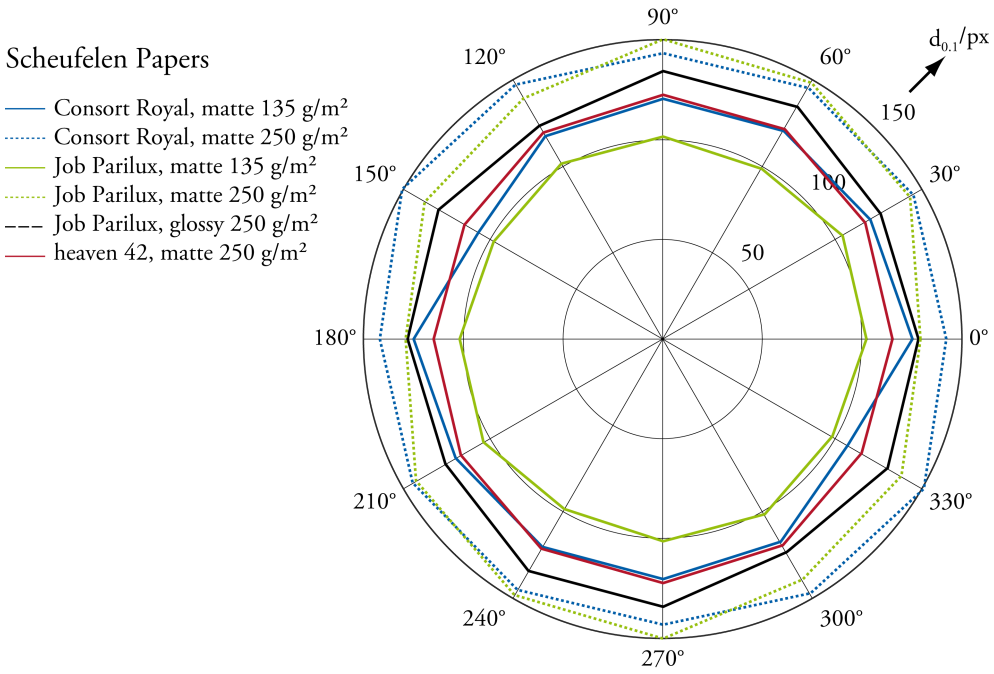

Figure B.16: 0.1-indicatrices for other Scheufelen papers.

Value	PBX	LIN	GAU	EXP	EMG	QUA	linprog
BVS, glossy 150 g/m^2							
s/px	95	134	55	38	91	0,08	
RMSD·1000	37,65	35,08	33,26	28,70	20,97	30,63	7,57
BVS, glossy 170 g/m^2							
s/px	83	118	49	34	82	0,07	
RMSD·1000	36,93	0,00	0,00	0,00	0,00	0,00	0,00
BVS, glossy 200 g/m^2							
s/px	91	129	54	37	89	0,08	
RMSD·1000	38,51	0,00	0,00	0,00	0,00	0,00	0,00
BVS, glossy 300 g/m^2							
s/px	93	133	55	39	94	0,09	
RMSD·1000	42,49	40,10	38,38	33,96	26,00	26,58	8,47
BVS, matte 90 g/m^2							
s/px	89	125	52	36	84	0,08	
RMSD·1000	37,70	35,21	33,48	29,14	21,77	29,15	8,66
BVS, matte 115 g/m^2							
s/px	78	109	45	31	73	0,06	
RMSD·1000	30,52	28,24	26,58	22,58	16,43	33,04	5,56
BVS, matte 130 g/m^2							
s/px	91	128	53	37	86	0,07	
RMSD·1000	37,03	34,39	32,53	27,81	19,59	30,35	6,80
BVS, matte 135 g/m^2							
s/px	81	115	48	33	81	0,07	
RMSD·1000	38,66	36,43	34,82	30,73	23,49	26,94	7,94
BVS, matte 150 g/m^2							
s/px	89	126	53	37	88	0,08	
RMSD·1000	38,94	36,72	35,10	31,10	24,45	30,69	9,16

Value	PBX	LIN	GAU	EXP	EMG	QUA	linprog
BVS, matte 170 g/m^2							
s/px	85	121	50	35	87	0,08	
RMSD·1000	0,00	0,00	0,00	0,00	0,00	0,00	0,00
BVS, matte 200 g/m^2							
s/px	87	123	51	35	83	0,07	
RMSD·1000	34,94	32,47	30,71	26,32	18,98	31,40	6,11
BVS, matte 300 g/m^2							
s/px	89	126	52	37	89	0,08	
RMSD·1000	39,20	36,90	35,21	30,93	23,45	28,59	6,50
Consort Royal, matte 135 g/m^2							
s/px	94	132	55	38	89	0,08	
RMSD·1000	33,22	30,88	29,15	25,08	19,30	35,86	6,68
Consort Royal, matte 250 g/m^2							
s/px	116	164	68	48	114	0,12	
RMSD·1000	41,69	38,91	36,87	31,81	23,37	32,51	7,57
Job Parilux, glossy 135 g/m^2							
s/px	112	158	65	44	103	0,10	
RMSD·1000	33,91	31,07	28,99	24,11	17,27	38,10	6,24
Job Parilux, matte 135 g/m^2							
s/px	90	126	52	36	83	0,07	
RMSD·1000	31,09	28,81	27,11	23,18	17,81	36,48	5,52
Job Parilux, matte 250 g/m^2							
s/px	121	170	71	49	114	0,13	
RMSD·1000	36,52	33,86	31,83	27,10	20,55	38,68	6,85
heaven 42, matte 250 g/m^2							
s/px	106	148	61	42	98	0,10	
RMSD·1000	35,16	32,76	31,00	26,95	21,34	36,73	8,37

Table B.6: Results of the LSF calculation for investigated Scheufelen papers; form parameter s and RMSD.

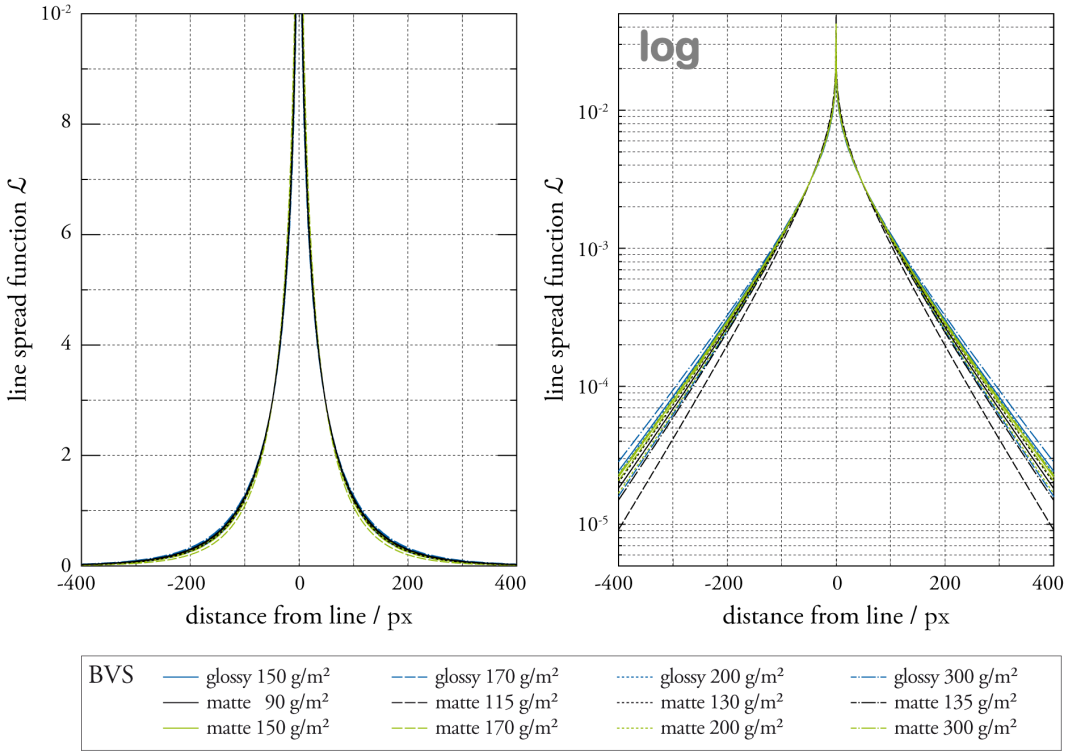

Figure B.17: LSFs for Scheufelen BVS papers.

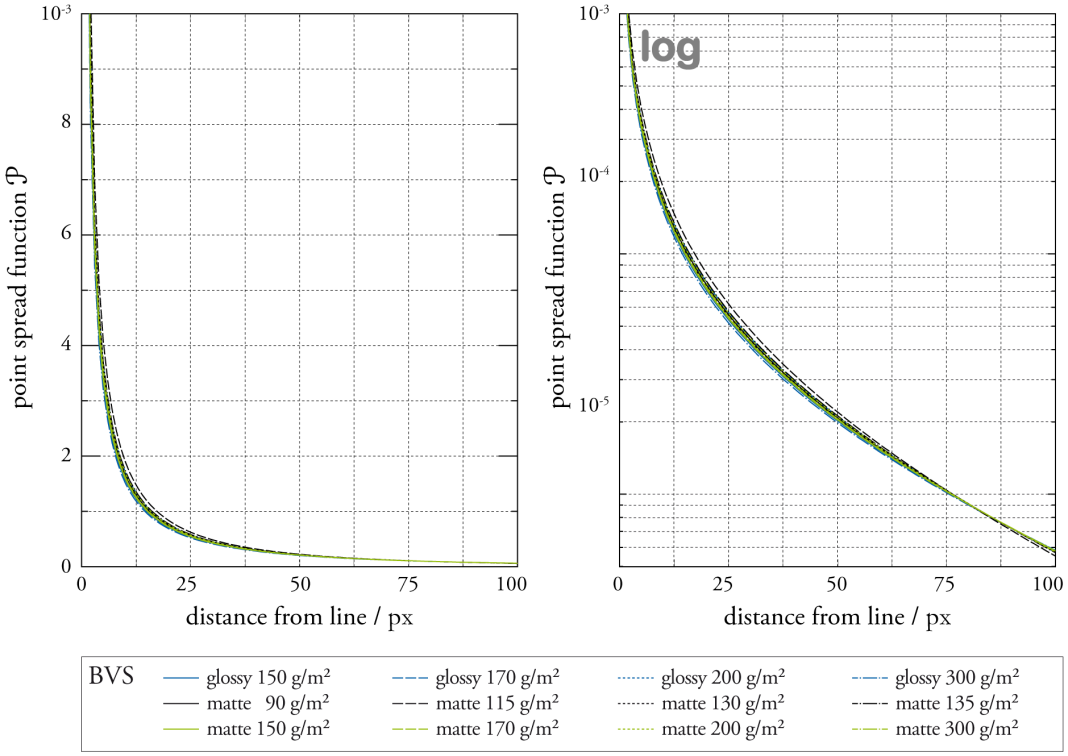

Figure B.18: PSFs for Scheufelen BVS papers.

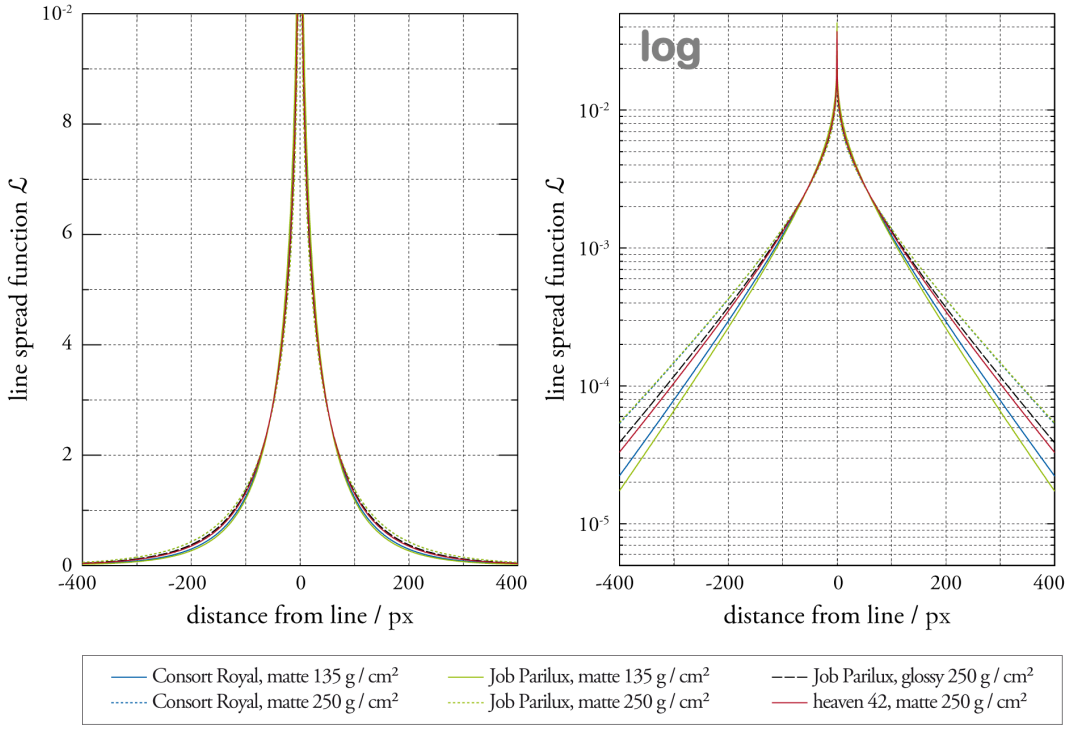

Figure B.19: LSFs for other Scheufelen papers.

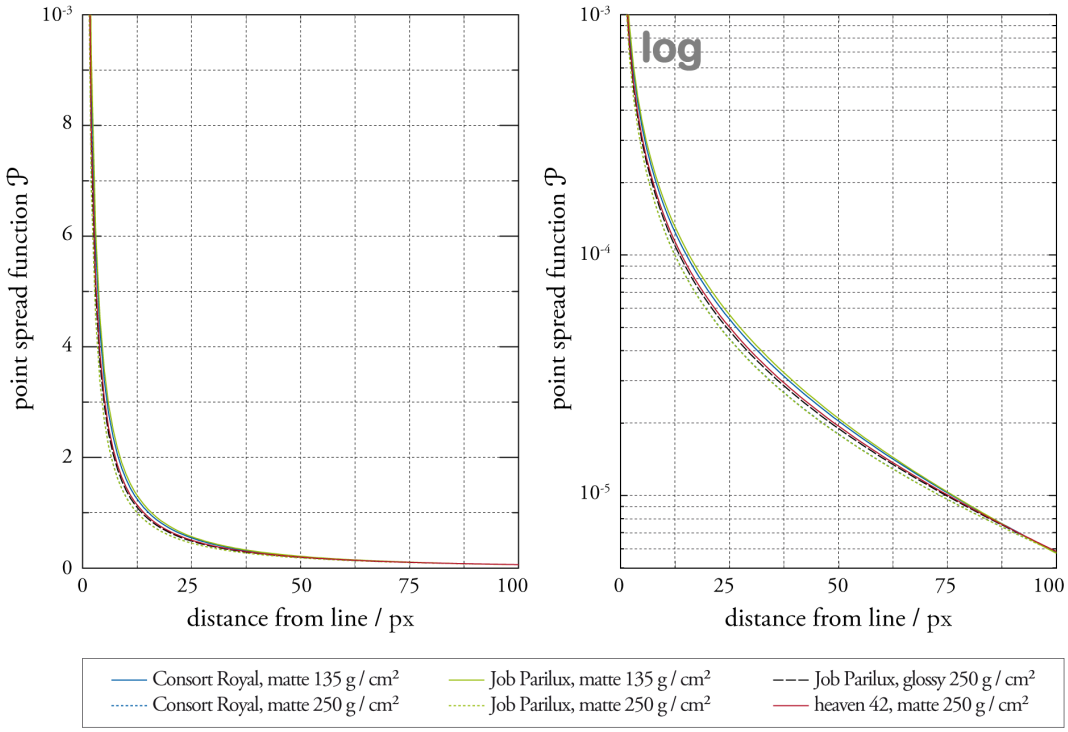

Figure B.20: PSFs for other Scheufelen papers.

B.4 Stora Enso Papers

Series	Coating	Grammage	Color
LumiArt	glossy	100 g/m^2	ND
	glossy	250 g/m^2	ND
	glossy	400 g/m^2	ND
LumiSilk	matte	100 g/m^2	ND
	matte	250 g/m^2	ND
	matte	400 g/m^2	ND

Table B.7: Investigated Stora Enso papers.

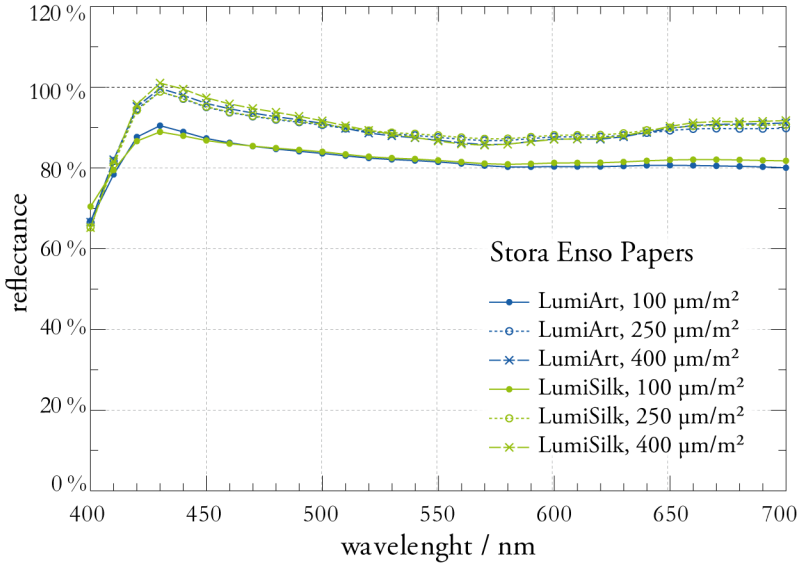

Figure B.21: Reflectance spectra for Stora Enso papers.

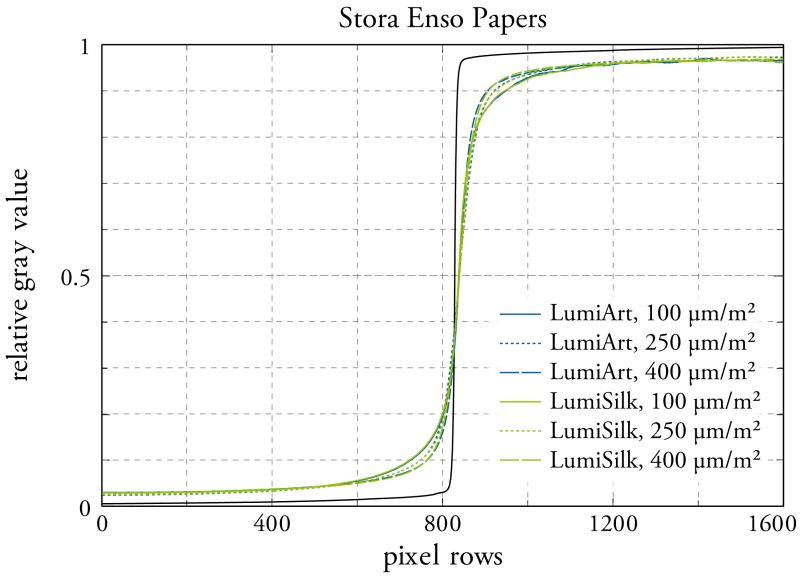

Figure B.22: ESFs for Stora Enso papers.

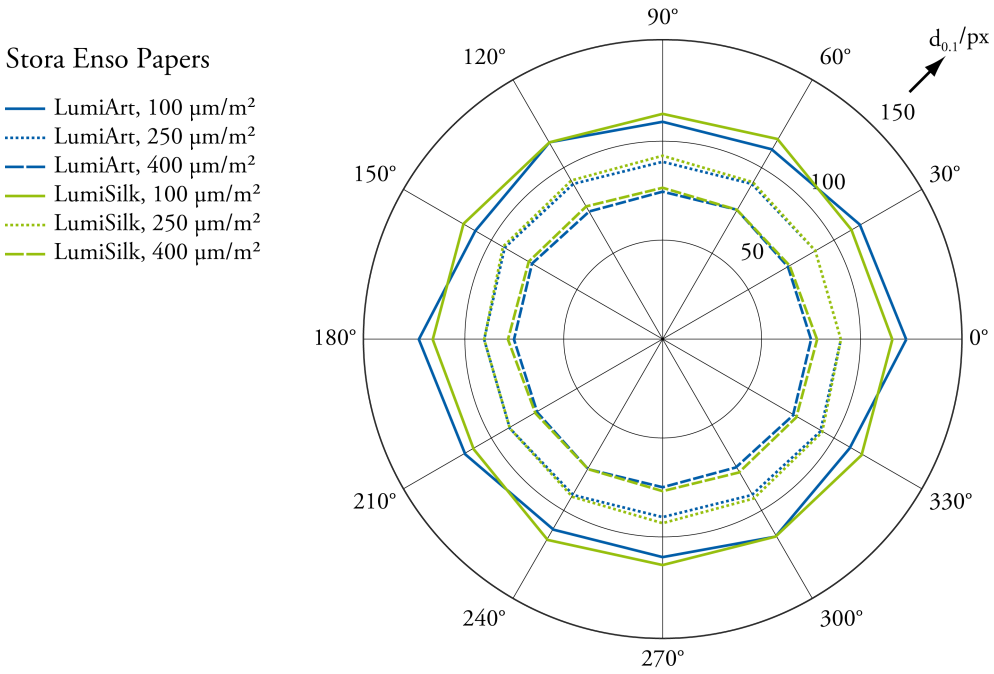

Figure B.23: 0.1-indicatrices for Stora Enso papers.

Value	PBX	LIN	GAU	EXP	EMG	QUA	linprog
LumiArt, 100 g/m^2							
s/px	81	114	47	33	79	0,07	
RMSD·1000	37,77	35,51	33,91	29,85	22,78	27,47	8,44
LumiArt, 250 g/m^2							
s/px	85	119	49	34	79	0,07	
RMSD·1000	29,34	27,27	25,69	22,17	17,78	36,98	5,30
LumiArt, 400 g/m^2							
s/px	63	88	36	25	60	0,05	
RMSD·1000	30,77	29,16	27,98	25,24	21,19	28,35	6,99
LumiSilk, 100 g/m^2							
s/px	77	109	45	31	75	0,06	
RMSD·1000	34,86	32,50	30,82	26,52	18,91	28,87	5,60
LumiSilk, 250 g/m^2							
s/px	78	110	45	31	74	0,06	
RMSD·1000	30,71	28,65	27,11	23,52	18,39	33,64	5,93
LumiSilk, 400 g/m^2							
s/px	72	99	41	28	66	0,05	
RMSD·1000	29,07	27,36	26,11	23,36	19,96	32,67	7,68

Table B.8: Results of the LSF calculation for investigated Stora Enso papers; form parameter s and RMSD.

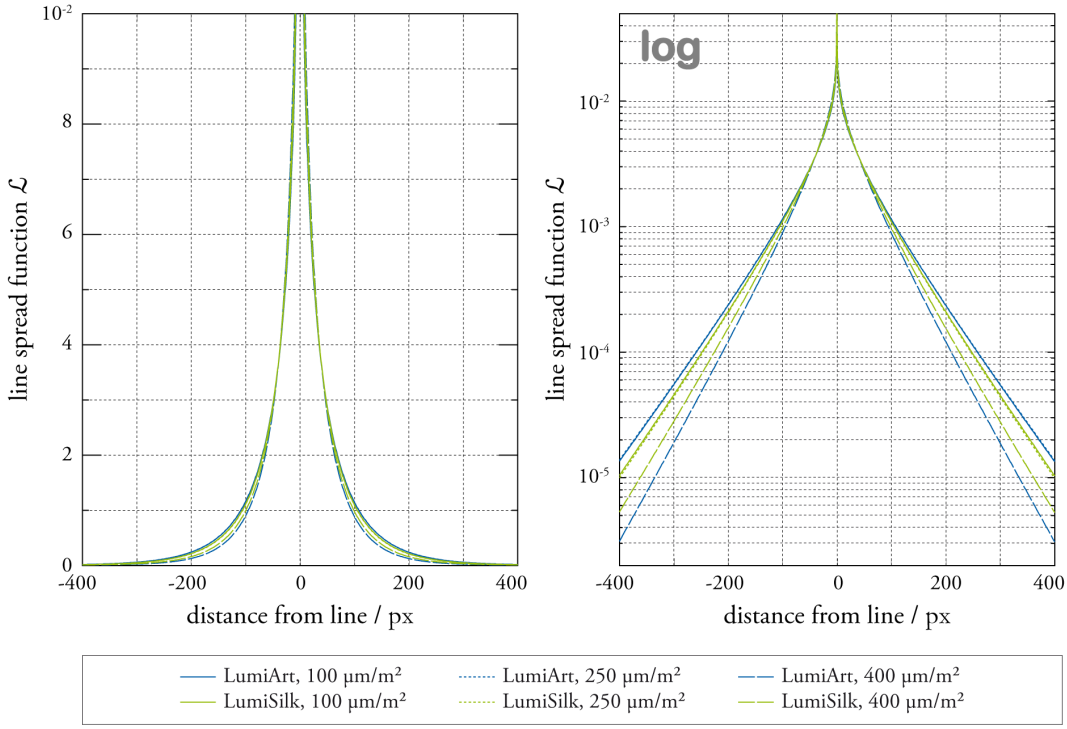

Figure B.24: LSFs for Stora Enso papers.

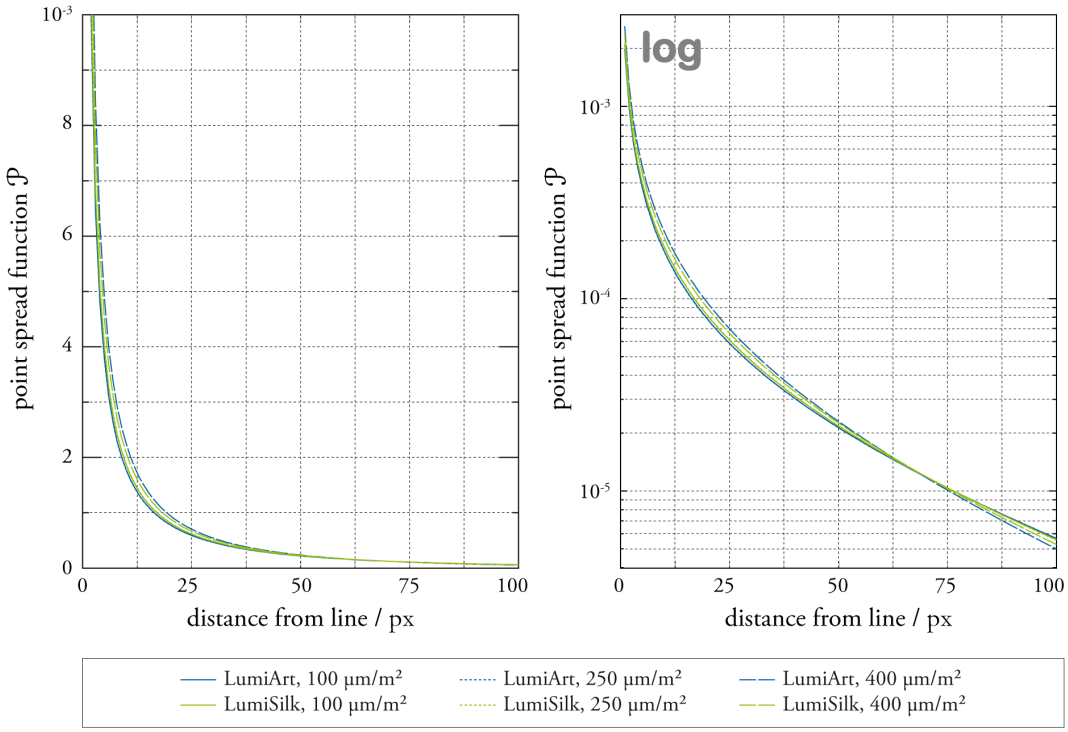

Figure B.25: PSFs for Stora Enso papers.